Shape Optimization: Theoretical, Numerical and Practical Aspects

Beniamin Bogosel

To cite this version:

Beniamin Bogosel. Shape Optimization: Theoretical, Numerical and Practical Aspects. Optimization and Control [math.OC]. Ecole Polytechnique, 2024. tel-04595474

HAL Id: tel-04595474
https://hal.science/tel-04595474

Submitted on 31 May 2024

INSTITUT
POLYTECHNIQUE
DE PARIS

Shape Optimization: Theoretical, Numerical and Practical Aspects

Beniamin Bogosel

Professeur assistant, CMAP UMR 7641, École Polytechnique

30 mai 2024

Sur avis des rapports de :

Samuel Amstutz
Maître de Conférences HdR, LMA, Avignon Université

Chiu-Yen Kao
Professeure, Claremont McKenna College, Claremont, USA

Jimmy Lamboley
Professeur, IMJ-PRG, Sorbonne Université Paris

Composition du Jury :

Grégoire Allaire
Professeur, CMAP, École Polytechnique

Samuel Amstutz
Maître de Conférences HdR, LMA, Avignon Université

Virginie Bonnaillie-Noël
Directrice de recherche CNRS, DMA, ENS Paris

Dorin Bucur
Professeur, LAMA, Université Savoie Mont Blanc

Antoine Henrot
Professeur émérite, IECL, École des Mines, Nancy

Chiu-Yen Kao
Professeure, Claremont McKenna College, Claremont, USA

Jimmy Lamboley
Professeur, IMJ-PRG, Sorbonne Université, Paris

Édouard Oudet
Professeur, LJK, Université Grenoble Alpes, Grenoble

Habilitation à Diriger les Recherches

Remerciements

Les travaux présentés dans ce manuscrit sont le fruit des nombreuses discussions et collaborations. Je remercie tous mes collaborateurs et tous ceux qui par une question, suggestion ou critique m'ont aidé à focaliser mes idées de recherche. Merci aux collègues du CMAP et aux personnels administratifs qui contribuent à créer un cadre de travail très agréable.

Je voudrais remercier Samuel Amstutz, Chiu-Yen Kao et Jimmy Lamboley pour avoir accepté de lire le manuscrit et d'écrire un rapport. J'en suis très honoré.

Un grand merci à Grégoire Allaire pour tous ses conseils, commentaires et encouragements concernant ce mémoire. Merci également pour tous les nouveaux sujets de recherche que j'ai pu découvrir en travaillant avec lui et qui ont grandement influencé ma recherche après la thèse.

Je garde de très beaux souvenirs de mon séjour à l'ENS ou j'ai pu travailler avec Virginie Bonnaillie-Noël pour étudier des nouveaux aspects concernant les partitions spectrales optimales. Les discussions avec Antoine Henrot sur l'optimisation des quantités spectrales parmi les convexes ont motivé une de mes principales axes de recherche. Merci à tous les deux d'avoir accepté de faire partie du jury.

L'influence positive de Dorin Bucur et Édouard Oudet sur mes recherches continue même après la thèse. Merci Édouard pour tes provocations à travailler sur des beaux problèmes. Merci Dorin pour tous les bons moments qu'on a pu passer ensemble en parlant des maths et plein d'autres choses.

Mes parents et ma famille m'ont toujours soutenu dans ma passion pour étudier les maths et je leur suis reconnaissant. Cristina, Gloria et Felix, vous êtes à mes côtés chaque jour, et vous êtes ma plus grande source d'inspiration et motivation. Je vous aime.

Contents

Chapter 1

Introduction

1.1 General aspects: shape optimization and modelization

In this memoir I present various results concerning **shape optimization problems**, i.e. optimization problems where the variable is a shape. A typical formulation for such problems is given by

$$\min_{\Omega \in \mathcal{U}_{ad}} J(\Omega), \tag{1.1}$$

where $\mathcal{U}_{ad}$ represents the class of admissible shapes denoted by Ω, including possible constraints.

When studying shape optimization problems, many classical questions like the existence and regularity of optimal shapes are not straightforward. Such results depend on the proper choice of a topology on the class of admissible shapes $\mathcal{U}_{ad}$. Classical monographs [71], [52], [2], [36] show how to handle such difficulties. Ideally one would like to find explicit solutions to problems of the form (1.1), however this can rarely be done. Therefore, finding numerical approximations of optimal shapes is of great interest from both theoretical and practical reasons. My work deals with a diverse range of aspects regarding shape optimization problems, as underlined below.

Theoretical aspects presented in my work include results regarding the existence of optimal shapes (for example [A1], [A2], [A3], [A25]) and regularity of optimal shapes [A4]. The computation of shape derivatives is also an essential aspect, with theoretical and numerical implications [A3], [A5], [A6]. In particular, in [A7] I worked on the computation of first and second shape derivatives on polygonal domains, together with other theoretical aspects, motivated by the Polyà-Szegö conjecture (more details are given in Chapter 5).

Numerical simulations play an important role when dealing with shape optimization problems. From a practical or industrial point of view, optimization algorithms can improve a given design by decreasing the objective function, usually related to manufacturability or final usage constraints. From a theoretical point of view, simulations may indicate qualitative properties of the optimal shape or even suggest meaningful conjectures that can lead to new proof strategies.

Modelization aspects play a fundamental role for rendering theoretical and numerical aspects from shape optimization useful from an industrial point of view. A key aspect for developing a successful modelization strategy is the constant interaction with the industrial partners. I had the opportunity to experience this in the SOFIA project (described in Section 2.2), regrouping multiple industrial and academic partners around topics related to metal additive manufacturing techniques. The research work that resulted from this experience will be presented in Chapter 2.

In my research work after my PhD defense I dealt with various aspects related to shape optimization problems. In the following, two classifications of my works are provided, underlining the associated contributions. The first classification is related to the final purpose of the methodology, while the second is related to more concrete aspects underlining the discrete representation of shapes in numerical practice.

1.2 First classification: final purpose of the methodology

I. Improve a given design preserving practical constraints. From an industrial point of view, this is a meaningful objective, as the cost function to be minimized is often related to fabrication costs. One may also underline that numerical shape and topology optimization methods are used in this context even when there exists no optimal shape. This aspect leads to potential numerical difficulties, as the optimal design obtained numerically often depends on the initialization and on the mesh used to describe the shape. Classical aspects related to such ideas are presented in [7], [2], [21].

I started working on this type of problems during my postdoc in the SOFIA project supervised by Grégoire Allaire. The SOFIA project dealt with various aspects related to metal based Additive Manufacturing (AM) processes. I worked on the optimization of support structures. One particularity of this work was the strong connection with the industrial partners. The regular exchanges with these partners helped us tune our models and propose solutions that were in accord with the desired fabrication constraints.

I collaborated on this subject with G. Allaire, Martin Bihr (PhD student in co-supervision with G. Allaire) and Matias Godoy-Campbell (postdoc in the SOFIA project in co-supervision with G. Allaire) and these collaborations lead to the following publications: [A8], [A9], [A5], [A10], [A11].

II. Find new directions for theoretical study, confirm and propose conjectures. Imposing convexity of admissible shapes often leads to straightforward proofs of existence of optimal shapes. However the complete analytic descriptions of such optimal shapes are often unavailable. Numerical optimization algorithms can efficiently approximate such optimal shapes and give concrete ideas motivating the theoretical study.

A first example illustrating this concept is the article [A12] in collaboration with Antoine Henrot and Ilaria Lucardesi, where we study two dimensional shapes minimizing the k-th eigenvalue of the Dirichlet-Laplace operator when a diameter constraint is imposed. During our study, multiple back-and-forth exchanges between numerical computations and theoretical observations helped us advance towards the goal. The diameter constraint, contrary to well studied volume [35], [102] and perimeter constraints [51], [A13], is non-local and the disk becomes a local minimum for a larger number of indices k. A similar approach is employed for the Steklov eigenvalues in the paper [A2] in collaboration with A. Al Sayed, A. Henrot and F. Nacry.

Motivated by the interest researchers have in the use of numerical tools for approximating convex optimal shapes, together with Pedro Antunes we worked in [A1] on a two and three dimensional numerical framework where the support function of a convex set is approximated using a truncated spectral decomposition. The numerical framework was generalized even further in [A14] (only in dimension two), where arbitrary convex shapes, including those having segments in the boundary, can be efficiently approximated.

III. Prove that a given shape is optimal. Using numerical tools to prove a shape is not optimal, generally amounts to finding a counter example: an optimization algorithm needs to find a shape with a smaller value than the conjectured one. Unfortunately, the opposite situation occurs most of the time: the numerical optimization algorithm finds the conjectured shape. Confirming such conjectures validates and motivates the theoretical ideas, but is not enough to prove that the shapes obtained numerically are optimal.

It is possible, nevertheless, to imagine a strategy that could prove that a given shape is optimal with the aid of numerical tools. Suppose that the shape S_n^* depends on n real parameters. Consider the following steps:

- Prove that S_n^* is a local minimizer: compute analytically the associated Hessian matrix and conclude that it is positive definite (in a proper sense that takes into account the eventual constraints). If no theoretical proof of positivity of the Hessian is available, numerical tools can be employed.
- Prove that shapes *far away* (in a sense to be defined) from S_n^* cannot be minimizers. This

is usually a consequence of explicit theoretical bounds on various geometric quantities of potential minimizers.

- Identify precisely the bounded region which is not covered by the previous two steps and devise a strategy to show through a finite series of validated numerical computations that no minimizer exists in this region.

All computations involved in the above strategy should be validated, in the sense that all errors need to be accounted for: discretization errors related to numerical PDE approximation methods (finite elements), errors related to machine representation (use of interval arithmetics).

Together with Dorin Bucur we show in [A7] that such a strategy can be used for a well known conjecture due to Polya and Szegö:

The regular n-gon minimizes the first eigenvalue of the Dirichlet-Laplace operator among n-gons having fixed area.

Despite its simplicity, this question is still unanswered for $n \geq 5$. In [A7] we make a series of initial steps towards a hybrid proof, including the computation of the Hessian matrix when considering vertex coordinates as variables, the computation and validated numerical approximation of the eigenvalues of the Hessian matrix, formal reduction of the proof to a finite number of validated numerical computations. This initial work opens the way to a series of new perspectives from both theoretical and numerical points of view.

1.3 Second classification: choice of discretization method

From a numerical point of view, the variable shapes Ω in (1.1) need to be described starting from a finite number of parameters. The choice of discretization should be rich enough to allow the representation of a family of shapes that is as large as possible. Moreover, the constraints that are present make some choices of representation more advantageous than other ones. Below I give a short description of the discretization methods used in my work.

(a) Explicit parametrization. Having a precise and explicit parametrization of the boundary gives access to the complete geometric information regarding the given shapes. This allows the use of precise numerical approximation techniques (for example, fundamental solutions for solving PDEs) and of more advanced numerical optimization algorithms (LBFGS, IPOPT). On the other hand, such parametrizations are available only when the admissible shapes are *simple enough*. For example, when considering star-shaped domains [A13], [A3], [A6] or convex domains [A12], [A1].

(b) Density functions. Explicit parametrizations described previously limit the complexity of the shapes that can be represented. Explicit representations become too tedious when dealing with optimal partitioning problems. In order to capture arbitrarily complex shapes one may consider a bounding domain D and represent a shape $\omega \subset D$ using its characteristic function $\chi_\omega : D \to \{0, 1\}$. In practice it is more convenient to relax the parametrization and allow a transition zone using density functions $\varphi : D \to [0, 1]$. In addition to the arbitrary complexity of the shapes (depending on the mesh or discretization of the bounding box D), partitioning conditions are straightforward in this case: the sum of the associated densities is identically equal to 1.

Density based methods are classical and one may cite the famous SIMP method described in [21]. One drawback of this method is the use of a *penalization* technique to extract a shape from the optimal density function. One particularity of my work is that problems we studied are *self-penalized* in the sense that the minimization in the class of relaxed densities with values in $[0, 1]$ or even $\mathbb{R}$ leads naturally to densities that are close to characteristic functions. This self-penalization phenomenon is due to some double well potential terms appearing in Γ-convergence approximations or to the concavity of the dependence of the objective functions in the density φ.

I use density functions representations in the following works:

- **Minimization of sums and p-norms of the fundamental eigenvalues for the cells of a partition.** A first work in this direction is [A15] in collaboration with V. Bonnaillie-Noël (while I was a postdoc at Ecole Normale Supérieure Paris) where we investigated the behavior of optimal partitions up to 10 cells of some planar domains. One particularity of this work, further investigated and improved in [A16], is the use a truncation of the computational domain to accelerate the computation of the first eigenvalue associated to a density $\varphi : D \to [0,1]$: only nodes and neighbors of the set $\{\varphi > \varepsilon\}$ are used in the PDE computation, significantly improving the convergence speed of the optimization algorithm compared to the original algorithm in [32].
- **The study of Cheeger sets and clusters.** Together with D. Bucur and I. Fragalà we worked in [A17] on a Γ-convergence approximation for α-Cheeger sets and clusters. In particular, we obtain a variational method for investigating circle and sphere packings which avoids the usual combinatorial difficulties of a direct approach.
- **Maximiziation of the minimal perimeter of a partition.** Together with E. Oudet, we worked in [A3] on maximizing the minimal perimeter of a partition of a two or three dimensional domain. During the optimization process, numerical optimal partitions minimizing the total relative perimeter are computed at every iteration. The classical Modica-Mortola Γ convergence result [97] is used for approximating the minimal total relative perimeter.

(c) Level-set representation. The use of density functions as a numerical representation method leads to difficulties in identifying the actual boundary of the associated shape. A penalization method [21] or some heuristical method, for example choosing a threshold of the density, need to be used. The level-set method introduced by Osher and Sethian [101] and used successfully in structural optimization [7] consists of considering a bounding domain D and a function $\phi : D \to \mathbb{R}$. The shape parametrized by ϕ is the level-set $\omega = \{\phi \leq 0\}$ (the sign convention is a choice). Given a shape $\omega \subset D$, one natural choice of level-set function is the signed distance function d_ω, defined as the distance to the boundary $\partial\omega$ with positive sign outside and negative sign inside. This choice allows to recover easily geometric information on ω: ∇d_ω gives the normal vector, Δd_ω gives the mean curvature, etc. Efficient algorithms were devised in [113], [40], [50] for re-initializing a level-set function as a distance function and for advecting a level-set function using a vector field.

I use level-set methods in all articles related to industrial applications for additive manufacturing [A8], [A9], [A10], [A11], [A5].

1.4 Co-advising of young researchers

PhD thesis of Martin Bihr: 2019-2022. [23] I co-advised this thesis together with G. Allaire. This PhD thesis was a CIFRE[1] thesis at Safran Tech. On the industrial side, the thesis had the following advisors: X. Betbeder-Lauque, F. Bordeu, J. Querois from Safran.

The subject of the thesis is the optimization of the shape and support structures for designs in additive manufacturing for SLM technologies. Various results obtained in this thesis are presented in Sections 2.3, 2.5 and are the subject of publications [A9], [A5].

Postdoc – Matias Godoy: 2019-2022. This postdoc which I co-advised together with G. Allaire was financed by the SOFIA project (described in Section 2.2).

The subject of the postdoc was the study of shape optimization problems for imperfect interface problems, motivated by practical aspects related to support structures in additive manufacturing. The work is described in Section 2.6 and is the subject of the papers [A10], [A11].

Phd thesis of Richard Joly: 2022–. I am a co-advisor together with G. Allaire of this CIFRE PhD thesis in collaboration with Total. The subject of the thesis is the optimization of

---

[1] Conventions industrielles de formation par la recherche

batteries.

Summer internship of Mehdi Makni: 2021. I advised this internship during Mehdi's second Bachelor year. The goal of the internship was to further develop aspects I taught in the course MAA209 (Introduction to numerical Optimization) for Bachelor students. During the internship Mehdi worked on the implementation in Python of several algorithms related to spectral partitioning problems described in Section 4.4 and in particular the one shown in [A16].

1.5 Code production

I uploaded on Github the codes used for the simulations in some of my articles. More precisely:

- The following toolbox used in [A17] can be used to approximate numerically Cheeger sets and optimal Cheeger patches. More details are given in Section 4.3.

  `https://github.com/bbogo/Cheeger_patch`

- The following repository

  `https://github.com/bbogo/LongestShortestPartitions`

  contains codes used in [A3]. It features a Python Jupyter Notebook used to compute Voronoi diagrams with prescribed cell areas and minimal perimeter. In particular, the sensitivities of the areas and perimeters of individual Voronoi cells with respect to the position of the Voronoi points are computed. The second part contains FreeFEM codes used for the maximization of the minimal relative perimeter of a partition. The context and more details are given in Section 4.2.
- The repository

  `https://github.com/bbogo/ConvexSets`

  contains codes related to the paper [A14]. The discretization method described in Section 3.4 is implemented in FreeFEM [66] and is used to solve numerically various shape optimization problems under convexity and width constraints.
- A set of smaller code samples related to papers [A7], [A24], [A20] can be found on my webpage:

  `http://www.cmap.polytechnique.fr/~beniamin.bogosel/software.html`

1.6 Structure of the memoir and List of Publications

The memoir is structured into chapters underlining some of my main contributions to this field and relating them to the two classifications provided previously. Each chapter concludes with a list of perspectives, underlining the new possible lines of research opened by the presented works.

Chapter 2 deals with the optimization of the shape and topology of part and support structures in Additive Manufacturing. I started working in this field in collaboration with G. Allaire in the SOFIA project. The chapter starts with a brief introduction to AM providing the relevant modelization issues motivating our work. A first step in the modelization for optimizing support structures in AM is proposed in [A8]. Following the feedback from the industrial partners, we refine our models and propose methods for optimizing the orientation of the part to be fabricated in [A9]. The PhD thesis of M. Bihr leads to the work [A5], where a simplified process simulation method based on the inherent strain method allows to optimize the part and supports related to various thermo-mechanical criteria.

Post-processing of the contact regions between the part and support structures can be costly. Sometimes an imperfect bonding between part and supports is desirable. In collaboration with

G. Allaire and M. Godoy, we study shape optimization problems involving two phases with imperfect bonding in the articles [A10], [A11].

Chapter 3 presents numerical aspects related to shape optimization under convexity constraints. The support function is the main tool used, allowing to transform the geometric convexity constraint into a functional one. An initial numerical framework using truncated spectral decompositions is presented, based on the works [A12], [A1].

A main drawback of using truncated spectral decompositions is the implicit assumption of strict convexity. On the other hand, the saturation of the convexity constraint appears naturally in many cases: segments in the boundary need to be taken into account. A second approach is provided, considering the values of the support function on a discretization of $[0, 2\pi]$, based on the articles [A2], [A14].

Chapter 4 presents aspects related to numerical optimal partitions and multiphase problems. One particularity of the numerical methods presented in this chapter is the use of densities to represent shapes.

The use of Γ-convergence results together with density representation of shapes allows us to study optimal α-Cheeger clusters in [A17] and to maximize minimal perimeter partitions in [A3].

In papers [A15], [A16] an improvement of the algorithm introduced in [32] is proposed. The improved algorithm allows to efficiently find optimal partitions minimizing sums of fundamental eigenvalues of each cell for many cells and even in dimension three. Partitions minimizing the maximal fundamental eigenvalue of the cells are of particular interest in [A15] and further aspects in this direction are discussed in [A18].

Chapter 5 presents the strategy for a hybrid proof of the polygonal Faber-Krahn inequality based on the paper [A7] in collaboration with D. Bucur. Following [88], we compute the second derivative of a simple eigenvalue of the Dirichlet-Laplace operator. Using distributed volumic integrals only Lipschitz regularity is required for the shape and perturbation fields. This allows us to obtain the Hessian of the first eigenvalue of a polygon, taking the vertex coordinates as variables. Furthermore, the eigenvalues of the Hessian matrix are computed and explicit error bounds are given for their approximations using finite elements. Numerical simulations show that the regular polygon is a local minimizer. Various theoretical estimates allow us to show that the proof of the Polyà-Szegö conjecture can be reduced to a finite number of validated numerical computations.

The following papers are not presented in this memoir:

- Papers related to my PhD thesis: [A13], [A19], [A20], [A21], [A22], [A23], [A4].
- In [A24], together with V. Perollaz, K. Raschel and A. Trotignon, we study the critical exponents of a class of random walks. The main tool used is the computation of the fundamental eigenvalue of the Laplace-Beltrami eigenvalues for particular spherical triangles.
- In [A6] together with T. Giletti and A. Tellini we study the behavior of the spreading speed for KPP bulk-surface systems with respect to the shape of the section of the cylindrical domain.
- In [A25] together with P. Antunes we consider the optimization of the low eigenvalues of the Steklov-Lamé operator. We investigate theoretical questions related to existence of minimizers and we perform numerical computations of optimal domains.
- In [A26], which is an expository paper, I present a new geometric proof of a theorem of Siebeck and Marden linking the roots of a cubic polynomial to the roots of its derivative via geometric arguments.

References

[A1] P. R. S. Antunes and B. Bogosel, “Parametric shape optimization using the support function,” *Comput. Optim. Appl.*, vol. 82, no. 1, pp. 107–138, 2022.

[A2] A. Al Sayed, B. Bogosel, A. Henrot, and F. Nacry, “Maximization of the Steklov eigenvalues with a diameter constraint,” *SIAM J. Math. Anal.*, vol. 53, no. 1, pp. 710–729, 2021.

[A3] B. Bogosel and E. Oudet, “Longest minimal length partitions,” *Interfaces Free Bound.*, vol. 24, no. 1, pp. 95–135, 2022.

[A4] B. Bogosel, “Regularity result for a shape optimization problem under perimeter constraint,” *Comm. Anal. Geom.*, vol. 27, no. 7, pp. 1523–1547, 2019.

[A5] M. Bihr, G. Allaire, X. Betbeder-Lauque, B. Bogosel, F. Bordeu, and J. Querois, “Part and supports optimization in metal powder bed additive manufacturing using simplified process simulation,” *Comput. Methods Appl. Mech. Engrg.*, vol. 395, pp. Paper No. 114975, 30, 2022.

[A6] B. Bogosel, T. Giletti, and A. Tellini, “Propagation for KPP bulk-surface systems in a general cylindrical domain,” *Nonlinear Anal.*, vol. 213, pp. Paper No. 112528, 42, 2021.

[A7] B. Bogosel and D. Bucur, “On the polygonal Faber-Krahn inequality,” 2022.

[A8] G. Allaire and B. Bogosel, “Optimizing supports for additive manufacturing,” *Struct. Multidiscip. Optim.*, vol. 58, no. 6, pp. 2493–2515, 2018.

[A9] G. Allaire, M. Bihr, and B. Bogosel, “Support optimization in additive manufacturing for geometric and thermo-mechanical constraints,” *Struct. Multidiscip. Optim.*, vol. 61, no. 6, pp. 2377–2399, 2020.

[A10] G. Allaire, B. Bogosel, and M. Godoy, “Shape optimization of an imperfect interface: steady-state heat diffusion,” *J. Optim. Theory Appl.*, vol. 191, no. 1, pp. 169–201, 2021.

[A11] G. Allaire, B. Bogosel, and M. Godoy, “Topology optimization of supports with imperfect bonding in additive manufacturing,” *Structural and Multidisciplinary Optimization*, 2022.

[A12] B. Bogosel, A. Henrot, and I. Lucardesi, “Minimization of the eigenvalues of the Dirichlet-Laplacian with a diameter constraint,” *SIAM J. Math. Anal.*, vol. 50, no. 5, pp. 5337–5361, 2018.

[A13] B. Bogosel and E. Oudet, “Qualitative and numerical analysis of a spectral problem with perimeter constraint,” *SIAM J. Control Optim.*, vol. 54, no. 1, pp. 317–340, 2016.

[A14] B. Bogosel, “Numerical shape optimization among convex sets,” 2022.

[A15] B. Bogosel and V. Bonnaillie-Noël, “Minimal partitions for p-norms of eigenvalues,” *Interfaces Free Bound.*, vol. 20, no. 1, pp. 129–163, 2018.

[A16] B. Bogosel, “Efficient algorithm for optimizing spectral partitions,” *Appl. Math. Comput.*, vol. 333, pp. 61–75, 2018.

[A17] B. Bogosel, D. Bucur, and I. Fragalà, “Phase field approach to optimal packing problems and related Cheeger clusters,” *Appl. Math. Optim.*, vol. 81, no. 1, pp. 63–87, 2020.

[A18] B. Bogosel and V. Bonnaillie-Noël, “Optimal partitions for the sum and the maximum of eigenvalues,” in *Fourteenth International Conference Zaragoza-Pau on Mathematics and its Applications*, vol. 41 of *Monogr. Mat. García Galdeano*, pp. 41–53, Prensas Univ. Zaragoza, Zaragoza, 2018.

[A19] B. Bogosel and B. Velichkov, “A multiphase shape optimization problem for eigenvalues: qualitative study and numerical results,” *SIAM J. Numer. Anal.*, vol. 54, no. 1, pp. 210–241, 2016.

[A20] B. Bogosel, “The method of fundamental solutions applied to boundary eigenvalue problems,” *J. Comput. Appl. Math.*, vol. 306, pp. 265–285, 2016.

[A21] B. Bogosel, “The Steklov spectrum on moving domains,” *Appl. Math. Optim.*, vol. 75, no. 1, pp. 1–25, 2017.

[A22] B. Bogosel, D. Bucur, and A. Giacomini, “Optimal shapes maximizing the Steklov eigenvalues,” *SIAM J. Math. Anal.*, vol. 49, no. 2, pp. 1645–1680, 2017.

[A23] B. Bogosel and E. Oudet, “Partitions of minimal length on manifolds,” *Exp. Math.*, vol. 26, no. 4, pp. 496–508, 2017.

[A24] B. Bogosel, V. Perrollaz, K. Raschel, and A. Trotignon, “3D positive lattice walks and spherical triangles,” *J. Combin. Theory Ser. A*, vol. 172, pp. 105189, 47, 2020.

[A25] B. Bogosel and P. R. S. Antunes, “Optimization of the Steklov-Lamé eigenvalues with respect to the domain,” 2022.

[A26] B. Bogosel, “A geometric proof of the Siebeck-Marden theorem,” *Amer. Math. Monthly*, vol. 124, no. 5, pp. 459–463, 2017.

Chapter 2

Design optimization for additive manufacturing

2.1 Introduction

Shape and topology optimization methods introduced new ways of designing parts to be used in industrial applications. Structural optimization methods modify the design such that volume or some other relevant constraints are preserved, while the objective function corresponding to some practical quantity of interest is diminished. Pioneering works in this sense use methods inspired from homogenization [21] and the level-set method [7], [118]. Nevertheless, such automatic design methods often produce shapes with complex topologies, which are difficult, if not impossible, to manufacture using conventional fabrication methods (molding, casting). For manufacturability purposes, additional constraints were considered and applied during the optimization process. Among these I mention thickness constraints [6], molding direction constraints [5], geometric and architectural constraints [49].

The rise of Additive Manufacturing (AM) technologies in recent years made possible the construction of arbitrarily complex parts. There exist many such fabrication technologies, the main characteristic being that the initial design is divided into slices which are built successively on top of each other. The complex designs proposed using shape and topology optimization became realizable, at least in theory. From a practical point of view, designs containing significant horizontal regions (called *overhang regions* in the sequel) cannot be fabricated. The type of AM technology used (polymer, selective laser melting – SLM) raises particular limitations and constraints. In order to alleviate the constraints and render the design realizable, two options are available: modifying the shape of the fabricated part or adding support structures.

I started working on shape optimization ideas related to AM when I became a postdoc in the SOFIA project, in collaboration with Grégoire Allaire at CMAP. The subject of my work was the optimization of the shape and of the topology of support structures in SLM fabrication processes. Initial works dealing with shape optimization for AM optimize the constructed part ω so that the fabrication process can succeed. It is generally agreed that large unsupported surfaces that are almost horizontal cannot be constructed correctly using AM (using polymer or SLM technologies). Constraints related to the control of the size of overhanging regions can be formulated either in a direct geometric way [119], [3] or using modelization aspects based on the mechanical behavior of the part during the build process [3]. The novelty of our approach is that for a fixed part ω we consider adding optimized supports S such that manufacturability requirements are achieved for the whole structure $S \cup \omega$. The fact that ω is fixed is a constraint which is imposed in various applications where the design of the part cannot be modified to render it feasible using AM techniques.

One main aspect of my work was meeting with industrial partners (AddUp, Safran, Zodiac, Volume) and learning from their practical experience how to design and adapt our simulation and optimization models to the industrial requirements. Multiple such exchanges allowed us to obtain results having an impact on the industrial applications.

Given a fixed design ω and a design region D, containing ω, modeling the build chamber, we consider variable supports $S \subset D \setminus \omega$ that are subject to optimization. One natural way to obtain optimized support structures S is to minimize an objective function related to the displacements provided by the linearized elasticity equation. The loading forces and boundary conditions considered are inspired by the practical configuration of the part to be manufactured and model the behavior of the part/support structure during the manufacturing process. The nature of the forces considered lead to different results as illustrated in the following. In [A8] we consider optimizing supports to counteract the action of the gravity on the part, modeled by a volumic force in the elasticity equation acting inside of the part ω. In [A9] we study how the orientation of the part influences the need of support structures. We also investigate how the use of surface forces (modeling gravitational effects on overhangs or displacements induced by thermo-mechanical deformations) change the behavior of the supports. Various technical difficulties were encountered at this stage: handling STL files (containing a triangulation of the surface of the part to be fabricated) and constructing fitted meshes around the part, obtaining the design space for the supports. The software FreeFEM [66] and the re-meshing library MMG [48] were intensively used.

In Section 2.2 practical aspects regarding the SLM manufacturing process are presented, motivating the models proposed in the next sections. Section 2.3 deals with the optimization of the orientation of the part with respect to various aspects related to AM and support structures. In Section 2.4 an initial model is presented, where supports are optimized in order to counteract the gravitational forces acting in the interior of the design. A refinement of this model is given, applying surface loads mimicking the gravity on overhang regions. Compared with the previous model, the second one produces supports that touch all regions that are in overhang.

Section 2.5 presents a summary of the work done in the thesis of Martin Bihr [23] (CIFRE thesis at Safran Tech) which I co-supervised with Grégoire Allaire. A simplified process simulation for SLM printing is proposed, based in the inherent-strain method. This model is efficient and manages to capture the thermo-mechanical effects present during the manufacturing process. Various criteria are investigated, among which I mention: the Von Mises stress, the maximal vertical displacement of the structure for each layer, the vertical displacement of the part released from the fabrication plateau. This work lead to the publication [A5] and various aspects were validated experimentally, since a plateau with optimized shapes for various criteria was fabricated using a SLM machine at Safran.

Section 2.6 presents the work done in collaboration with Matias Godoy and Grégoire Allaire regarding imperfect interface models. To improve the post-processing of parts, including the removal of supports, sometimes an imperfect part-support interface is used. We investigate mechanical models where the contact region between two materials is imperfect, i.e. the global structure is less rigid along the interface. We study these models in the context of shape and topology optimization, studying the corresponding shape derivatives and proposing numerical methods for approximating solutions to the associated PDEs. This work lead to the articles [A10] and [A11].

2.2 Practical aspects regarding support structures

In our work we focus on SLM (selective laser melting) AM fabrication processes, motivated by the interest of the industrial partners in the SOFIA project. In most of this chapter we suppose that the design of the fabricated part is given and we may modify its orientation or add support structures to facilitate its construction. Given a part ω to be fabricated, the design is divided into slices which are constructed successively on top of each other (see Figure 2.1).

The SLM fabrication process is described as follows:

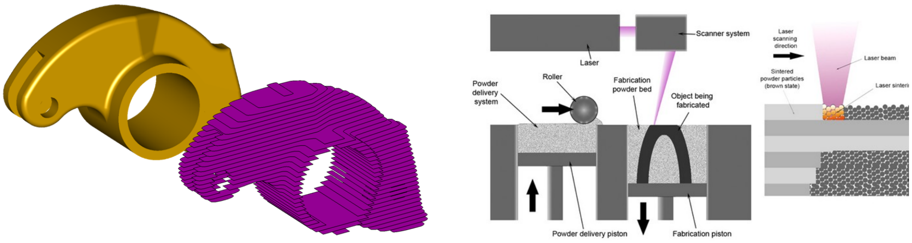

Figure 2.1: Design cut into horizontal slices (left). Graphical description of an SLM machine.

- The fabrication takes place in a rectangular box D, called the build chamber. The lower face of this box is called the baseplate, usually denoted with Γ_D in the sequel.
- A thin layer (typically 50 microns) of metal powder is deposited on top of the existing structure using a roller.
- The laser melts the metal powder on the regions corresponding to the current slice. The melted metal cools down and fusions with the existing structure.
- The structure is lowered and the process is repeated until all slices are constructed.

Already it can be noted that contrary to polymer AM technologies, the space outside the part to be fabricated is filled with metal powder. The metal powder is a poor heat conductor, acting almost as an insulator. Moreover, the powder does not act as a support and melting parts of the current layer that are in overhang may lead to bubbling and poor surface quality of the constructed part.

Given a part ω and an orientation, the success of the fabrication process is not guaranteed. The SLM fabrication process is costly, with the cost being distributed between the metal powder used and the machine printing time. It is agreed that roughly 90% of the cost is the machine printing time, due to their high production and maintenance cost. There are various reasons that can lead to process failure, which we describe below. We learned about these reasons discussing with the industrial partners in the SOFIA project: AddUp, Fusia, Safran, Zodiac, Volume.

(i) Inclined surfaces. It is generally agreed, based on the practical experiences, that for a given metal there exists an angle β such that surfaces making an angle less than β with the horizontal plane (parallel to the baseplate) cannot be constructed. The threshold angle β is determined experimentally and depends on the machine and the metal powder used. We have two ways of optimizing the construction of inclined surfaces: choosing a proper orientation that minimizes the surface area of overhang regions or adding support structures for these overhang regions.

(ii) Thermo-mechanical deformations. The metal powder is melted on top of the existing structure. This leads to large thermal gradients. As the current slice cools down, it shrinks leading to a horizontal contraction that affects the global part. Overhanging regions are especially subjected to such constraints and, contrary to the intuition, they can be pulled upwards when the horizontal slices contract. (see Figure 2.2) The corresponding vertical deformations of the part are problematic since the deformed part may interfere with the powder deposition system. (see Figure 2.2) A collision of the part with the roller may lead to the deformation of the part, may produce damage to the roller or can simply stop the fabrication process altogether. Even if the fabrication process completes successfully it is possible that the thermo-mechanical stresses in the part may lead to large deformations or cracks. (see Figure 2.2)

(iii) Contact or friction with the powder deposition system. At the powder deposition stage, the roller may exert important friction forces on the part due to the thinness of the current powder layer. The magnitude of the exerted force is proportional to the contact surface between the roller and the part. It is generally agreed that the orientation of the part should be chosen such that there are as few regions as possible parallel to the roller.

Support structures are added to alleviate these potential problems. Nevertheless, the sup-

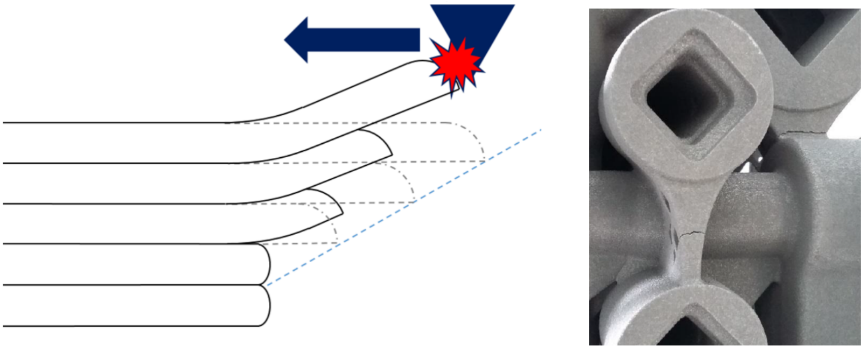

Figure 2.2: (left)Vertical deformation of overhanging regions during SLM fabrication process. (right) Cracks appearing during the SLM fabrication process, due to large thermal stresses.

ports come with a cost. First of all, there is an additional consumption of metal powder and printing time motivating the construction of supports that are as light as possible. Secondly, support structures are removed at the end of the fabrication process and the contact region between the part and supports often needs to be post-processed, leading to additional costs.

Support structures are melted from the same metal powder. Therefore, they have the same material properties. However, it is possible to design support structures that have a lattice structure, leading to different mechanical behavior compared to the fabricated part. It is generally agreed in the industrial practice that full supports give best behavior for preventing the vertical displacement of overhang parts and they conduct heat better to allow a more efficient cooling process.

2.3 Optimization of the orientation

Given a shape $\omega \subset \mathbb{R}^3$ to be printed, it can be observed that changing its orientation may change the quantity of supports needed for its fabrication. Moreover, choosing the proper orientation of a part to be printed is the first step of the fabrication process. Below, we discuss a few criteria that can be used, motivated by the practical observations from the industrial collaborators. These criteria are presented in detail in [A9].

- **Minimize the area of overhang regions.** Given a threshold angle β, for each orientation of the shape ω one can compute the area of the overhang regions. The area can be expressed as a boundary integral on ω and for simplicity one may fix ω and consider the build direction $\vec{d} \in \mathbb{S}^2$ variable (depending on the orientation) leading to the function

  $$\mathcal{G}_1(\vec{d}) = \int_{\partial\omega} H(\vec{n} \cdot (-\vec{d}) - \cos\beta) ds,$$

  where H is the Heaviside function. Replacing H with a smooth approximation leads to a differentiable function, whose gradient can be used for a more efficient local-optimization.

  This formulation can take into account regions for which supports are not wanted. Such a constraint may arise from accessibility issues or due to constraints related to the quality requirements for certain surfaces of the final design. In practice, it is enough to add a weight function in the above integral, penalizing such regions.

- **Minimize the projected area on a given plane.** The motivation for this cost functional is twofold. First, for some applications, multiple parts need to be built during the same fabrication process. To optimize the packing of the parts on the baseplate, the projected area of the part should be as small as possible. Secondly, minimizing the projected area on the plane of the roller will decrease the forces induced by the roller on the built part. For simplicity, we consider the following formula

$$\mathcal{G}_2(\vec{d}) = \int_{\partial\omega} (\vec{n} \cdot \vec{d})_+ ds,$$

for the projected area with eventual repetition. As before, replacing the positive part with a suitable regularization gives an approximate gradient useful for local optimization.

One may observe that rotating the shape around the vertical axis does not change the overhang regions, i.e. $\mathcal{G}_1(\vec{d})$. Therefore, one can combine the two criteria presented up to this point: find the initial orientation minimizing the overhang areas and afterwards find the optimal orientation around the vertical axis for which the projection of the plane of the roller is minimized. See Figure 2.4 for an example.

- **Minimize the volume of vertical supports.** Consider the overhang region $\Gamma_\beta(\partial\omega)$ and compute the volume $\mathcal{G}_3(\vec{d})$ underneath it, i.e. the vertical cylindrical region under overhanging regions. This gives a rough estimate of the quantity of supports needed to support the overhangs. Ray casting can be used to approximate this volume for a given orientation. Rays are sent towards the baseplate starting from the nodes lying on overhanging faces of the discretized design and the first intersection with either the rest of the structure or the baseplate is used to construct the desired cylindrical region where the supports lie.

- **Minimize the variation of the areas of horizontal sections.** A heuristic way of reducing the residual stresses present in the printed object is to have a small variation of the areas of the cross sections of the structure, parallel to the baseplate. Given a triangulation of the structure, recovered from an STL file, it is rather straightforward to compute the polygonal contour corresponding to a slice at a given height. Isocontour algorithms on triangulations can be employed efficiently to do this. Denote by $\mathcal{G}_4(\vec{d})$ the variation of the areas of the slices taken at some uniform distribution of heights between the minimal and maximal one.

Another obvious, and trivial, criterion is the minimization of the height, as a lower height would necessitate fewer layers, leading to a shorter fabrication time. All these different criteria may lead to different optimal orientations and should be considered in view of the desired applications. These different criteria can be investigated quickly for a given design and they give a quick overview of the advantages of different orientation, with respect to different manufacturing constraints. These criteria can also be aggregated into a multi-objective optimization procedure.

From a practical point of view, the angle space for three dimensional objects has dimension two and any one of the above criteria may lead to many local minima. In order to avoid local minima, a rectangular grid is considered and the objective function is evaluated for each point in this grid. Then, if the approximate gradient can be computed, as it is the case for the first two criteria, a more refined local optimization procedure based on a gradient descent algorithm is performed.

Detecting accessible regions. In order to remove support structures and to process contact surfaces, these regions should be accessible from the exterior of the part in a straight line. Complex structures may have regions that do not verify this accessibility assumption. We propose two ways of detecting these regions:

- **Ray tracing.** Consider a family of source points outside the shape and send rays towards all points (x_j) in the discretized part given by a triangulated surface. If the first intersection point of the ray corresponding with x_j with $\partial\omega$ is x_j then this point is accessible. This approach is natural, but the choice of the appropriate source points may differ from shape to shape. See Figure 2.3 for an illustration.

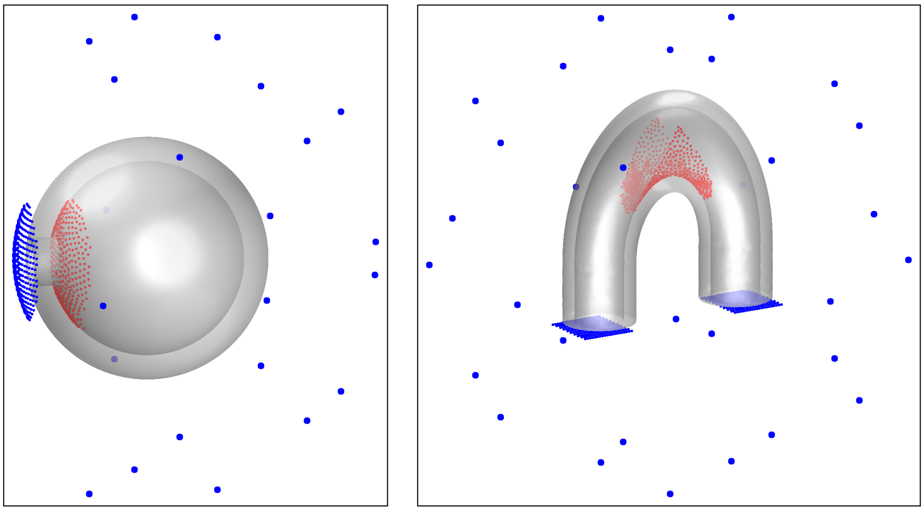

Figure 2.3: Detecting accessible regions using ray casting. The source points are represented with blue and the inaccessible regions with red.

- **Distance functions.** Consider a box D containing ω. Given $x \in \partial\omega$ and $y \in D$ we can consider the *geodesic distance* $d_\omega(x, y)$, i.e. the length of the shortest curve contained in $D \setminus \omega$ connecting x and y. Then it is obvious how an accessibility criterion can be formulated: if $d_\omega(x, y)$ equals the Euclidean distance, then x is accessible from y. For fixed y, the distance $x \mapsto d_\omega(x, y)$ can be computed efficiently using fast marching methods as the one described in [50].

An illustration of a possible analysis of the optimal orientations that can be chosen for a given structure is given in Figure 2.4. The U-shaped tube contains inaccessible regions. Taking these into account when minimizing the surface area of overhang regions completely changes the final orientation. In figures where two arrows are shown, the red one corresponds to the minimization of the area of overhang regions, while the green one corresponds to the minimization of the projection on the plane of the roller. More examples and details are shown in [A9].

2.4 Linearized elasticity context

Consider the build chamber D and a fixed shape $\omega \subset D$ with a given fixed orientation. The support structures are represented by the shape $S \subset (D \setminus \omega)$. The goal is to assign an objective function $S \mapsto J(S)$ based on the discussion in Section 2.2 that when optimized would yield supports that are in accord with the industrial requirements. A secondary goal, that guided our modelization choices, is the efficiency of the shape optimization algorithm. A usual requirement is that the simulation process should finish in shorter time than the fabrication process, allowing possible iterations and improvement of the support structures.

A natural idea is to search for supports that are as stiff as possible under different loadings, when using the linearized elasticity equation. For simplicity, the objective function used for the initial examples is the **compliance**, which leads to a self-adjoint problem, efficient from the computational point of view.

(a) Gravity-like forces. The first option we tried is to consider the optimization of the support S such that the structure $S \cup \omega$ is the stiffest when considering volumic downward pointing forces in ω. The fact that the supports can attach to the baseplate is modelized by assigning a Dirichlet boundary condition on the lower face Γ_D of D. Numerical simulations are performed in FreeFEM [66] based on the level-set method [113], [7]. The theoretical and numerical considerations are detailed in [A8].

It can be observed that the supports obtained through the optimization process connect

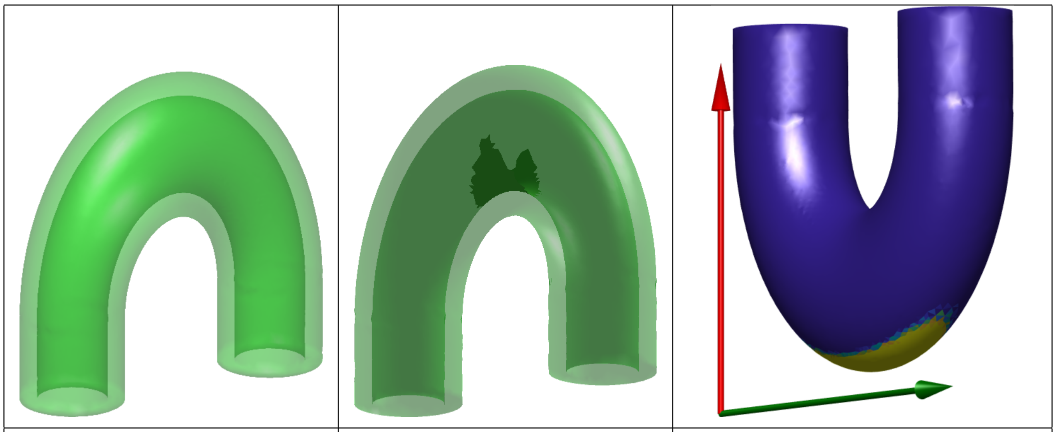

1. U-shaped tube | 2. Inaccessible regions | 3. Area Supported Reg: $\mathcal{G}_1$

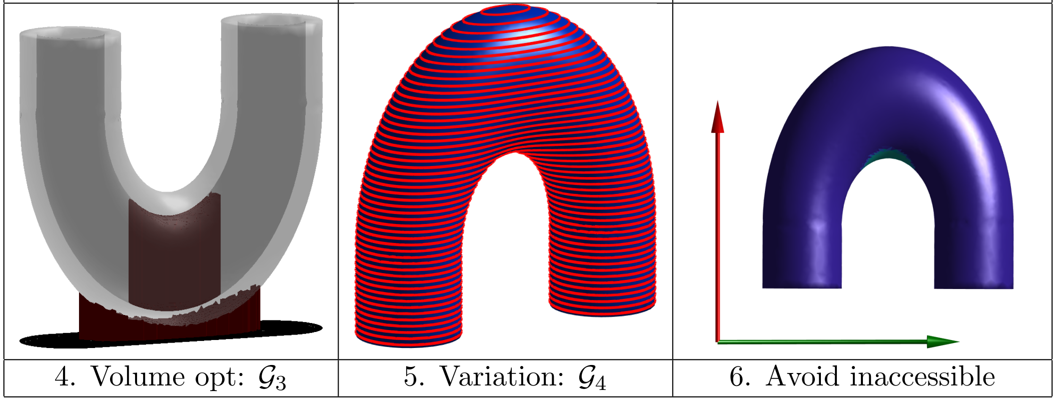

4. Volume opt: $\mathcal{G}_3$ | 5. Variation: $\mathcal{G}_4$ | 6. Avoid inaccessible

Figure 2.4: Case study: U-shaped tube. The various criteria considered are illustrated including the detection of inaccessible regions.

the baseplate to various parts of the structure, increasing its stiffness. Nevertheless, these supports are not in agreement with practical requirements, since large overhanging regions are not supported. In [A8] we also consider the optimization of the supports with respect to the evacuation of the heat towards the baseplate and the simultaneous optimization of the shape and supports. For the latter, two level-set functions are used, allowing to capture the part, the support and the powder regions. Different parts of the boundaries give rise to different shape derivative formulas, which are detailed in the paper. Motivated by the paper [3] we also propose a layer-by-layer model which yields similar results, but is more costly from a numerical point of view. Some of these aspects of simultaneous shape/support optimization are developed further in the thesis of M. Bihr [23].

(b) Surface forces acting on overhangs. To force the support to attach to overhanging regions we consider again a linearized elasticity problem in $D \setminus \omega$ with downwards pointing surface loads on overhanging regions $\Gamma_\beta(\partial\omega)$. Dirichlet boundary conditions are considered on the baseplate and, possibly, on certain parts of $\partial\omega$ where the support is allowed to be attached. Examples of supports obtained with this type of modelization are shown in Figure 2.6. It can be observed that all overhanging regions on $\partial\omega$ are supported.

From a practical point of view, we use the software MMG [48] to create a mesh of $D \setminus \omega$, the design space for the supports S. Starting from an STL file, a triangulation is obtained and adding a rectangular box around this triangulation allows us to obtain the desired mesh. FreeFEM is used to identify and relabel overhanging regions and regions where the support may attach. The process is illustrated in Figure 2.7.

In Figure 2.8 the optimization of supports is considered, using vertical surface loads on the U-shaped structure. Two cases are considered: the Dirichlet boundary condition is applied on the baseplate and on some parts of the shape ω and secondly, the Dirichlet boundary condition

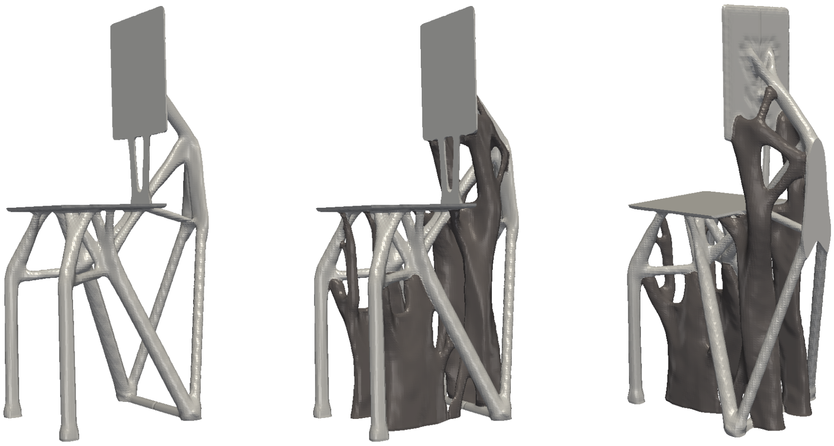

Figure 2.5: Fixed shape (left) and two views of the optimal supports.

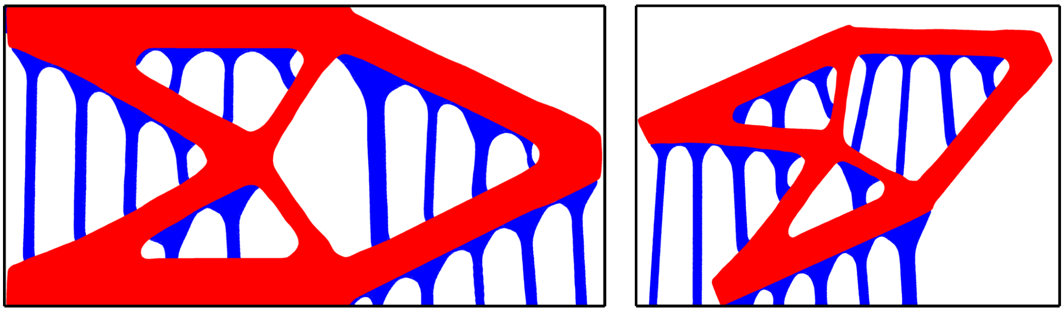

Figure 2.6: Optimized supports obtained by minimizing the compliance for vertical loadings, limit angle $\beta = 45^\circ$ and two different build orientations.

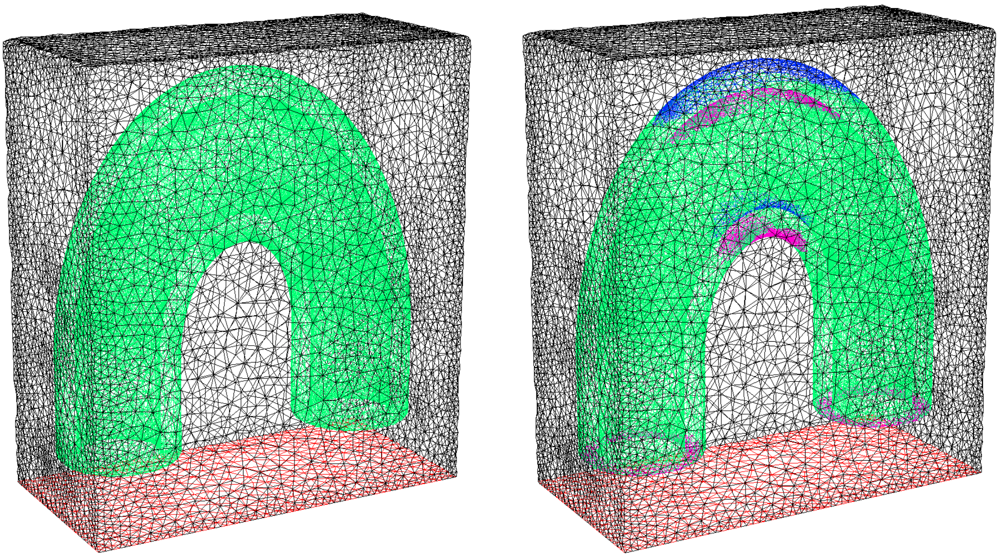

Figure 2.7: Mesh around the U-shaped tube ω obtained with MMG (left). Mesh with different colors for the different parts of the boundary of ω (right): green - free boundary, red - baseplate, purple - overhang regions Γ_β for $\beta = 45^\circ$, blue - regions of $\partial\omega$ where the support may attach.

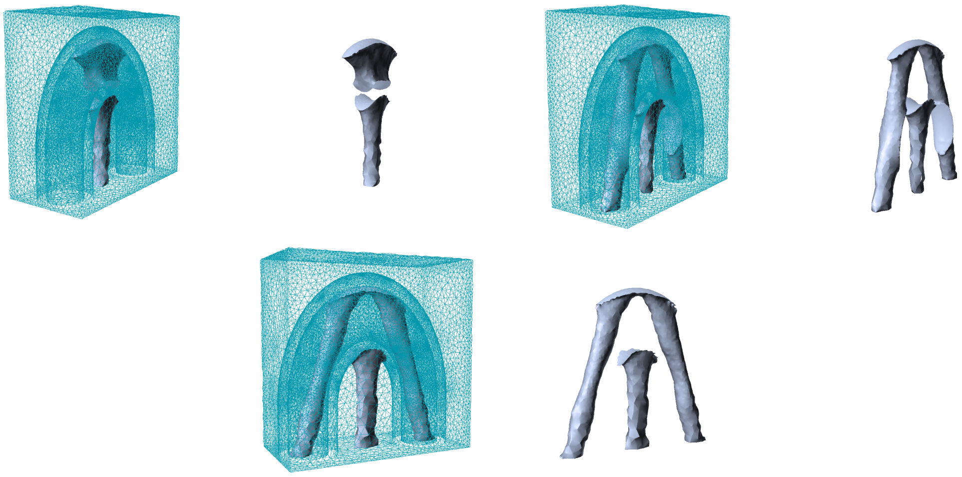

Figure 2.8: Optimized supports for minimal compliance under pseudo gravity loads. Upper left: $u = 0$ is imposed on a part of $\partial\omega$ and on the baseplate. Upper right: $u = 0$ is imposed only on the baseplate. Bottom: addition of a penalization term.

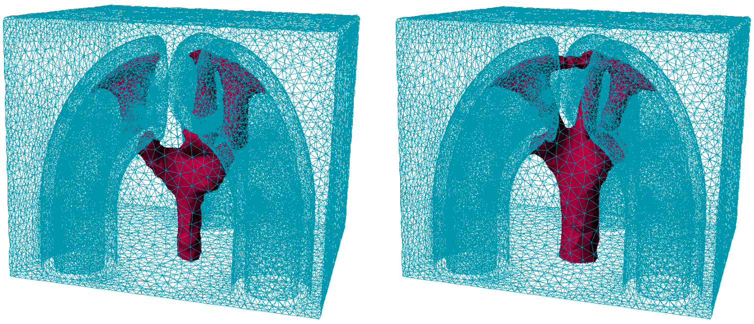

Figure 2.9: Optimized supports for minimal compliance under pseudo gravity loads for three copies of half-tubes: supports allowed to attach on the shapes (left), supports not allowed to attach on the shapes (right)

is considered only on the baseplate.

The motivation behind this is the post-processing cost of contact surfaces between the part and the support, discussed in Section 2.2. It turns out that changing the Dirichlet boundary condition so that the support can only attach on the baseplate is not enough to avoid the contact between the part and the support, as can be observed in the second case presented in Figure 2.8. In order to prevent this unwanted contact, an additional term is added in the objective function, penalizing the contact area between the support and the part. Adding this contact surface penalization term produces support structures that do not touch the shape ω, shown again in Figure 2.8. More details regarding the test cases and the implementation are given in [A9].

There are multiple possible extensions for such support optimization procedures. One idea is to consider mutualized support structures when multiple shapes need to be printed on the same plateau. An example in this sense, where three half tubes are considered inside the same mesh is shown in Figure 2.9. The optimization algorithm gives a single support structure supporting all overhanging regions, considering again the case where the support can attach to the shape or not. Up to this point, the optimization of support structures was only subjected to volume constraints. Therefore the resulting support structures may have overhangs themselves. A strategy to prevent this is a work in progress and is presented in the perspectives section.

2.5 Optimization of thermoelastic criteria using a simplified simulation model

The work described in this section is described in detail in [A5] and is part of the PhD thesis of Martin Bihr [23], which I co-supervised with Grégoire Allaire. As underlined in Section 2.2, the melting and cooling of the successive layers of the part can lead to high internal stresses and possible deformations of the printed object. In order to understand these thermo-mechanical phenomena before starting the fabrication process, numerical simulations should be performed. A complete thermo-mechanical simulation of the process has a high computational cost, since a number of PDEs proportional to the number of layers need to be solved, keeping all history in memory. From the point of view of numerical shape optimization this is especially costly, since such a simulation should be repeated at each iteration of the optimization process. Such a complete simulation approach is described in [122] and [4]. In the following, we propose a simpler model, which manages to capture the qualitative behavior of the fabricated structures while being computationally cheaper.

The inherent strain method consists in decomposing the total strain ε into its elastic part and the inelastic contribution

$$\varepsilon = \varepsilon_e + \varepsilon^*,$$

and suppose that ε^* is known. To find the inherent strain tensor ε^* corresponding to a given set of machine parameters a test part is manufactured, and ε^* is tuned such that the deflection measured experimentally corresponds to the one obtained numerically. More details and bibliographical references regarding this method are given in [A5].

Let us consider a shape ω contained in the build chamber D. The build chamber is divided into M layers $\mathcal{L}_i$ and the intermediate domains D_i are defined as tie union of the first i layers, for every $1 \leq i \leq M$, leading to a sequence of domains D_i verifying

$$D_1 \subset ... \subset D_i \subset ... \subset D_M \equiv D.$$

The baseplate, i.e. the bottom of the build chamber D, is denoted by Γ_D. For all $1 \leq i \leq M$ consider the intermediary shapes $\omega_i = \omega \cap D_i$. For each $1 \leq i \leq M$ consider the solutions $u_i \in H^1_{\Gamma_D}(\omega_i)^d$, i.e. $u \in H^1(\omega_i)^d$ with $u_i = 0$ on Γ_D verifying the inherent strain problem

$$\left\{ \begin{array}{rcll} -\operatorname{div}(\sigma_i) & = & 0 & \text{in } \omega_i \\ \sigma_i & = & A(e(u_i) + \varepsilon^*_{\mathcal{L}_i}) & \text{with } \varepsilon^*_{\mathcal{L}_i} = \varepsilon^* \chi_{L_i} \\ \sigma_i n & = & 0 & \text{on } \partial\omega_i \setminus \Gamma_D \\ u_i & = & 0 & \text{on } \Gamma_D \cap \partial\omega_i. \end{array} \right. \tag{2.1}$$

The constant inherent strain ε^* has diagonal entries $\{-10^{-4}, -10^{-4}, 0\}$ and was chosen based on the one used in the *Simufact Additive* software. One advantage of problem (2.1) is that displacements u_i found for each layer are independent. In particular, they can be computed in parallel, further improving the computational efficiency. We tested our basic FreeFEM [66] implementation and obtained results giving qualitative agreement with simulations made with Simufact for different test cases, as shown in [A5, Section 2].

The simplified simulation model allows us to efficiently optimize numerically various criteria related to the SLM manufacturing process. Compared to [4] there is no need to compute the solutions to the heat equations at each layer, the corresponding information being encoded in the inherent strain tensor ε^*. In the numerical simulations a volume constraint was imposed, as well as a final usage constraint, corresponding to an inequality constraint on the compliance given by a linearized elasticity problem. The context is described in [A5, Section 3].

The criteria optimized in this work are shown below:

- **Minimization of the vertical displacements.** In order to prevent the collision of the powder deposition system with the part, the positive vertical displacements should be

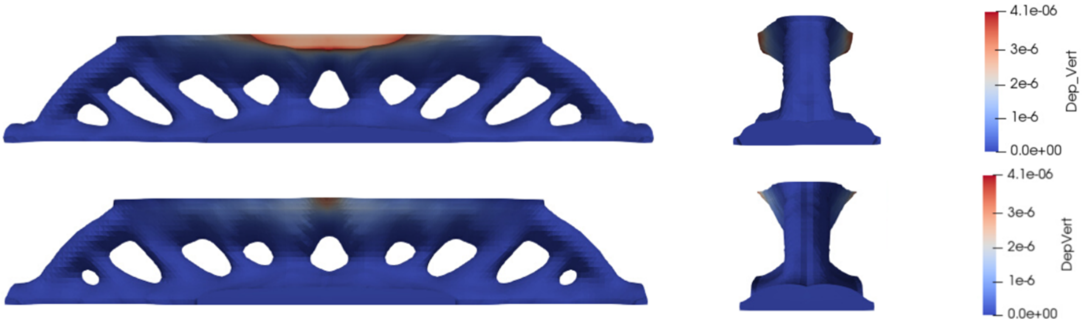

Figure 2.10: Minimizing the total vertical displacements.

limited as much as possible. In practice it is observed that such vertical displacements appear in particular on overhanging regions. In [A5, Section 5.1] an example is given, shown in Figure 2.10. It can be observed that the optimization process removes the massive overhanging part in the original design. This result is remarkable since the removal of overhaning regions is usually achieved using geometric criteria, while in this case a purely mechanical model is used.

- **Minimizing a Von Mises criterion.** The Von Mises field gives information about the total stress accumulated in different parts of the manufactured shape. It is generally agreed that this quantity should be decreased to prevent the occurrence of cracks and distortions in the printed object. An example of optimization in this sense is shown in [A5, Section 5.2].
- **Minimization of the residual displacement after plate separation.** After the 3D printing process is finished, the contraction of the successive layers leads to residual constraints in the part. The printed object is clamped to the baseplate Γ_D and cutting it will lead to potential deformations when the corresponding constraints are released. We model these deformations as follows. First, an inherent strain simulation with the part clamped on Γ_D gives us information about the constraints present in the part at the end of the printing process. Next, we solve another mechanical problem giving the displacement v of the part after the cut. In this problem, the stress given by the previous simulation is used as a load, considering that the part is clamped only on a smaller subset Γ_{D_0} of Γ_D. Next, we consider the minimization of the maximal vertical positive displacement given by v in the shape ω. The details, equations and a numerical test can be found in [A5, Section 6] and an experimental validation of the procedure is shown in Figure 2.11.

Following the presented simulations, an experimental assessment was performed at Safran. This experiment validated our numerical simulations in the following aspects:

- Parts optimized for minimizing vertical displacements displayed lower vertical displacements for some of the layers studied.
- Parts optimized for minimizing the displacement after plate separation displayed a lower vertical displacement, measured after the manufacturing process.

A calibration procedure was also proposed, following the experimental measurements, allowing to recover the coefficients of the inherent strain tensor. All details regarding the experimental work and the calibration procedure are given in [A5, Section 7].

2.6 Imperfect interface models

The content of this section is obtained in collaboration with G. Allaire and M. Godoy (postdoc in the SOFIA project) and is described in detail in [A10] and [A11]. The motivation for this work comes from the post processing cost related to the removal of support structures. In some applications, a weaker part/support contact region is designed, allowing the removal of supports

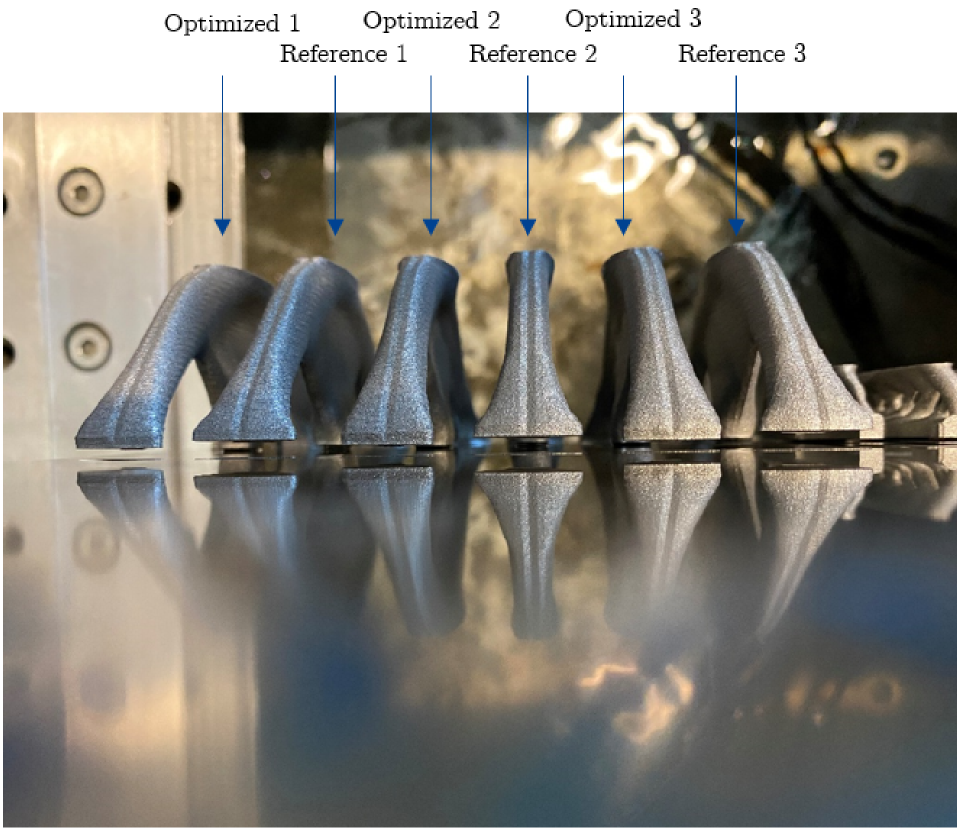

Figure 2.11: Partially cut parts optimized for minimizing vertical displacement after baseplate separation. The practical experimentation is part of M. Bihr's thesis [23].

by hand. Therefore, such weak contact regions do not behave mechanically in the same way as in a perfect interface setting. See Figure 2.12 for examples.

Consider a structure $\omega \subset \mathbb{R}^d$ and its supports represented by the shape $S \subset \mathbb{R}^d$. The interface between ω and S is denoted with Γ. Contrary to the context of Section 2.4, we consider displacements u which have components that are in H^1 when restricted to ω and S, but are not necessarily globally H^1. In particular, displacements u can be discontinuous along the interface Γ between S and ω and we denote by $[u] = u_S - u_\omega$ the jump of u across the interface Γ. Using the usual notations $e(u)$ (the symmetrized gradient) and

$$\sigma(u) = Ae(u) = 2\mu e(u) + \lambda \operatorname{div} u \, \mathbf{Id}$$

where λ and μ are the Lamé coefficients (potentially different in ω and S) we solve the following problem:

$$\begin{cases} u_{|\omega} = u_\omega \in H^1(\omega), u_{|S} = u_S \in H^1(S), u = 0 \text{ on } \Gamma_D \\ \int_\omega \sigma(u_\omega) : e(u_\omega) dx + \int_S \sigma(u_S) : e(u_S) dx + \int_\Gamma R^{-1}[u] \cdot [v] ds = L(v), \end{cases} \tag{2.2}$$

for all v verifying the same hypotheses as u. The linear form L models the different loadings that can be applied to the structure. The second order tensor

$$R = \alpha(\mathbf{Id} - \nu \otimes \nu) + \beta \nu \otimes \nu,$$

where ν is the normal vector to the interface Γ between S and ω pointing inside ω, models the rigidity of the structure at the contact interface Γ. In particular, parameters α and β model the stiffness of the structure $\omega \cup S$ along the interface Γ in the normal and tangential directions,

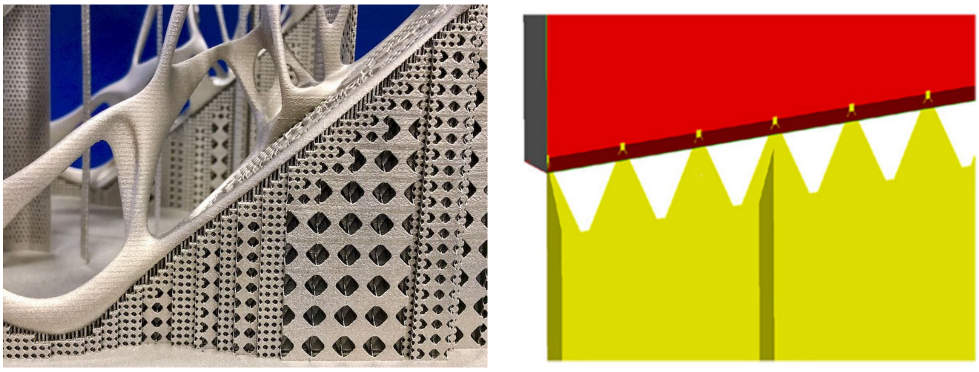

Figure 2.12: Support structures having a weak contact interface with the part, facilitating their removal.

respectively. When $\alpha, \beta \to 0^+$ we recover the perfect interface case, where the displacement is continuous along Γ, i.e. $[u] = 0$. Details in this sense are given in [A11, Section 2].

One can observe that standard piecewise affine finite elements are not enough to approximate solutions of (2.2) numerically. Notably, on the interface Γ the jump $[u] = u_S - u_\omega$ is present and needs to be computed numerically. The approach we chose is to consider two piecewise affine vector fields, one for u_ω and another one for u_S. We add additional terms in (2.2) with a small coefficient, ensuring that the resulting numerical problem is well posed. In practice, we consider a bounding box D and we mesh exactly ω and $D \setminus \omega$, ensuring that the interface Γ is always exactly meshed. The supports S are represented with a level-set function defined on $D \setminus \omega$. From a practical point of view, the resulting numerical problem has twice the size as the usual linearized elasticity problem, leading to costly computations, especially in dimension three.

Numerical results shown in Figure 2.13 show how the rigidities α, β influence the optimized support structures. The loading case considered corresponds to vertical, gravity like forces acting in the part ω and the objective function is the compliance. As the parameters α, β increase, the interface becomes weaker in the tangential and normal directions, respectively. The perfect interface yields supports resembling vertical pillars similar to the configurations obtained in [A8] in the perfect case. When the interface is weak in both tangential and normal directions, support structures become massive and go above the structure ω. A weakly tangential interface yields again vertical pillars, as the structure considered has substantial horizontal parts. A weakly normal interface gives supports concentrated on the edge of the overhanging parts, where the tangential attachment of the supports to the part aligned with the direction of the loads is more substantial. Although the supports obtained through this type of models is not in agreement with the industrial requirements underlined in Section 2.2, this study shows how a purely mechanical model related to the strength of the interface contact influences the resulting support structures.

2.7 Perspectives

The works presented in this chapter give rise to the following natural perspectives:

(i) Control of overhanging regions in the support being optimized. In the simulations presented previously a volume constraint is imposed on the support structures. This does not prevent optimized supports having themselves unwanted overhanging parts in their boundary. In the paper [119] a functional for quantifying overhangs in the level-set framework is proposed. Based on this, we can consider the following functional based on the signed distance function, which can be used to control overhanging regions. Given $\omega \subset D$ and d_ω its signed distance function, consider

$$J(\omega) = \int_{\omega_c} (\nabla d_\omega \cdot (-\vec{d}) - \cos\beta)_+^2, \tag{2.3}$$

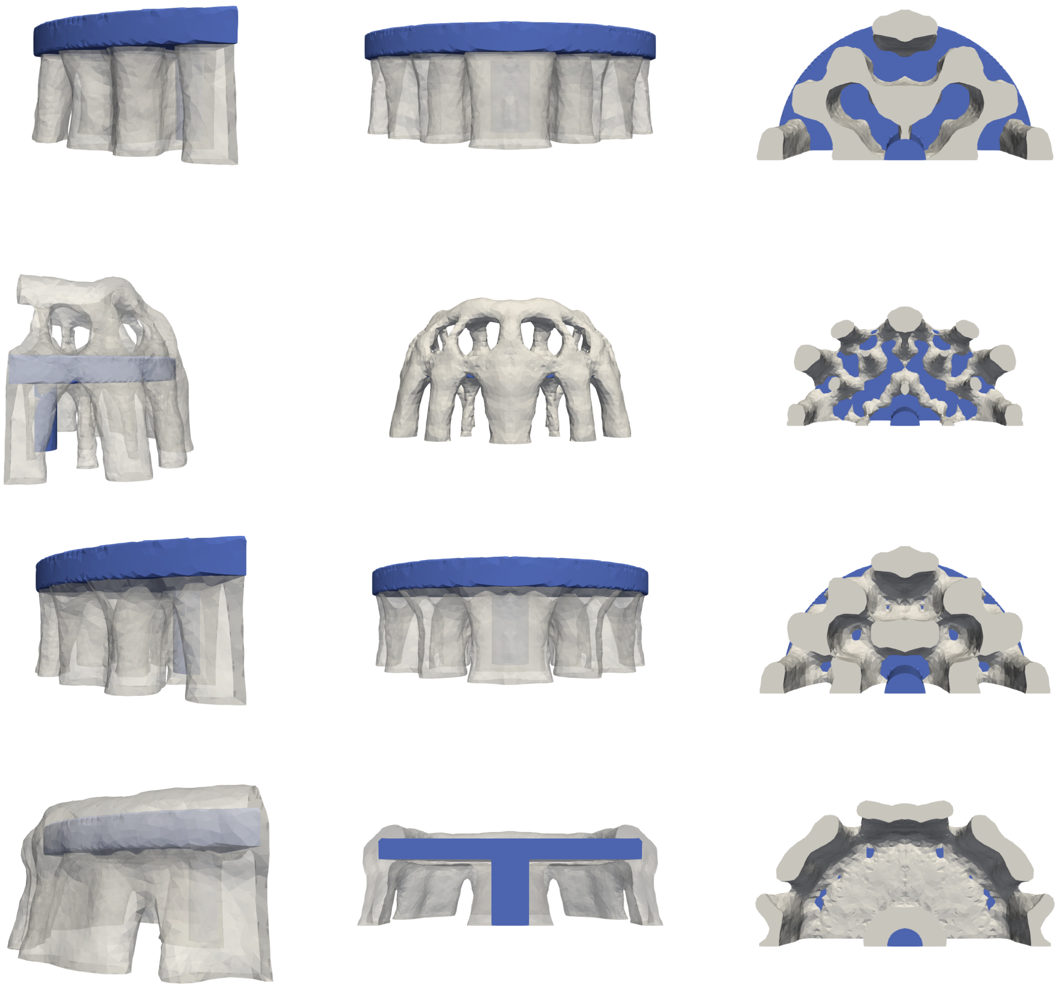

Figure 2.13: Different views of the optimized designs: perfect interface (upper row), $\alpha = \beta = 400$ (2nd row), $\alpha = 100, \beta = 1$ (3rd row) and $\alpha = 1, \beta = 100$ (lower row).

where, as usual $\vec{d}$ denotes the build direction. This functional has multiple advantages compared with, for example, the perimeter of overhanging regions. The latter creates a *dripping effect* as shown in [3]. The functional (2.3) has non-zero contribution when downward pointing spikes are present, eliminating these effects. The shape derivative of (2.3) can be computed using the methods described in [57].

(ii) Parallelization of the computations. Computations described in this chapter are realized using FreeFEM [66] coupled with toolboxes Advect [40] and Mshdist [50] used for advection and re-initialization of level-set functions. In all simulations, the main part of the computational cost is the resolution of the PDEs involved in the corresponding models. Parallel capabilities of FreeFEM could be used to accelerate this process, especially for complex models needing multiple solves per iteration (like those shown in Section 2.5). Moreover, the advection and re-initialization of the level set as a distance function could also profit from parallel computing. Examples of parallel implementations of shape and topology optimization problems using FreeFEM [66] are given in [58] and [53] for the case of body fitted meshes. These frameworks could be extended to the where the optimized shape is represented using level-set defined on a fixed mesh.

(iii) Optimization related to accessibility criteria. In Section 2.2 we recall that support structures need to be removed at the end of the manufacturing process. In particular, supports should not attach to non-accessible regions. The accessibility of a certain region can be defined in multiple ways, for example considering straight lines from some source points to the boundary of the part to be supported. From a shape optimization point of view, accessibility criteria that allow shape differentiability are of special interest. Initial work in this direction is done in the final chapter of the PhD thesis of M. Bihr [23] and is the subject of a work in progress.

Chapter 3

Numerical shape optimization for convex sets

3.1 Introduction

Problems investigated in this chapter have the form $\min_{\omega\in\mathcal{A}} \mathcal{F}(\omega)$, where $\mathcal{A}$ is a family of convex sets with additional constraints. I focus on aspects related to the numerical handling of constraints coming from convex geometry (convexity, diameter, constant-width, inclusion), using well adapted functional parametrizations of convex sets.

The study of shape optimization problems in the class of convex sets has particular features. The existence of solutions is often facilitated by the compactness properties underlined by the Blaschke selection theorem [112, Chapter 1]: a sequence of convex shapes included in a large ball contains a subsequence converging in the Hausdorff metric. The study of the regularity of optimal shapes via optimality conditions is more difficult. Parts of the optimal shapes where the convexity constraint is saturated (for example segments in the boundaries) cannot be perturbed with arbitrary vector fields. The papers [70], [85], [86] describe some of the theoretical challenges that appear working with such constraints.

Numerical tools for approximating solutions to shape optimization problems are useful in this context since in many cases the theoretical tools cannot describe completely the optimal shapes. In such cases, new leads for theoretical study and new conjectures can arise from properly designed numerical simulations. The goal of this chapter is to underline my contributions to this area of research described in a series of publications: [A12], [A1], [A2], [A14]. Difficulties underlined previously, regarding admissible domain perturbations, are also reflected in the numerical study. In the article [16] the authors answer this challenge using perturbations which preserve convexity. The approaches described in this chapter use a parametric formulation and exploit the fact that convex shapes admit efficient functional parametrizations based on the support function and the gauge function.

There are works in the literature which propose algorithms that can handle the convexity constraint. In [83] a method is proposed in which the convex shapes are represented as intersections of half-spaces. In [96] the authors propose a method of projection onto the class of convex shapes. The articles [20], [84], [104] show how to deal with width constraints using various formulations. The methods presented in the previous references are rather complex and not straightforward to implement.

The work presented in this chapter was motivated by the search of a more direct approach to shape optimization among convex sets, allowing more flexibility in the choice of constraints and functionals to be minimized. This is made possible starting from the properties of the support function. This idea was initially proposed in [19] for the study of shapes of constant width, further extended in the habilitation thesis [18]. However, the numerical framework used in [19], [18] needs special tools regarding semi-definite programming algorithms and the cost functional is at most linear or quadratic in terms of the Fourier coefficients of the support function. In [A12] and [A1] we extend this framework to arbitrary functionals including three dimensional simulations.

The discretization strategies using the support function can be described as follows:

- Strictly convex shapes have support functions of class at least C^1. Therefore, a truncated spectral decomposition of the support function allows an efficient way to parametrize such shapes. The numerical framework is presented in Section 3.3, based on the publications [A12] and [A1].
- One drawback when using spectral decomposition for approximating support functions of convex shapes is the exclusion of segments in the boundary. As recalled in Section 3.2, the support function is not differentiable for orientations corresponding to segments in the boundary. On the other hand, shape optimization problems in the class of convex sets often have solutions containing segments in the boundary, illustrating the competition between the convexity constraint and the behavior of the functional to be minimized. In order to capture segments in the boundary, in [A2] a discretization strategy using the values of the support function on a discretization of $[0, 2\pi]$ is employed. Furthermore, a completely rigorous approach, guaranteed to produce discrete convex shapes is given in [A14]. These aspects are detailed in Section 3.4.

In Section 3.2 various results regarding the support and functions associated to convex sets are recalled. In Section 3.3 strictly convex shapes are parametrized using a truncated spectral decomposition of the support function. In Section 3.4 the framework is extended to arbitrary convex sets using the values of the support function at a discretization of $[0, 2\pi]$. Section 3.5 shows various applications based on the methods described and gives more details regarding the numerical framework, including examples of fully working codes that are made available online on Github: `https://github.com/bbogo/ConvexSets`. We conclude with an overview of the perspectives of this work in Section 3.6.

3.2 Functional parametrizations of convex sets

3.2.1 The support function

A convex body $K \subset \mathbb{R}^d$ is a compact convex set with non-void interior. The support function $h_K : \mathbb{S}^{d-1} \to \mathbb{R}$ of a convex body $K \subset \mathbb{R}^d$ is defined by

$$h_K(u) = \max_{x \in K}(x \cdot u) \tag{3.1}$$

or alternatively, $h_K(u)$ is the distance from the origin to the supporting plane orthogonal to the direction $u \in \mathbb{S}^{d-1}$. An illustration for the two dimensional case is given in Figure 3.1. It is also possible to define the support function on the whole space $H_K : \mathbb{R}^d \to \mathbb{R}$ by

$$H_K(u) = \max_{x \in K}(x \cdot u), \tag{3.2}$$

and note that $h_K = H_K(u/|u|)$ when $u \in \mathbb{R}^d \setminus 0$. In other words, H_K is the positive 1-homogeneous function which coincides with h_K on the unit sphere. The concept of support function is classical in convex geometry and the reader can consult [112] for more details and properties. By definition, the support function is well adapted for handling width and diameter constraints, since $h_K(u) + h_K(-u)$ represents the distance between the two tangent hyperplanes to K orthogonal to $u \in \mathbb{S}^{d-1}$.

The definition above shows, in particular, that the support function is well adapted for dealing numerically with width or diameter constraints. This was already observed in the previous works [A1], [19], [A12] or [A2].

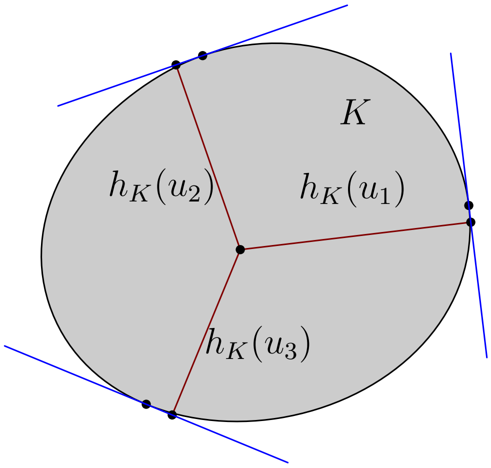

Figure 3.1: Illustration of the support function of a convex body.

In Figure 3.2 two examples of shapes and their associated support functions are shown, for the classical Reuleaux triangle and a stadium like shape. In [112, Cor 1.7.3] it is shown that at all points where the supporting plane intersects K at exactly one point, the support function is differentiable. In particular, as shown by the example of the stadium, segments in the boundary of a two dimensional convex domain produce discontinuities in the first derivative of the associated support function. Therefore, the discretization of the support function should allow such discontinuities in the derivative in order to capture segments in the boundary.

For a convex compact body $K \subset \mathbb{R}^2$ consider the associated support function h_K defined by (3.1). Let us briefly recall some of the basic properties of the support function. For a complete exposition with proofs the reader can consult [112, Section 1.7]. We parametrize the unit circle $\mathbb{S}^1$ using $u = (\cos\theta, \sin\theta)$ with $\theta \in [0, 2\pi]$. Therefore, in the following, we identify the support function h_K with a continuous 2π periodic function $p : [0, 2\pi] \to \mathbb{R}$. For $\theta \in [0, 2\pi]$ denote the associated normal and tangential vectors $\mathbf{r}(\theta) = (\cos\theta, \sin\theta)$ and $\mathbf{t}(\theta) = (-\sin\theta, \cos\theta)$. The set $H(K, \theta) = \{x \in \mathbb{R}^2 : x \cdot \mathbf{r}(\theta) = p(\theta)\}$ is called the support line of K at θ. The set $F(K, \theta) = K \cap H(K, \theta)$ is called the support set of K at θ. In [112, Section 1.7] it is shown that p is differentiable at θ if and only if the associated support set $F(K, \theta)$ contains only one point. An immediate consequence is that segments in the boundary of K correspond to parameters θ where the support function has a discontinuity in the first derivative. In particular, constant width shapes have support functions at least of class C^1, since they do not contain non-trivial segments in their boundaries. The proof is straightforward and can be found, for example, in [74, Exercise 7-3].

In view of the discussion above, the support function p of a strictly convex shape $K \subset \mathbb{R}^2$ is of class C^1. It is classical (see [19], [A1] and references therein) that in this case, a parametric representation of ∂K is given by $\mathbf{x}(\theta) = p(\theta)\mathbf{r}(\theta) + p'(\theta)\mathbf{t}(\theta)$ or, more explicitly,

$$\begin{cases} x_1(\theta) = p(\theta)\cos\theta - p'(\theta)\sin\theta, \\ x_2(\theta) = p(\theta)\sin\theta + p'(\theta)\cos\theta. \end{cases} \tag{3.3}$$

It is straightforward to see that at points where the support function p is C^2, the tangent vector at the curve with the parametrization (3.3) is given by $(p(\theta) + p''(\theta))\mathbf{t}(\theta)$. In [19], the convexity of K is characterized by

$$p(\theta) + p''(\theta) \geq 0 \text{ for every } \theta \in [0, 2\pi]. \tag{3.4}$$

At points where p is at least C^2, the condition above is clear. As underlined in [17], [19], when p is of class $C^{1,1}$, the constraint may also be interpreted in the sense of distributions, including

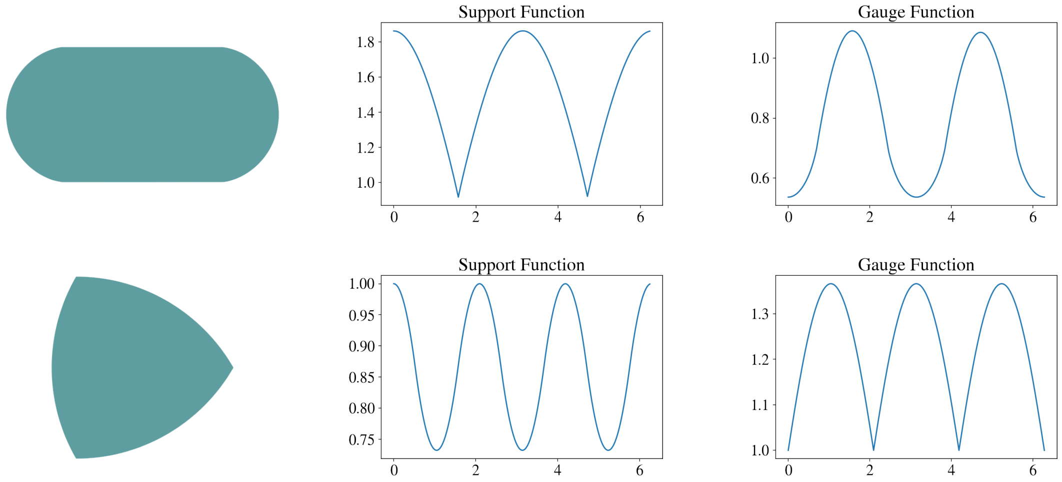

Figure 3.2: Two examples of convex shapes together with their support and gauge functions. Segments in the boundary correspond to singular points for the support function. Angular points generate singularities for the gauge function.

points where p'' is not defined. In dimension three the corresponding parametric representation and convexity constraint become more involved, as shown in [A1].

3.2.2 The gauge function

Another natural parametrization of convex sets can be achieved using radial functions with respect to an interior point. In dimension two it turns out that the inverse of the radial distance to a fixed origin has properties which allows again the use of efficient numerical methods for discretizing convex shapes. Given $K \subset \mathbb{R}^2$ a convex set containing the origin, consider $\rho_K : [0, 2\pi] \to \mathbb{R}_+$ to be a radial function for K. In other words, $\theta \mapsto \rho_K(\theta) \begin{pmatrix} \cos\theta \\ \sin\theta \end{pmatrix}$ is a parametrization for ∂K. This allows us to define the associated gauge function $\gamma_K : [0, 2\pi] \to \mathbb{R}_+$ by

$$\gamma_K(\theta) = 1/\rho_K(\theta). \tag{3.5}$$

The gauge function is related to the support function via the polar body. Given a convex body K, the polar body is $K^\circ = \{y \in \mathbb{R}^d : x \cdot y \leq 1, \forall x \in K\}$. The gauge function of the body K is equal to the support function for K°. See [112] for more details. Compared with the support function, the gauge function has singularities at angular points (instead of segments). Two examples are shown in Figure 3.2 illustrating the smoothness of the gauge function for segments in the boundary and singularities coming from angular points. Details regarding the usage of the gauge function in numerical simulations are presented in Section 3.4.

The usage of the gauge function rather than the radial function for parametrizing convex sets is further motivated by the simplicity of the convexity condition when using the gauge function. Indeed, it can be shown that in dimension two, if γ_K is of class C^2 convexity is equivalent with

$$\gamma_K(\theta) + \gamma_K''(\theta) \geq 0,$$

for every $\theta \in [0, 2\pi]$. One can observe that this condition is the same as (3.4) for the support function. From a numerical point of view, the analogue discrete constraints should be investigated as shown in Section 3.4.

3.3 Spectral decomposition of the support function

The initial motivation for finding an appropriate framework for numerical shape optimization among convex set was the article [A12], where we study the minimization of the k-th eigenvalue of the Dirichlet-Laplace operator under diameter constraint

$$\min_{\operatorname{diam}(\Omega)=d} \lambda_k(\Omega). \tag{3.6}$$

Eigenvalues λ_k are decreasing with respect to set inclusion: $\omega_1 \subset \omega_2 \Rightarrow \lambda_k(\omega_1) \geq \lambda_k(\omega_2)$. Taking the convex hull preserves the diameter and decreases the k-th eigenvalue, therefore we may assume that admissible shapes in (3.6) are convex. Problem (3.6) has solutions due to the Blaschke selection theorem and the continuity of the eigenvalues for the Hausdorff convergence of convex sets [68, Section 2.3.3]. Since the Dirichlet-Laplace eigenvalues are decreasing under domain inclusion, solutions of problem (3.6) are maximal sets for a given diameter, therefore they are *constant width* sets. The paper [19] already proposed a framework for shape optimization in the class of constant width sets, where a truncated spectral decomposition of the support function is used in dimension two. The convexity constraint is handled in a rigorous way, using semi-definite programming techniques and specialized software. Aspects related to the three dimensional case are discussed in the habilitation thesis of T. Bayen [18, Chapter 5]. An alternative way of imposing the convexity constraint was proposed in [9], where (3.4) is imposed only on a discrete subset of $[0, 2\pi]$. This results in a set of linear inequalities for the Fourier coefficients, allowing straightforward implementation using standard optimization software like `fmincon` in Matlab or `IPOPT`. Although this approximation is not as rigorous as the analytic approach in [19], when imposing (3.4) for sufficiently many points on the unit circle the numerical algorithm behaves well. Furthermore, there is no limitation concerning the objective function used in this context, as long as the shape derivative is known.

In dimension two, the numerical setting consists in working with support functions given by

$$(a_0, a_1, ..., a_n, b_1, ..., b_n) \mapsto p(\theta) = a_0 + \sum_{k=1}^{n} (a_k \cos(k\theta) + b_k \sin(k\theta)). \tag{3.7}$$

In view of the discussion in Section 3.2, p given by (3.7) can only be a support function of a strictly convex set. Constant width sets are strictly convex and, therefore, it is not restrictive to use such a parametrization in this context. Different constraints can be imposed in this setting:

- **convexity**: impose (3.4) for $\theta = 2\pi j/M$, $j = 0, ..., M-1$ resulting in a series of linear inequality constraints for the Fourier coefficients in (3.7).
- **constant width**: $p(\theta) + p(\theta + \pi) = w$ is characterized by $a_{2k} = b_{2k} = 0$ for $k \geq 1$, i.e. the even part of the spectral decomposition is constant.

Moreover, various geometric quantities like the area and perimeter have explicit expressions in terms of the coefficients of the parametrization given in (3.7), as recalled in [A1].

The three dimensional case is more involved, although similar ideas are used. The support function is approximated using spherical harmonics. The convexity constraint can be reduced to the positivity of the Gaussian curvature in dimension three, which can be imposed on a large enough family of points on the unit sphere, giving rise to a set of non-linear differentiable inequality constraints. More details regarding the discrete framework in dimensions two and three are given in [A1]. In the same work we prove that working with truncated spectral decomposition is not restrictive in the following sense: solutions for parametric optimization problems for support functions given by (3.7) converge towards solutions of optimization problems using the full Fourier series as the number of parameters converges to $+\infty$. This result, valid also in dimension three, generalizes the theoretical aspects shown in [19].

Let us now consider a few applications:

- **Minimization of the Dirichlet-Laplace eigenvalues under diameter constraint.** This is the subject of the work [A12]. From a numerical point of view, a first surprising

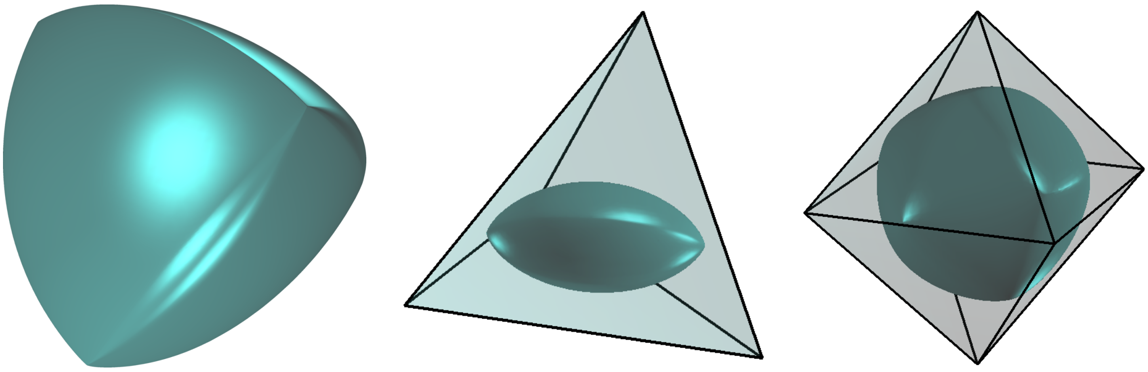

Figure 3.3: Left: Numerical minimization of the volume under constant width constraint in dimension three – the Meissner body. Center-Right: rotors of minimal volume in the regular tetrahedron and the regular octahedron.

result was observing that for $k \in \{1,2,3,4,5\}$ the minimizer is the disk. This is different from the case of volume and perimeter constraints considered in [102], [10], [11], [A13], where the disk is a minimizer only for $k \in \{1,3\}$. This motivated us to look more closely at indices k for which the disk is a local minimizer. The only indices k for which this can occur are $k \in \{1,2,3,4,5,7,8,11,12,16,17,27,33,34,41,42,50\}$. The proof of this fact goes through some delicate estimates involving the Bessel functions. The numerical algorithm allowed us to obtain better candidates than the disk for $k \in \{6,9,10,13,14,15,18,19,20\}$. The corresponding numerical optimal shapes are shown in Table 3.1. A similar analysis could be performed in dimension three. In [A1] we found numerically constant width shapes with smaller eigenvalue than the ball for $k \in \{10,46,99\}$.

- The Blaschke-Lebesgue theorem says that the Reuleaux triangle minimizes the area among shapes with given constant width. The three dimensional analogue problem is still open and it is conjectured that the Meissner bodies obtained by rounding three edges of a Reuleaux tetrahedron are optimal [79]. In [A1] we obtain the two Meissner bodies when minimizing the volume under constant width constraint as a result of a constrained optimization problem starting from random initial coefficients. The result is shown in Figure 3.3. This suggests that the conjecture should be true and Meissner bodies are indeed volume minimizers in the class of three dimensional bodies of constant width.
- Rotors are convex bodies that can turn inside a convex polygon/polyhedron always being tangent to all the edges/faces. In dimension two all regular polygons admit rotors [19], [17]. In dimension three there exist rotors in the regular tetrahedron, the regular octahedron and the cube (these are bodies of constant width). In [95] three dimensional rotors are characterized using the coefficients of the spherical harmonics of the associated support function. Maximal volume rotors are the inscribed balls. Minimal volume rotors are not analytically known and the proposed numerical framework allows us to approximate them numerically. Results obtained with our algorithm are shown in Figure 3.3.

Other applications are shown in [A1], however whenever segments are present in the boundary, the numerical algorithm had difficulties converging. Considering enough coefficients in the spectral decomposition allows to approximate segments in the boundary, but the well known Gibbs phenomenon prevents us to be very precise: the truncated Fourier series of a function f has an oscillatory behavior near a discontinuity of f or f'. Moreover, the behavior does not improve when considering more Fourier coefficients in the decomposition. This shows that as soon as segments are present in the boundary, truncated spectral decompositions of support functions are not appropriate for obtaining reliable numerical results. This motivates the content of the next section.

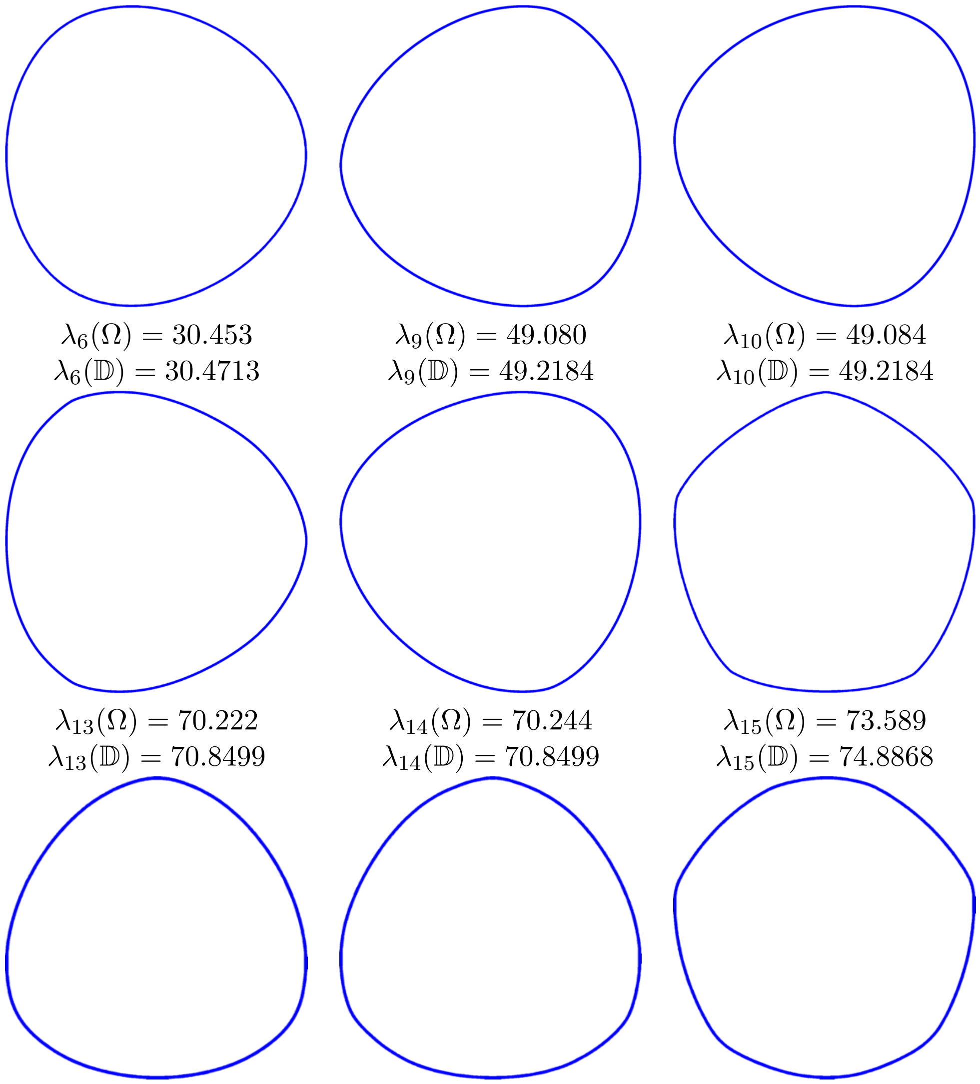

$\lambda_6(\Omega) = 30.453$
$\lambda_6(\mathbb{D}) = 30.4713$

$\lambda_9(\Omega) = 49.080$
$\lambda_9(\mathbb{D}) = 49.2184$

$\lambda_{10}(\Omega) = 49.084$
$\lambda_{10}(\mathbb{D}) = 49.2184$

$\lambda_{13}(\Omega) = 70.222$
$\lambda_{13}(\mathbb{D}) = 70.8499$

$\lambda_{14}(\Omega) = 70.244$
$\lambda_{14}(\mathbb{D}) = 70.8499$

$\lambda_{15}(\Omega) = 73.589$
$\lambda_{15}(\mathbb{D}) = 74.8868$

$\lambda_{18}(\Omega) = 93.626$
$\lambda_{13}(\mathbb{D}) = 95.2776$

$\lambda_{19}(\Omega) = 93.683$
$\lambda_{19}(\mathbb{D}) = 95.2776$

$\lambda_{20}(\Omega) = 98.254$
$\lambda_{20}(\mathbb{D}) = 98.7263$

Table 3.1: Non circular shapes of width 2 which are candidates to be the minimizers of λ_k, for $k = 6, 9, 10, 13, 14, 15, 18, 20$.

3.4 Discrete framework: support and gauge functions

In the article [A2] we investigate shapes maximizing the k-th Steklov eigenvalue under diameter constraints. Recall that for a Lipschitz domain Ω, the Steklov eigenvalues are defined by

$$\left\{ \begin{array}{rcll} -\Delta u &=& 0 & \text{in } \Omega \\ \partial_n u &=& \sigma_k(\Omega) u & \text{on } \partial\Omega, \end{array} \right. \tag{3.8}$$

where $\partial_n u$ denotes the usual normal derivative. The Steklov spectrum of a domain Ω consists of a sequence of eigenvalues of the form

$$0 = \sigma_0(\Omega) \leq \sigma_1(\Omega) \leq \sigma_2(\Omega) ... \to +\infty.$$

The zero eigenvalue is associated to a constant eigenfunction and when Ω is connected $\sigma_1(\Omega)$ is strictly positive. Therefore, the question of optimizing the Steklov eigenvalues becomes interesting for indices $k \geq 1$, corresponding to non-zero eigenvalues. When considering convexity and diameter constraints we are able to show that optimal shapes exist for the maximization of

$\sigma_k(\Omega)$. Moreover, two surprising theoretical results hold: for $k \geq 1$, the k-th Steklov eigenvalue is not maximized by the ball in any dimension and the k-th optimal Steklov eigenvalue is always multiple. The fact that analytic description of optimal shapes is not available, not even for the first eigenvalue, motivated us to investigate optimal shapes numerically. It quickly turned out that segments and angular points are present in the boundaries of optimal shapes, making the approach presented in the previous section inefficient.

We devised a simple alternative by choosing parameters

$$p_j = p(\theta_j),\ \theta_j = 2\pi j/N, j = 0, ..., N-1,$$

representing the values of the support function at a uniform discretization of $[0, 2\pi]$. In the following denote by $h = 2\pi/N$ the uniform discretization step. The convexity constraint (3.4) and the parametrization (3.3) give rise to discrete analogues once the approximation of the differential operators is chosen. A natural idea, which we employ in [A12], is to use finite differences: $p'(\theta_j) \approx \frac{p_{j+1}-p_{j-1}}{2h}, p''(\theta_j) \approx \frac{p_{j+1}+p_{j-1}-2p_j}{h^2}$. This gives rise to parametric optimization problems with linear inequality constraints, easily handled by available optimization software.

However, when investigating the convexity of the discrete polygons given by the parametrization, in the recent work [A14] I show that for h small the discrete polygon obtained is not necessary convex. A rigorous alternative is presented in the next section.

3.4.1 Rigorous discrete convexity condition

It is well known that if p is the support function of the convex body $K \subset \mathbb{R}^2$ then $\overline{p} = p + a\cos\theta + b\sin\theta$ is the support function of the translated body $(a, b) + K$. This is a straightforward consequence of definition or of the parametrization (3.3). One may note that the classical centered finite differences are not exact when considering discretizations of translations given by $\overline{p}_i = p_i + a\cos\theta_i + b\sin\theta_i$.

To remedy this we propose the following choices for approximating the first derivatives $p'(\theta_i)$ and the discrete curvature radii $p(\theta_i) + p''(\theta_i)$:

$$p'(\theta_i) \approx \frac{p_{i+1} - p_{i-1}}{2\sin h} := q_i, \quad p(\theta_i) + p''(\theta_i) \approx \varrho_i = p_i + \frac{p_{i+1} - 2p_i + p_{i+1}}{2 - 2\cos h}. \tag{3.9}$$

The observations below show that this discretization choice for first derivatives and curvature radii has multiple advantages:

- As $h \to 0$ we have $\sin h = h + O(h^3)$, $2 - 2\cos h = h^2 + O(h^4)$. Therefore, when $h \to 0$, at points where p is smooth, the discretizations proposed in (3.9) converge to $p'(\theta_i)$ and $p + p''(\theta_i)$, respectively. Therefore, the proposed discretization is **consistent**.
- Formulas (3.9) are linear in p_i and they are exact for support functions of the form $p(\theta) = c + a\sin\theta + b\cos\theta$. A first consequence is that the **discretization process commutes with translations**: the numerical representations of two translated convex bodies are related by the same translation. Secondly, translated discretized convex bodies have the same discrete curvature radii given by (3.9).
- Using $p'(\theta_i) \approx (p_{i+1} - p_{i-1})/(2\sin h)$ in (3.3) and computing the oriented area of the triangle given by three consecutive vertices $\mathbf{A}_1, \mathbf{A}_2, \mathbf{A}_3$ in the discretization, we obtain

$$\text{Area}(\Delta\mathbf{A}_1\mathbf{A}_2\mathbf{A}_3) = [\varrho_2(\varrho_1 + \varrho_3) + 2\varrho_1\varrho_3\cos h]\sin^2(h/2)\tan(h/2). \tag{3.10}$$

  Assuming the discrete radii of curvature are non-negative implies that the oriented area of $\Delta\mathbf{A}_1\mathbf{A}_2\mathbf{A}_3$ is non-negative. Therefore, **discrete shapes** constructed using (3.9) in the parametrization (3.3) **are convex**, provided

$$\varrho_i = p_i + \frac{p_{i+1} - 2p_i + p_{i+1}}{2 - 2\cos h} = \frac{p_{i+1} + p_{i-1} - 2p_i\cos h}{2 - 2\cos h} \geq 0, \quad i = 0, ..., N-1. \tag{3.11}$$

> Equation (3.10) and geometric aspects underlined in [A14, Proposition 2.7] show that for a convex n-gon, approximated using the procedure above, $N-n$ of the discrete curvature radii are equal to zero. Moreover, consecutive discrete curvature radii equal to zero correspond to overlapping points in the parametrization.

The constraints (3.11) are linear in the variables $(p_i)_{i=0}^{N-1}$ and can be easily implemented in optimization software. These constraints are used in all the numerical simulations presented in the sequel.

For $N \geq 5$, denote by $\mathcal{K}_N$ the following class of convex polygons:

$$\mathcal{K}_N = \{\mathbf{A}_0...\mathbf{A}_{N-1} : \mathbf{A}_j = p_j\mathbf{r}_j + \frac{p_{j+1}-p_{j-1}}{2\sin\frac{2\pi}{N}}\mathbf{t}_j,$$
$$p_{j+1}+p_{j-1}-2p_j\cos\frac{2\pi}{N} \geq 0,\ \forall j=0,...,N-1\}.$$

These are the polygons used in the numerical framework to approximate convex sets.

In [A14, Section 2.3] more geometric aspects are presented, motivating the choice of the discretization (3.9). It turns out that this is the only choice that produces convex polygons for all variables p_j, $0 \leq j \leq M-1$ verifying (3.11). The polygons in $\mathcal{K}_N$ defined above can approximate arbitrarily well any convex set in the Hausdorff metric as $N \to \infty$. Moreover, it can be shown that zero curvature radii in (3.9) lead to particular behavior regarding the vertices of the discrete polygon. In particular, segments in the boundary can be well characterized and multiple consecutive points may coincide at angular points.

3.4.2 Gauge function

A convex shape K with non-void interior is well characterized using a radial function $\rho : [0,2\pi] \to (0,+\infty)$ with respect to an interior point O. The radial function verifies $\rho(\theta) = |OX_\theta|$ where $X_\theta \in \partial K$ is the intersection of the line through O having direction $(\cos\theta, \sin\theta)$ with ∂K. Given a radial function $\rho(\theta)$ which is of class C^2 at least, the curvature of K for the radial coordinate θ is given by

$$\kappa(\theta) = \frac{\rho^2(\theta)+2(\rho'(\theta))^2-\rho(\theta)\rho''(\theta)}{(\rho(\theta)^2+(\rho'(\theta))^2)^{3/2}}.$$

It can be readily checked that using the gauge function, defined by $\gamma : [0,2\pi] \to (0,+\infty)$, $\gamma(\theta) = 1/\rho(\theta)$ the sign of the curvature $\kappa(\theta)$ is given by the sign of $\gamma+\gamma''$. In other words, if γ is of class C^2 then γ is the gauge function of a convex set if and only if

$$\gamma(\theta)+\gamma''(\theta) \geq 0, \text{ for every } \theta \in [0,2\pi]. \tag{3.12}$$

As recalled in the introduction, the gauge function of a convex body is the support function of the polar body $K^\circ = \{y \in \mathbb{R}^d : x \cdot y \leq 1, \forall x \in K\}$.

As in the case of the support function, described in Section 3.4.1 we consider a discretization $\theta_j = jh$, $0 \leq j \leq N-1$, with $h = 2\pi/N$. The values of the gauge function at the points θ_i are approximated by $\gamma_i \approx \gamma(\theta_i)$. Note that by definition we have $\gamma_i > 0$. The discretization of the convexity constraint (3.12) using centered finite differences gives

$$\gamma_i + \frac{\gamma_{i+1}-2\gamma_i+\gamma_{i-1}}{h^2} \geq 0, \text{ for every } 0 \leq i \leq N-1. \tag{3.13}$$

On the other hand, for three consecutive angles $\theta_{i-1}, \theta_i, \theta_{i+1}$ we may consider the triangle with vertices $\mathbf{A}_i = (1/\gamma_i)\mathbf{r}_i$, with $\mathbf{r}_i = (\cos\theta_i, \sin\theta_i)$ and computing its oriented area gives

$$\text{Area}(\Delta\mathbf{A}_{i-1}\mathbf{A}_i\mathbf{A}_{i+1}) = \frac{(\gamma_{i-1}+\gamma_{i+1}-2\gamma_i\cos h)\sin h}{2\gamma_{i-1}\gamma_i\gamma_{i+1}}. \tag{3.14}$$

This implies that the rigorous convexity condition from the discrete point of view is

$$\gamma_{i-1} + \gamma_{i+1} - 2\gamma_i \cos h \geq 0, \text{ for every } 0 \leq i \leq N-1. \tag{3.15}$$

In view of the equality $2\cos h = 2 - h^2 + O(h^4)$, inequalities (3.13) and (3.15) are equivalent up to a term of order $O(h^4)$. However, for small h (3.13) is a consequence of (3.15), but not the other way around.

It can be observed that the rigorous discrete convexity constraint (3.15) is the same as the rigorous discrete convexity constraint for the support function (3.11). Therefore, given a set of parameters $(p_i)_{i=0}^{N-1} = (\gamma_i)_{i=0}^{N-1}$, verifying the constraints (3.15), the discrete shapes constructed using the proposed discretization for the support function and the gauge functions are both convex.

3.5 Applications and Code

The numerical frameworks described in the previous sections are implemented in FreeFEM [66]. The optimization software IPOPT [116] is used for handling the various inequality constraints. The sensitivity of the objective function with respect to each one of the parameters of the discretization is computed based on the shape derivative. Details are provided in [A14, Section 3]. To facilitate the reproduction of the results of this article, some of the codes used are published online at the following repository:

`https://github.com/bbogo/ConvexSets`

The codes can be used in a straightforward way to tackle other optimization problems with the constraints described previously. It is enough to modify the computation of the objective function (based on different PDEs if needed) and to change the shape derivative formula in the code. The linear inequality/equality constraints needed for handling the convexity and width constraints should be modified accordingly.

Below I present some applications based on the previously described numerical frameworks.

(i) Using the support function. The support function allows to easily implement numerical shape optimization problems among convex sets, following the description shown in Section 3.4.1. In particular, width, constant width and diameter constraints can be imposed in a straightforward manner in this context.

- **Minimization of the k-th Dirichlet Laplace eigenvalue $\lambda_k(\omega)$ under area and convexity constraints**. For $k = 2$ best results known in the litterature, shown in [12] are obtained without any effort. For $k \geq 3$ better results than those shown in [A1] are obtained, due to the correct capturing of segments in the boundary.
- **Maximization of $\lambda_k(\omega)$ under constant width constraint**. Numerical simulations show that for $1 \leq k \leq 10$ the Reuleaux triangle is the maximizer. From a theoretical point of view this is an open problem.
- **Maximization of $\lambda_k(\omega)$ under minimal width constraint**. Numerical simulations show that for $1 \leq k \leq 10$ the equilateral triangle is the maximizer. From a theoretical point of view this is an open problem.
- Simulations made in [16] are performed using the numerical framework described above, obtaining similar results.

(ii) Using the gauge function. The numerical framework based on the gauge function described in Section 3.4.2 has the same complexity as the one based on the support function. On one hand, the parametrization using the gauge function is more straightforward, since only the radial distances are used. Recall that the support function also uses tangential components based on an approximation of the first derivative, as shown by the parametrization (3.3). However, dealing with width constraints is not straightforward in this context. Therefore, one should

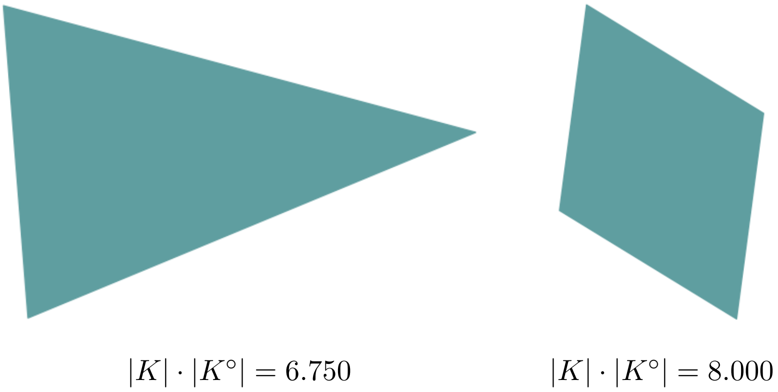

Figure 3.4: Numerical minimizers for $|K| \cdot |K^\circ|$ in dimension two.

choose between the support or gauge function parametrizations according to the particularities of the problem under study.

- The minimization of $\lambda_k(\omega)$ under convexity and volume constraints is revisited, obtaining results similar to those obtained with the support function.
- The maximization of $\lambda_1(\omega)$ under convexity, inclusion ($D_1 \subset \omega \subset D_2$) and volume constraints is investigated, following a problem proposed in the recent article [87]. Theoretical results show that free parts of $\partial\omega$ are polygonal lines, but optimal shapes are not known in general. Numerical simulations agree with the theoretical ideas and could be used to further characterize optimal shapes.

(iii) Optimizing functionals depending on a convex body and its polar body. We observed that the rigorous discrete convexity constraints for the support and the gauge functions are the same: see (3.11) and (3.15). Moreover, the gauge function of a convex set is the support function of the polar body. As a direct consequence, one can use the same set of parameters to describe K and its polar body K°.

As an illustration, we test the algorithm for a well known problem in dimension two, the minimization of the product $|K| \cdot |K^\circ|$. It is well known that when K is convex and symmetric with respect to the origin, the solution is a parallelogram, while when K is a general shape containing the origin, the solution is a triangle. More details about this problem can be found in [31]. The numerical simulations recover the theoretical ones as shown in Figure 3.4. While in dimension two the problem is solved, the three dimensional case is not yet solved completely. The conjecture is proved for $n = 3$ for centrally symmetric bodies in [73]. An extension of the numerical framework to the three dimensional case is of particular interest in this sense.

3.6 Perspectives

The framework described in Section 3.4 is complete in dimension two, in the sense that arbitrary functionals can be handled and the discrete shapes used are always convex, provided the parameters verify the corresponding linear inequality constraints. The next goal is to extend this framework in dimension three. The potential difficulties are underlined below:

- Compared to dimension two, in dimension three a uniform sampling of the unit three dimensional sphere should be used. Such a uniform sampling is not exact, but numerical algorithms can be used.
- Given a uniform sampling of the sphere and a set of parameters representing the support function at these points, approximations of the tangential gradients are needed to define the boundary points. Like in dimension two, one key point could be to impose that the discretization is invariant with respect to translations.

- The geometric aspects shown in [A14, Section 2] should be extended to the three dimensional case, giving additional insight on the rigorous discrete convexity constraint in this case.
- The usage of the gauge function in dimension three should be investigated. One could, potentially, recover the two dimensional results, namely that for a set of parameters, the discrete convexity constraints should be the same for the gauge and support functions.

Achieving this program would lead to a complete numerical framework in dimensions two and three, allowing the study of a large class of functionals under the convex geometry constraints presented in this chapter.

Chapter 4

Optimal partitioning and multiphase problems

4.1 Introduction

This chapter presents theoretical and numerical aspects related to shape optimization problems depending on multiple shapes. Consider a domain D subset of an Euclidean space or a manifold and a fixed positive integer $n \geq 2$. General problems of the form

$$\min_{(\omega_i)\in\mathcal{A}} F(\omega_1,...,\omega_n)$$

are considered where $\mathcal{A}$ denotes the set of partitions of D, defined by

$$\mathcal{A} = \{(\omega_i)_{i=1}^n : \operatorname{int}(\omega_i) \cap \operatorname{int}(\omega_j) = \emptyset \text{ for } 1 \leq i < j \leq n, \bigcup_{i=1}^n \overline{\omega}_i = D\}, \tag{4.1}$$

where the usual notations for the interior and closure of a set are used. Given $(\omega_i)_{i=1}^n \in \mathcal{A}$, we call ω_i a *phase* or *cell* of the partition. General multiphase problems where the partition condition is removed, considering only n non-overlapping phases, can also be investigated using the tools proposed in the sequel. In some cases, additional volume constraints $|\omega_i| = c_i$ are imposed for each one of the cells ω_i, $1 \leq i \leq n$.

Famous examples in this sense are given by the minimization of the total perimeter

$$\min_{(\omega_i)\in\mathcal{A}} \sum_{i=1}^n \operatorname{Per}(\omega_i) \tag{4.2}$$

when the areas of ω_i are equal: $|\omega_i| = |D|/n$. Theoretical and quantitative results are well studied for problem (4.2) as shown, for example, in [93] and [98]. Nevertheless, explicit optimal configurations are rarely known, as in addition to the usual difficulties when dealing with shape optimization problems for one phase, combinatorial aspects concerning the position of the cells need to be taken into account. The asymptotic case where $n \to \infty$ is known as the *honeycomb conjecture*. Since the antiquity it was remarked that the structure of the bee honeycomb should be optimal in terms of labor cost. Since this cost is related to the total perimeter of the honeycomb walls, it was natural to conjecture that the hexagonal partition is optimal for (4.2) as $n \to \infty$. This result was proved in full generality only recently in the famous work of T. Hales [65]. Numerical algorithms for approximating solutions to problem (4.2) were proposed in various contexts. The three dimensional case is more challenging and the corresponding optimal partition is not known. The Weaire-Phelan structure [120] is conjectured to be optimal, following various numerical results. In [45] the authors use the software Evolver by K. Brakke which can optimize locally the total perimeter starting from a given partition. One difficulty in the study presented in [45] is that all combinatorial combinations of cell configurations need to be considered as initializations to avoid local minima. An alternative approach based on the Voronoi implicit interface method is described in [111], where the cells of the partition are modeled with a function inspired from the level-set method.

A more flexible approach, less sensible to the initialization and being able to deal with arbitrary cell configurations (without any restrictions related to connectedness or combinatorial aspects) was proposed in [103]. In this approach, cells are replaced with densities, the perimeter is approximated using the Modica-Mortola Γ-convergence result and the partition condition becomes a simple algebraic constraint: the sum of the densities is identically equal to 1. An analogue approach for minimal perimeter partitions on manifolds is presented in [A23]. This allowed us to recover results from [45] regarding optimal partitions of the sphere into equal area cells, avoiding all the difficulties regarding the combinatorial configuration of the cells in the intialization. In [34] the method was extended to a large number of cells by considering a restricted grid around each cell, drastically reducing the computational costs. This work inspired the framework presented in Section 4.4 for the case of spectral functionals.

Recently, in [A3] we investigate how the minimal relative perimeter partition of D into n cells varies with respect to the shape of the container D. This study was motivated by [55] where the authors solve the two dimensional case where $n = 2$ and D is divided into equal areas: it is shown that the disk maximizes the minimal perimeter partition into two cells of equal areas. We show that, among convex sets, there exists a container D maximizing the minimal total relative perimeter of a partition with fixed volume of the cells (not necessarily equal). Then we devise a numerical method for approximating maximizing shapes. Surprisingly, the ball seems to be optimal in 2D and 3D, regardless on the volume constraints assigned to the cells. The details of this work are described in Section 4.2.

Given a domain $D \subset \mathbb{R}^d$, the α-Cheeger set is defined as the subset $\omega \subset D$ minimizing the ratio $\dfrac{\operatorname{Per}(\omega)}{|\omega|^\alpha}$. Inspired from the Modica-Mortola theorem, in [A17] we present a Γ-convergence approximation for the α-Cheeger sets and the corresponding problem for clusters. When α converges to $(d-1)/d$, it is possible to approximate circle and ball packing problems using a direct variational method, avoiding the usual combinatorial difficulties. This work is presented in Section 4.3. In this context, instead of considering a partitioning problem we work directly with the Cheeger sets in a multiphase formulation.

A second class of partitioning problems that I studied is related to the minimization of functionals related to the Dirichlet-Laplace eigenvalues for each one of the cells. A classical problem is to solve

$$\min_{(\omega_i)\in\mathcal{A}} \lambda_1(\omega_1) + ... + \lambda_1(\omega_n), \tag{4.3}$$

where $\mathcal{A}$ denotes the family of partitions of a given domain D defined in (4.1). Notice that no constraint is imposed on the volumes of the cells in this case, since the monotonicity and properties of the eigenvalues show that a small cell will have a large first eigenvalue. From a quantitative point of view, an optimal configuration will have connected cells with a volumes that are not too small. The problem was studied in [43], [42] from a theoretical point of view. However, earlier references and computations can be found in [47], where (4.3) is related to the stationary state of some chemical reaction system. The study of this problem is also motivated by modelization considerations when studying dynamical systems of populations in competition [44]. Removing the partition condition and adding a volume penalization term for each cell leads to a well posed multiphase problem studied theoretically in [39] and numerically in [A19]. The existence of solutions for problem (4.3) is discussed in [32]. Although various conjectures exist for particular domains D, almost no theoretical result is known regarding the precise description of minimizers, not even for $n = 2$. This motivated the study of numerical methods like the one proposed in [32] where again densities are used to parametrize shapes. From a theoretical point of view it is conjectured that when $n \to \infty$ the honeycomb hexagonal partition is optimal for

(4.3). The conjecture was motivated by simulations presented in [32] and more recently by those in [A16]. Theoretical results in [37] show that, assuming convexity of the cells, the honeycomb conjecture is optimal, provided the Polyà-Szegö conjecture[1] holds true for pentagons, hexagons and heptagons. The most recent developments related to this famous conjecture are presented in Chapter 5.

Different functions depending on the fundamental eigenvalues of the cells can be considered, among which we mention p-norms and the maximum. The maximum of the fundamental eigenvalues is of particular interest, since in some cases, the optimal partition is related to the nodal partition of a particular eigenfunction of D. This is one of the rare cases where the solution to the corresponding optimal partitioning problem can be identified analytically. Among the various articles dealing with this aspect I mention [28], [27], [29], [26], [25]. In the paper [A15] written in collaboration with V. Bonnaillie-Noël, we propose an algorithm inspired from [32] for minimizing p-norms of the fundamental eigenvalues. For $p \to \infty$, such optimal partitions approximate the optimal partition for the maximum of the fundamental eigenvalues. We investigate for various planar domains the evolution of such partitions as p changes.

The numerical algorithm used in [A15] uses a grid restriction technique, using only neighboring nodes of the current cell in the computation of the Dirichlet-Laplace eigenvalue. This brings significant efficiency improvements compared to the algorithm proposed in [32]. The algorithm is further improved and extended to optimal partitions on surfaces and in dimension three in [A16]. Further aspects related to optimal partitioning for functionals depending on spectral quantities are presented in Section 4.4

4.2 Total relative perimeter: behavior of the optimal partition on moving domains

Given $\Omega \subset \mathbb{R}^d$, open, connected with Lipschitz boundary and $c \in (0,1)$ we consider the *isoperimetric profile*

$$I(\Omega,c) = \min\{\operatorname{Per}_\Omega(\omega) : \omega \subset \Omega, |\omega| = c|\Omega|\}. \tag{4.4}$$

We denote by $\operatorname{Per}_\Omega$ the relative perimeter with respect to Ω. For a regular set $\omega \subset \Omega$ we have $\operatorname{Per}_\Omega = \mathcal{H}^{d-1}(\partial\omega \cap \Omega)$, i.e. only the perimeter of ω inside Ω is taken into account. As usual, $\mathcal{H}^{d-1}$ denotes the $d-1$ dimensional Hausdorff measure. The notion of perimeter can be generalized to less regular sets, called generically *sets of finite perimeter*, using functions of bounded variation. More precisely $\omega \subset \Omega$ has finite relative perimeter with respect to Ω if its characteristic function χ_ω belongs to $BV(\Omega)$, the space of functions defined on Ω, having bounded variation. More details can be found, for example, in [93, Part II].

Similarly, given $\mathbf{c} = (c_i)_{i=1}^n \in \mathbb{R}^n$ such that $\sum_{i=1}^n c_i = 1$ consider the *isoperimetric profile of a partition* defined by

$$PI(\Omega,\mathbf{c}) = \min\{\sum_{i=1}^n \operatorname{Per}_\Omega(\omega_i) : \omega_i \subset \Omega, (\omega_i) \text{ form a partition of } \Omega, |\omega_i| = c_i|\Omega|\}. \tag{4.5}$$

The existence of optimal isoperimetric sets and partitions is classical [98], [93] and is a consequence of the lower semicontinuity of the generalized de Giorgi perimeter with respect to the L^1 convergence of characteristic sets.

We are interested in optimizing the isoperimetric profiles defined above with respect to the shape of the container Ω, when the volume is fixed. Considering thin rectangles shows that the minimization problem does not have a solution. Therefore, we turn our attention to the maximization problems. In the case of a single phase, given $c \in (0,1)$ consider the problem

$$\max_{|\Omega| = v_d} I(\Omega,c). \tag{4.6}$$

---

[1] The conjecture says that regular n-gons minimize λ_1 among n-gons having fixed area.

For the partition case, given $\mathbf{c} \in \mathbb{R}^d$ with $\sum_{i=1}^n c_i = 1$ consider the problem

$$\max_{|\Omega|=v_d} PI(\Omega, \mathbf{c}). \tag{4.7}$$

Our work was initiated by the article [80] on the CNRS Image des Mathématiques website, where the contents of [55] are discussed. The article asks what happens if isoperimetric sets corresponding to volumes smaller than one half are considered. It turns out that the single phase problem is called *convex isoperimetric problem* in the literature and dates back to an article of [121] according to historical facts presented on Frank Morgan's blog [99]. The single phase problem is solved for $c = 1/2$ in [55] and for small $c \in (0, 1)$ in [22]. The case of perturbations of the disk and axisymetric domains is handled in [117]. The question of maximizing the isoperimetric profile of a partition (4.5) is new.

We start by proving that problems (4.6) and (4.7) have solutions. We consider the case of convex sets, although in dimension two the result could hold even among star-shaped domains or even simply connected domains, since we did not find any relevant counterexamples. The proof of existence given in [A3, Section 2] has the following steps:

- **Upper bounds** for the isoperimetric profiles are found using a Loomis-Withney inequality [81] which relates the volume of a convex body K to the volume of its projection on a family of hyperplanes orthogonal to an orthonormal basis of $\mathbb{R}^d$. This shows that the minimal volume of the projection of Ω on a hyperplane has an upper bound in terms of $|\Omega|$.
- **Compactness** properties for a maximizing sequence are recovered by finding an upper bound for the diameter and using the Blaschke selection theorem [112, Chapter 1].
- Finally, **continuity** of the isoperimetric profiles for the Hausdorff metric is a consequence of the results in [108], which are extended to the case of partitions.

Numerical tools that help approximate isoperimetric sets and minimal length partitions based on Γ-convergence results are developed in [103], [A23]. In our work we want to maximize the length of a minimal perimeter partition with respect to the shape of the container Ω.

A key point in our approach is the approximation of minimal length partitions involved in the computation of $PI(\Omega, \mathbf{c})$. In order to avoid difficulties related to the treatment of the partition constraint it is convenient to represent each set in the partition ω_i as a density $u_i : \Omega \to [0, 1]$. Then, the partition constraint can be simply expressed by the algebraic equality $\sum_{i=1}^n u_i = 1$ on Ω. The next aspect is the approximation of the perimeter of a set represented via its density function. A well known technique is based on the Γ-convergence relaxation for the perimeter inspired by a result of Modica and Mortola [97]. The main idea is to replace the perimeter with a functional that, when minimized, yields minimizers converging to those that minimize the perimeter.

Let us briefly recall the concept of Γ-convergence and the property that motivates its use when dealing with numerical optimization. Let X be a metric space. For $\varepsilon > 0$ consider the functionals $F_\varepsilon, F : X \to [0, +\infty]$. We say that F_ε Γ-converges to F and we denote $F_\varepsilon \xrightarrow{\Gamma} F$ if the following two properties hold:

(LI) For every $x \in X$ and every $(x_\varepsilon) \subset X$ with $(x_\varepsilon) \to x$ we have

$$F(x) \leq \liminf_{\varepsilon \to 0} F_\varepsilon(x_\varepsilon) \tag{4.8}$$

(LS) For every $x \in X$ there exists $(x_\varepsilon) \subset X$ such that $(x_\varepsilon) \to x$ and

$$F(x) \geq \limsup_{\varepsilon \to 0} F_\varepsilon(x_\varepsilon). \tag{4.9}$$

An important consequence is the following classical result concerning the convergence of minimizers of a sequence of functionals that Γ converge:

Suppose that $F_\varepsilon \xrightarrow{\Gamma} F$ *and* x_ε *minimizes* F_ε *on* X*. Then every limit point of* (x_ε) *is a minimizer for* F *on* X*.*

Therefore, in practice, in order to approximate the minimizers of F it is possible to search for minimizers of F_ε, for ε small enough.

Let us now state the two theoretical results that are used in this work concerning the Γ-convergence relaxation of the perimeter and of the total perimeter of a partition, with integral constraints on the densities. The first result is the classical Modica-Mortola theorem [97]. Various proofs can be found in [1, 33, 41]. In the following Ω is a bounded, Lipschitz open set. Consider a double well potential $W : \mathbb{R} \to [0,\infty)$ which verifies the following assumptions: W is of class C^1, $W(z) = 0$ if and only if $z \in \{0,1\}$ and W has exactly three critical points. For such a double well potential W described previously, denote $\gamma = 2\int_0^1 \sqrt{W(s)}ds$. In the following $c \in [0,1]$ represents the fraction used for the volume constraint.

Theorem 4.2.1 (Modica-Mortola)**.** *Define* $F_\varepsilon, F : L^1(\Omega) \to [0,+\infty]$ *by*

$$F_\varepsilon(u) = \begin{cases} \displaystyle\int_\Omega \left(\varepsilon|\nabla u|^2 + \frac{1}{\varepsilon}W(u)\right) & u \in H^1(\Omega), \int_\Omega u = c|\Omega| \\ +\infty & \textit{otherwise} \end{cases}$$

and

$$F(u) = \begin{cases} \gamma \operatorname{Per}_\Omega(\{u=1\}) & u \in BV(\Omega;\{0,1\}), \int_\Omega u = c|\Omega| \\ +\infty & \textit{otherwise} \end{cases}.$$

Then $F_\varepsilon \xrightarrow{\Gamma} F$ *in the* $L^1(\Omega)$ *topology.*

This result can be generalized to the case of partitions. It should be underlined that it is not a trivial extension of the single phase result, since the **Γ-convergence is not stable for the sum**.

Theorem 4.2.2. *Define* $G_\varepsilon, G : L^1(\Omega) \to [0,+\infty]$ *by*

$$G_\varepsilon(\mathbf{u}) = \begin{cases} \displaystyle\sum_{i=1}^n \int_\Omega \left(\varepsilon|\nabla u_i|^2 + \frac{1}{\varepsilon}W(u_i)\right) & \textit{if } \mathbf{u} \in (H^1(\Omega))^n \cap X(\Omega,\mathbf{c}) \\ +\infty & \textit{otherwise} \end{cases}$$

$$G(\mathbf{u}) = \begin{cases} \gamma \sum_{i=1}^n \operatorname{Per}_\Omega(\{u_i=1\}) & \textit{if } \mathbf{u} \in (BV(\Omega,\{0,1\}))^n \cap X(\Omega,\mathbf{c}) \\ +\infty & \textit{otherwise} \end{cases}$$

Then $G_\varepsilon \xrightarrow{\Gamma} G$ *in the* $(L^1(\Omega))^n$ *topology.*

A proof of this result can be found in [103]. In the numerical simulations the double well potential is $W(s) = s^2(1-s)^2$ which gives the factor $\gamma = 1/3$ in the results shown above.

4.2.1 Numerical framework for approximating minimal perimeter partitions

In this section the numerical minimization of F_ε and G_ε is discussed. Since Ω is a general domain, we choose to work with finite element discretizations. Given $\mathcal{T}_h$ a triangulation of Ω, denote by $(x_j)_{j=1}^N$ the set of the nodes. Working with $\mathbf{P_1}$ Lagrange finite elements, a piecewise affine function u defined on the mesh $\mathcal{T}_h$ is written $\sum_{j=1}^N u_j\phi_j$. As usual, ϕ_j are the piece-wise linear functions on each triangle, characterized by $\phi_j(x_k) = \delta_{jk}$. For a $\mathbf{P_1}$ finite element function, the values u_j are given by $u(x_j)$ and we denote $\mathbf{u} = (u_j) = (u(x_j)) \in \mathbb{R}^N$. With these notations, it is classical to introduce the mass matrix M and the rigidity matrix K defined by

$$M = \left(\int_{\mathcal{T}_h} \phi_i\phi_j\right)_{1\le i,j\le N} \text{ and } K = \left(\int_{\mathcal{T}_h} \nabla\phi_i \cdot \nabla\phi_j\right)_{1\le i,j\le N}$$

As an immediate consequence of the linearity of the decompositions $u = \sum_{j=1}^N u_j\phi_j$, $v = \sum_{j=1}^N v_j\phi_j$ we have that

$$\int_{\mathcal{T}_h} uv = \mathbf{u}^T M\mathbf{v} \text{ and } \int_{\mathcal{T}_h} \nabla u\cdot\nabla v = \mathbf{u}^T K\mathbf{v}.$$

This immediately shows that the functionals F_ε and G_ε can be approximated using the mass and rigidity matrices M and K using the expression

$$\int_{\mathcal{T}_h} \left(\varepsilon|\nabla u|^2 + \frac{1}{\varepsilon}u^2(1-u)^2\right) \approx \varepsilon\mathbf{u}^T K\mathbf{u} + \frac{1}{\varepsilon}\mathbf{v}^T M\mathbf{v} =: \mathcal{F}(\mathbf{u}) \tag{4.10}$$

where $\mathbf{v} = (u_j(1-u_j))_{j=1}^N$. The formula (4.10) is a quadrature rule using values at the nodes of the triangulation. The first term is exact for $\mathbf{P_1}$ functions u. The second term in the integral (4.10), is a fourth order polynomial, which is approximated using the mass matrix for $\mathbf{P_1}$ finite elements. The approximation error appears only in regions where $\mathbf{u} \in (0,1)$, corresponding to the phase transition region. The gradient of this expression w.r.t. $\mathbf{u}$ can be computed and is given by

$$\nabla\mathcal{F}(\mathbf{u}) = 2\varepsilon K\mathbf{u} + \frac{2}{\varepsilon}M\mathbf{v}\odot(1-2\mathbf{u}), \tag{4.11}$$

where $\odot$ denotes pointwise multiplication of two vectors: $\mathbf{u}\odot\mathbf{v} = (u_jv_j)_{j=1}^N$.

It is obvious that with (4.10) and (4.11) it is possible to implement a gradient-based optimization algorithm in order to minimize F_ε and G_ε. The software FreeFEM [66] is used for constructing the finite element framework and the algorithm LBFGS from the package Nlopt [75] is used for the minimization of (4.10).

Constraints. Volume and partition constraints need to be imposed for all the phases represented by the densities $(u_i)_{i=1}^n$. A projection method is considered, allowing the use of efficient optimization algorithms recalled above. The details are given in [A3, Section 3.2]. The main idea inspired from [34] is to project u_i parallel to $\sqrt{2W(u_i)}$, modifying the densities mostly at the interface with the neighboring cells.

Initialization. It was underlined that density based methods from [103], [A23] allow to obtain meaningful approximation of global minimizers starting from random densities. Nevertheless, in our case, an optimal partition needs to be found at every iteration of the maximization algorithm. It is therefore useful to search for initializations that are as close as possible to the optimal partition we search. This lead us to consider Voronoi diagrams with particular features, as described in [A3, Section 3.3].

We compute the sensitivity of the areas and perimeters of each one of the Voronoi cells with respect to the position of the Voronoi points. This allows us to find:

- Voronoi diagrams with cells having prescribed areas.
- Perimeter minimizing Voronoi diagrams with area constraints for the cells.

These tools are used for finding initial partitions in dimension two. In dimension three, this process is more costly and only random Voronoi diagrams were considered.

Shape derivative. Assuming that minimizers u_Ω and $(u_\Omega^i)_{i=1}^n$ of F_ε and G_ε, respectively, defined in Theorems 4.2.1, 4.2.2 are unique and differentiable with respect to Ω we find that the ε-isoperimetric profiles are shape differentiable verifying:

$$I_\varepsilon(\Omega,c)'_\Omega(\theta) = \int_{\partial\Omega}\left(\varepsilon|\nabla u_\Omega|^2 + \frac{1}{\varepsilon}W(u_\Omega) + \mu(u_\Omega - c)\right)\theta\cdot n \tag{4.12}$$

where $\mu = -\frac{1}{\varepsilon|\Omega|}\int_\Omega W'(u_\Omega)$ and

$$\begin{aligned} PI_\varepsilon(\Omega,\mathbf{c})'_\Omega(\theta) = & \int_{\partial\Omega}\sum_{i=1}^n \left(\varepsilon|\nabla u^i_\Omega|^2 + \frac{1}{\varepsilon}W(u^i_\Omega)\right)\theta\cdot n \\ & + \sum_{i=1}^n \mu_i \int_{\partial\Omega}(u^i_\Omega - c_i)\theta\cdot n \end{aligned} \tag{4.13}$$

The Lagrange multipliers μ_i can be found using $\phi_i = \delta_{ij}$ in the optimality conditions for the minimization of G_ε, which gives $\mu_i = -1/(\varepsilon|\Omega|)\int_\Omega W'(u^i_\Omega)$. Details regarding these computations are given in [A3, Section 3.4].

It should be noted that results obtained agree with classical works related to the differentiation of a minimum under constraints: [52, Chapter 9, Sections 2.3, 5.4], [59, Capter 3], [30, Chapter 4]. Looking more closely at formulas (4.12), (4.13) it can be observed that the terms appearing can be associated to one of the two phenomena:

- Movement of the boundary at the contact point between $\partial\Omega$ and the interfaces of the optimal partition.
- Global movement of the boundary corresponding to the intersection with the cell with index i, proportional with the corresponding Lagrange multiplier μ_i. In the single phase case, the Lagrange multiplier is related to the mean curvature of the isoperimetric set, according to [92].

Parametrization and optimization algorithm. We are interested in studying numerically problems (4.6) and (4.7) among convex sets. We choose to work with radial parametrization, which obviously includes convex sets. The radial functions are parametrized using truncated Fourier series.

The maximization algorithm used is a simple gradient flow, advancing in the direction of the gradient regardless of the evolution of the value of the objective function. The step of the gradient flow algorithm is decreased after a fixed number of iterations to avoid oscillations and to improve convergence. This algorithm choice is motivated by the fact that we compute the objective function via a numerical optimization algorithm. If instead of a global minimum we use a local minimum for computing an ascent direction and the objective value, we may find a larger value than expected for the maximum. A gradient flow algorithm may correct itself at subsequent iterations, if needed.

Code. The finite element software used for the optimization algorithm described in Section 4.2.1 is FreeFEM [66], which provides an interface to the LBFGS optimizer from Nlopt [75].

The partition initialization via Voronoi diagrams is coded in Python, where optimization algorithms from `Scipy.optimize` and `Nlopt` are used for unconstrained and, respectively, constrained optimizations. Codes and examples are provided in the following Github repository:

`https://github.com/bbogo/LongestShortestPartitions/tree/main/GradientVoronoi`.

The visualization is done with Python using Matplotlib in dimension two and Mayavi [107] in dimension three. The graphical representation of partitions is done by extracting surface meshes of an iso-level for each cell in the optimal partition using FreeFEM [66] and MMG3D [48]. These surface meshes are then plotted with Mayavi [107]. Some codes used for obtaining the results illustrated in the paper can be found in the Github repository:

`https://github.com/bbogo/LongestShortestPartitions/tree/main/FreeFEMcodes`.

4.2.2 Numerical results and discussion

The behavior of the gradient flow algorithm is illustrated in Figures 4.1 and 4.2. It can be observed that the objective function stabilizes itself as the step decreases. The optimal numerical

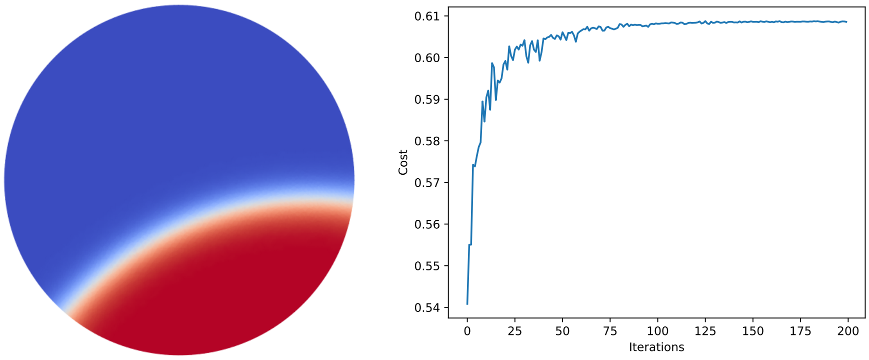

Figure 4.1: Maximization of $I(\Omega, 0.3)$ in dimension two together with the evolution of the cost function.

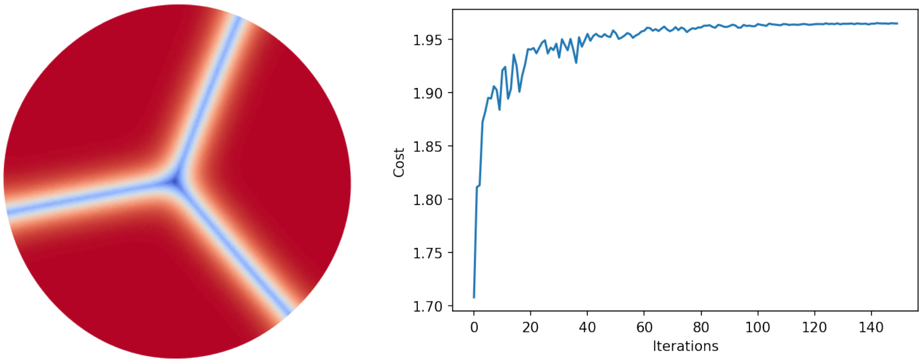

Figure 4.2: Maximization of $PI(\Omega, (1/3, 1/3, 1/3))$ in dimension two together with the evolution of the cost function.

shape obtained is the disk, regardless of the number of cells, as also shown in Figures 4.3, 4.4. Three dimensional computations shown in Figures 4.5, 4.6 show that the ball is the numerical maximizer. It is remarkable that the ball remains the maximizer even when the volume constraints on the cells are not equal.

The theoretical considerations and numerical simulations presented in this work suggest that the results of [22], [117], [55] are valid in more general settings: in dimensions two and three, under volume and convexity constraints the ball maximizes the following:

- the minimal relative perimeter of a subset $\omega \subset \Omega$ with volume constraint $|\omega| = c|\Omega|$ for all $c \in (0, 1)$.
- the minimal relative perimeter of a partition of Ω into sets $(\omega_i)_{i=1}^n$ with volume constraints $|\omega_i| = c_i|\Omega|$ given $c_i \in (0, 1)$ with $\sum_{i=1}^n c_i = 1$. The result seems to hold even in the case where the sets $|\omega_i|$ do not have the same volume constraints.

In [A3, Section 5] we also investigate the optimality conditions based on the shape derivative formulas. We conclude that the optimal partition corresponding to a solution of (4.6) or (4.7)

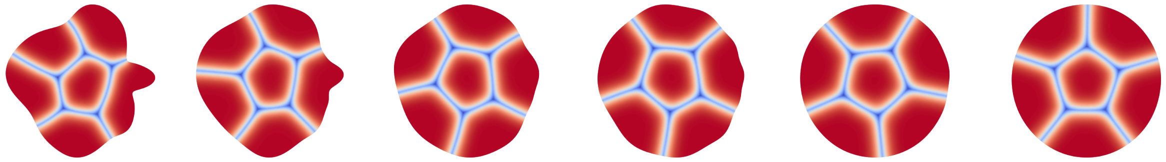
Iter 1: 3.305 Iter 6: 3.383 Iter 13: 3.384 Iter 20: 3.422 Iter 70: 3.441 Iter 150: 3.450

Figure 4.3: Illustration of the gradient flow algorithm in dimension two for $n = 6$: the numerical optimal partition and its associated cost are represented for a couple of iterations.

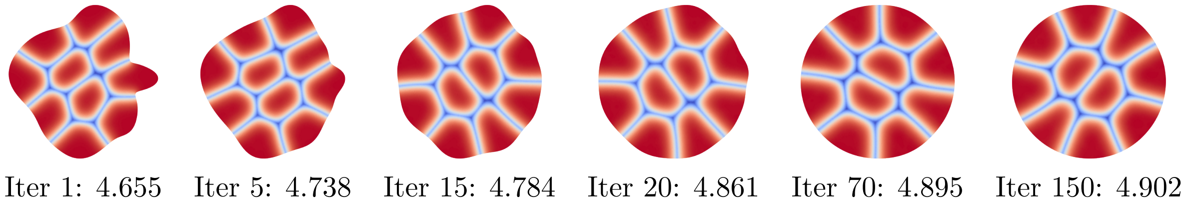

Figure 4.4: Illustration of the gradient flow algorithm in dimension two for $n = 10$: the numerical optimal partition and its associated cost are represented for a couple of iterations.

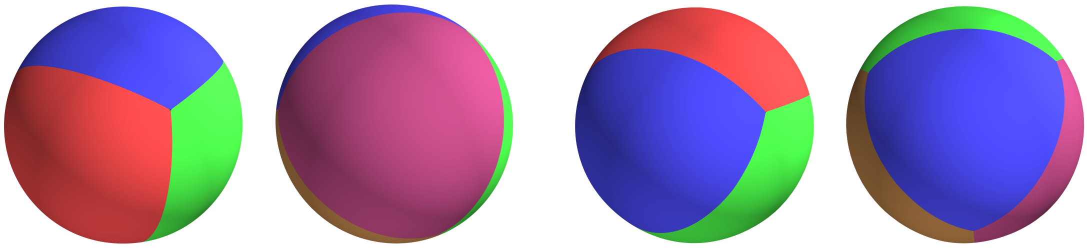

Figure 4.5: (left) Maximization of the length of the minimal perimeter partition into equal areas for $n \in \{3, 4\}$. (right) Results obtained when the area constraints are not the same: $n = 3$: ratios $1 : 2 : 2$, $n = 4$: ratios $1 : 2 : 2 : 2$.

is not unique. Moreover, it is likely that every boundary point of a maximizing set Ω should be a contact point for an optimal isoperimetric set or partition. This fact shows why the ball is likely to be a solution for the problems considered, regardless of the size of the constraints.

4.3 Cheeger sets and clusters

Consider $d \geq 2$ and $\alpha > \frac{d-1}{d}$ a fixed constant. For every bounded measurable subset E of $\mathbb{R}^d$, we introduce the following generalized α-Cheeger constant

$$h_\alpha(E) := \min \left\{ \frac{\mathcal{H}^{N-1}(\partial^* \Omega)}{|\Omega|^\alpha} \ : \ \Omega \subset E, \ \Omega \text{ measurable} \right\}. \tag{4.14}$$

Notice that the lower bound on the exponent α is linked to the isoperimetric inequality. The case $\alpha = 1$ corresponds to the classical notion of Cheeger set. Given a container $D \subset \mathbb{R}^d$, the objective of the work [A17] is to study problems

$$\min \left\{ \max_{i=1,\dots,k} h_\alpha(E_i) : \ (E_1, \dots, E_k) \in \mathcal{P}_k(D) \right\} \tag{4.15}$$

$$\min \left\{ \sum_{i=1}^k h_\alpha(E_i) : \ (E_1, \dots, E_k) \in \mathcal{P}_k(D) \right\}, \tag{4.16}$$

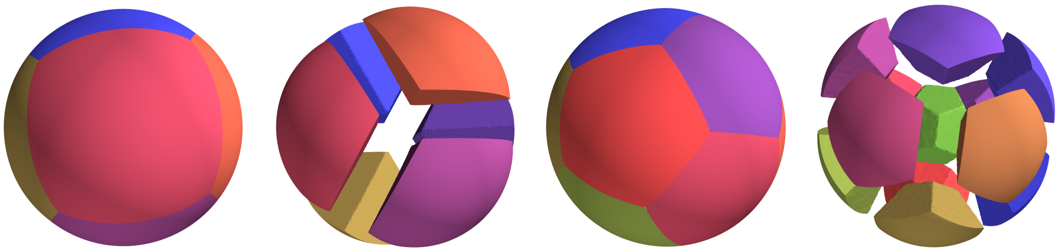

Figure 4.6: Maximization of the length of the minimal perimeter partition into equal areas for $n \in \{6, 13\}$. An expanded view of the optimal partition is also illustrated for each case.

where D is a given open bounded subset of $\mathbb{R}^d$ and

$$\mathcal{P}_k(D) = \Big\{(E_1,\dots,E_k)\ :\ \forall i,j=1,\dots,k,\ E_i\subset D,\ E_i\cap E_j=\emptyset,\ E_i \text{ measurable}\Big\}$$

denotes the set of partitions of D. The objective is twofold:

- Obtain qualitative results describing the behavior of the α-Cheeger clusters when $\alpha \to \left(\frac{d-1}{d}\right)_+$ or $\alpha\to+\infty$.
- Give an efficient phase field numerical approach for computing optimal α-cheeger clusters and, as a consequence of their asymptotic behavior, of optimal packings of balls in arbitrary boxes D.

A first natural idea is to observe that instead of working with the sets E_i one can work directly with the associated α-Cheeger sets ω_i, transforming the optimal partition problem into a multiphase problem.

Theoretical results. Let us recall briefly the main theoretical results proved in [A17]. Concerning the limiting behavior of solutions with respect to α we have the following:

- when $\alpha \to \left(\frac{d-1}{d}\right)_+$ solutions to problem (4.15) converge to the optimal packing problem

  $$\max\Big\{r\ :\ \exists\{x_i, r_i\geq r\}_{i=1,\dots,k}\,,\ B(x_i,r_i)\subset D\,,\ B(x_i,r_i)\cap B(x_j,r_j)=\emptyset\Big\}, \tag{4.17}$$

  and solutions to problem (4.16) converge to the following optimal packing problem

  $$\max\Big\{\prod_{i=1}^k r_i\ :\ \exists\{x_i,r_i\}_{i=1,\dots,k}\,,\ B(x_i,r_i)\subset D\,,\ B(x_i,r_i)\cap B(x_j,r_j)=\emptyset\Big\}.$$

- when $\alpha\to+\infty$ a solution to problem (4.15) converges the partition of D into k cells having equal measure, minimizing the product of their perimeters. We conjecture that for large k, similar to the result of [65], this optimal partition is the hexagonal one.

Next, we consider an approximation by Γ-convergence of the p-norm of a Cheeger cluster. Motivated by the Modica-Mortola result [97] (see also Theorem 4.2.1) and the definition of the α-Cheeger set, we consider an energy containing the Modica-Mortola formula at the numerator and a volume term in the denominator. The key point is to consider a higher exponent for the density in the volume integral in the denominator, as the natural choice equal to one is not enough.

Theorem 4.3.1. *Let D be a bounded, open and Lipschitz domain in $\mathbb{R}^d$. For any fixed $\alpha > \frac{d-1}{d}$ and $p>1$, consider the sequence of functionals defined on $L^1(D,\mathbb{R}^k)$ by*

$$F_{p,\varepsilon}(u_1,\dots,u_k) := \sum_{i=1}^k\left(\frac{\varepsilon\int_D|\nabla u_i|^2dx+\frac{9}{\varepsilon}\int_D u_i^2(1-u_i)^2}{\left(\int_D|u_i|^{\frac{2d}{d-1}}dx\right)^\alpha}\right)^p$$

if $u_i\in H^1_0(D)$, $u_i\geq 0$, $\sum_{i=1}^k u_i\leq 1$, and $+\infty$ if not. Then, for every sequence $u_i^\varepsilon\in H^1_0(D)\setminus\{0\}$ such that $\limsup_{\varepsilon\to 0}F_\varepsilon(u_1^\varepsilon,\dots,u_k^\varepsilon)<+\infty$, $(u_1^\varepsilon,\dots,u_k^\varepsilon)$ converges up to subsequences to some limit $(u_1,\dots,u_k)$ in $L^1(D,\mathbb{R}^k)$. Moreover, the sequence $F_{p,\varepsilon}$ Γ-converges as $\varepsilon\to 0$ in $L^1(D,\mathbb{R}^k)$ to the functional

$$F_p(\Omega_1,\dots,\Omega_k) := \sum_{i=1}^k\left(\frac{\mathcal{H}^{d-1}(\partial^*\Omega_i)}{|\Omega_i|^\alpha}\right)^p. \tag{4.18}$$

In practice, we replace the non-overlapping condition $\sum_{i=1}^k u_i\leq 1$ with a penalty term $\frac{1}{\varepsilon}\sum_{1\leq i<j\leq k}u_i^2u_j^2$ inspired from the paper of Caffarelli and Lin [43]. This gives rise to the following result which is the main practical tool for the numerical implementation of our phase field approach.

Proposition 4.3.2. *Let D be a bounded, open and Lipschitz domain in $\mathbb{R}^d$. For any fixed $\alpha > \frac{d-1}{d}$ and $p > 1$, the sequence of functionals defined on $L^1(D, \mathbb{R}^k)$ by*

$$\widetilde{F}_{p,\varepsilon}(u_1, \dots, u_k) := \sum_{i=1}^{k} \Big(\frac{\varepsilon \int_D |\nabla u_i|^2 dx + \frac{9}{\varepsilon} \int_D u_i^2 (1-u_i)^2}{\Big(\int_D |u_i|^{\frac{2d}{d-1}} dx \Big)^{\alpha}} \Big)^p + \frac{1}{\varepsilon} \sum_{1 \le i < j \le k} \int_D u_i^2 u_j^2 dx \tag{4.19}$$

if $u_i \in H_0^1(D)$, $0 \le u_i \le 1$ and $+\infty$ if not, Γ-converges as $\varepsilon \to 0$ in $L^1(D, \mathbb{R}^N)$ to the functional

$$F_p(\Omega_1, \dots, \Omega_k) := \sum_{i=1}^{k} \Big(\frac{\mathcal{H}^{d-1}(\partial^* \Omega_i)}{|\Omega_i|^{\alpha}} \Big)^p$$

Moreover, if for any $p > 1$ we denote $(\Omega_1^p, \dots, \Omega_k^p)$ a minimizer in $\mathcal{P}_k(D)$ of F_p then, for $p \to +\infty$, possibly extracting a subsequence, we have

$$(\Omega_1^p, \dots, \Omega_k^p) \overset{L^1(D,\mathbb{R}^k)}{\longrightarrow} (\Omega_1, \dots, \Omega_k),$$

being $(\Omega_1, \dots, \Omega_k)$ a solution to (4.15).

In order to discretize the functional (4.19), we consider a rectangular box D in $\mathbb{R}^2$ or $\mathbb{R}^3$ endowed with a finite differences uniform grid with M discretization points along each axis direction. A function u will be numerically represented by its values at the grid points. We use basic first order centered finite differences in order to compute the gradient terms $|\nabla u_i|$, and basic quadrature formulas to compute all integrals. Similar approaches were already used in [103] and [A23]. The other integrals are approximated by using basic quadrature formulas on the grid. The optimization is done using a LBFGS quasi-Newton method implemented in Matlab [114], allowing pointwise bounds for all optimization variables. This optimization strategy motivated us to use the penalized formulation shown in (4.19).

For a general domain D we consider a rectangular box $D' \supset D$ on which we construct the finite differences grid. We set all functions involved in the computations to be equal to zero on grid points outside D and set the gradient to be equal to zero on the same points lying outside D. In this way the optimization is made only on points inside the desired domain D. Such type of techniques are called *fictitious domain methods* or *chimera methods* in the literature.

It is also possible to use a finite element framework in order to minimize (4.19) on general domains. In [A23, Section 3] one can find a detailed presentation of such a finite element framework in the context of Modica-Mortola functionals. Once the mass and rigity matrices for the Lagrange $\mathbf{P_1}$ finite elements are obtained, all functionals needed in our computations can be expressed using vector matrix products.

We make available an implementation of the algorithm described above which can be found online at the following link:

`https://github.com/bbogo/Cheeger_patch`.

This implementation uses the finite element framework for the optimization of (4.19). As detailed below it is also possible, for convex domains, to compare the Cheeger sets found by minimizing (4.19) with the exact Cheeger sets obtained using the representation formula provided by Kawohl and Lachand-Robert in [78].

We conclude with a series of numerical experiments:

- **Computation of α-Cheeger sets.** In this case, corresponding to $k = 1$, there is no need to use the penalization term. We optimize directly the non-penalized ratio between the Modica-Mortola ratio and the volume term with constraints $0 \le u \le 1$. Examples can be seen in Figure 4.7 for a domain in $\mathbb{R}^2$ and in Figure 4.8 for a domain in $\mathbb{R}^3$.

In order to test the accuracy of our method we compare our algorithm with an implementation of the Kawohl & Lachand-Robert explicit formula for finding Cheeger sets ($\alpha = 1$)

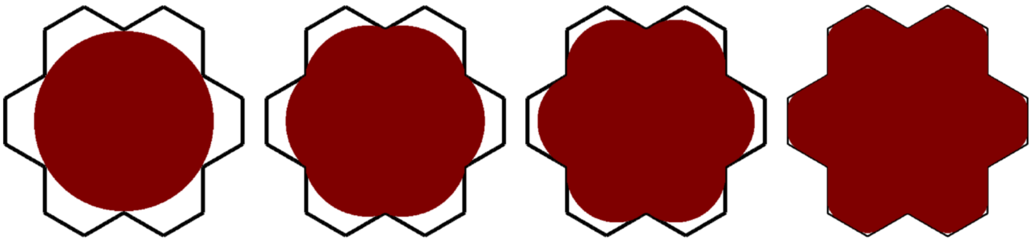

Figure 4.7: The α-Cheeger set for a non-convex set in $2D$, for $\alpha \in \{0.5001, 0.75, 1, 2\}$.

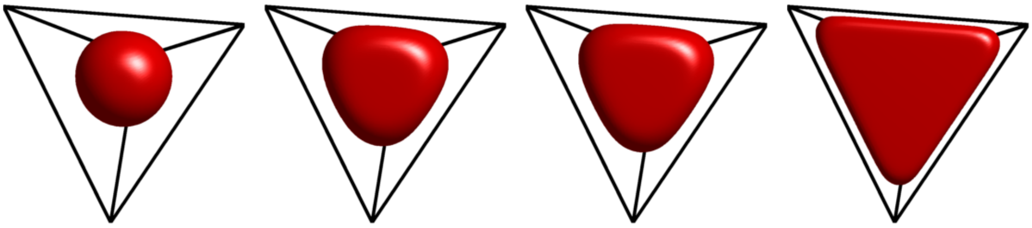

Figure 4.8: The α-Cheeger set for a regular tetrahedron in $3D$, for $\alpha \in \{0.667, 0.9, 1, 2\}$.

associated to convex sets in 2D [78]. As can be seen in Figure 4.9 the relaxation algorithm we propose is quite precise. We represent with red the ε-level set of the result obtained when minimizing (4.19) and with dotted blue the result obtained using the algorithm described in [78]. The value of ε used here is the same as the one used in the relaxed formulation. Choosing a level set corresponding to a larger value would correspond to a contour which does not touch the boundary of D, contrary to the known behavior of Cheeger sets. In the test cases presented below the results given by the two algorithms are almost indistinguishable. The relative errors obtained are small and, as expected, working on finer meshes leads to better approximations both of the Cheeger sets and of the Cheeger constants.

- **Computation of α-Cheeger clusters.** Some examples of Cheeger clusters can be seen in Figure 4.10. One can notice immediately that the cells are not necessarily convex, for instance when D is a square and $n = 5$. The results in the periodic case are in accordance with results in [37].

- **Computation of optimal packings.** We compute α-Cheeger clusters for α very close to $\frac{d-1}{d}$ and p *large*, which in our computations means at most 100. Choosing the parameter α close to $\frac{d-1}{d}$ forces the cells in the optimal configurations to be close to disks. We choose to use a p-norm approach since this regularizes the non-smooth problem of minimizing the maximal radius of a family of disks. The minimization of a p-norm instead of the ∞-norm is a natural idea, also used in [A15] for the study of partitions of a domain which minimize the largest

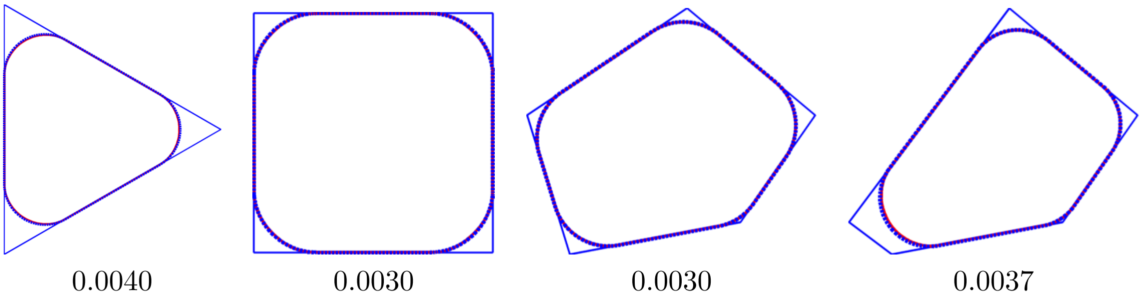

Figure 4.9: Comparison between results obtained when minimizing (4.19) (red) and the Kawohl & Lachand-Robert formula from [78] (dotted-blue). The numbers given below the pictures indicate the relative errors for the corresponding Cheeger constants.

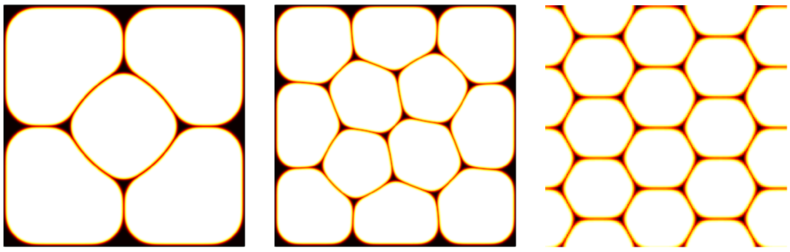

Figure 4.10: Cheeger clusters for problem (4.16) in a square: 5 cells, 12 cells, 16 cells (periodic).

fundamental eigenvalue of the Dirichlet-Laplace operator. To quantify our results we extract an approximation for the centers of the disks given by the densities obtained numerically. Once these centers are known, we perform a local minimization using `fmincon` in Matlab to obtain a more accurate description of the circle/sphere packing obtained.

In the planar case, we present some computational results in Figure 4.11. In our test cases the numerical algorithm based on the Γ-convergence result combined with the post-treatment algorithm generally produce configurations which are comparable to the best known results in the literature. We recall that one of the first papers regarding the circle packings in a circle was authored by Kravitz in 1967 [82]. In this paper we can find a conjecture regarding the 19-circle packing in a disk. The optimality of this 19-packing, presented in Figure 4.11, was proved by Fodor in [60]. Extensive numerical results up to thousands of circles were performed and collected on the website `http://www.packomania.com/`, maintained by Eckard Specht. In all cases, we compared our results with best ones available, listed on the above cited website. The numerical algorithm manages to capture the right results in cases where the optimal circle packing configuration is unique and rigid, like the case of 19 disks in a circle or 28 disks in an equilateral triangle. Moreover, we are able to capture the best known results even in cases where the solution is not unique, like in the case when we have 18 disks in a circle. One may notice that the best known configuration for 18 disks inside a circle contains disks of the same radius as the best known configuration for 19 disks. Therefore, when dealing with the circle, removing a disk from the 19-disk optimal packing gives a solution for the 18 disks case. This shows that the optimal configuration is not unique in this case. Our relaxed algorithm finds a configuration which is equivalent to the best known configurations given by other algorithms. We may observe slight differences between configurations in the relaxed setting and the refined results, which are due to the fact that when working with densities cells are not constrained to be disks.

Some examples of computations of optimal spherical packings for domains in $\mathbb{R}^3$ are presented in Figure 4.12. In this case, we observe again a good convergence to the best known configurations.

4.4 Optimal partitions for spectral functionals: an efficient algorithm

4.4.1 Numerical framework

In this section I recall the results obtained in [A15] and [A16] related to optimal partitions for spectral functionals. The main tool allowing us to study numerically such optimal partitions in an efficient way is an improvement of the algorithm proposed in [32] based on a grid restriction procedure.

First, let us recall that for a domain $D \subset \mathbb{R}^d$ and a subset $\omega \subset D$, the Dirichlet-Laplace eigenvalues verify

$$-\Delta u_k = \lambda_k(\omega) u_k, u_k \in H_0^1(\omega).$$

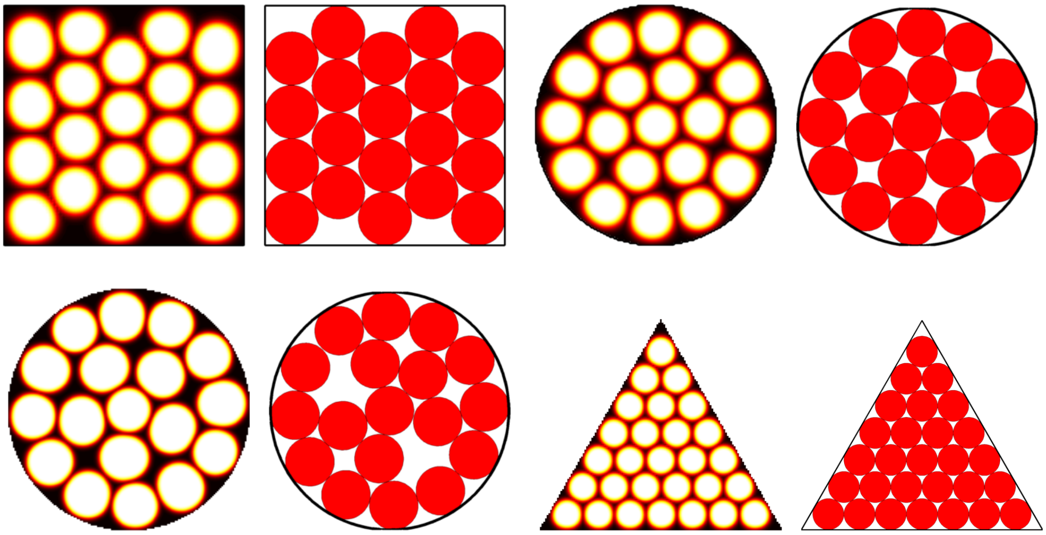

Figure 4.11: Circle packing examples in 2D for problem (4.17): density representation and local optimization.

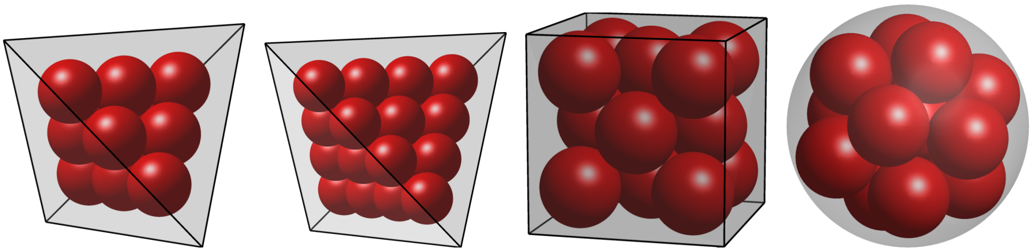

Figure 4.12: Sphere packing examples in 3D for problem (4.17).

The main challenge is to compute approximations of $\lambda_k(\omega)$ working with a discretization of D. The idea motivating this comes from the article [62] where the shape $\omega \subset D$ is encoded in a measure appearing as a penalization term

$$-\Delta u_k + \mu u_k = \lambda_k(\mu) u_k, u_k \in H_0^1(D).$$

In the case where μ is given by

$$\mu(X) = \begin{cases} 0 & \text{if } \operatorname{cap}(X \cap \omega) = 0 \\ +\infty & \text{otherwise} \end{cases}$$

then $\lambda(\mu)$ is precisely the first eigenvalue of the Dirichlet Laplacian operator on ω, where cap denotes the capacity. This formulation inspired the numerical method presented in [32] where a density approximation is used for approximating the shape ω. If φ is close to the characteristic function of ω then solving

$$(-\Delta + C(1-\varphi))u = \lambda_1(C,\varphi)u \tag{4.20}$$

for $u \in H_0^1(D)$ and $C \gg 1$ will give us approximations of the eigenvalues and eigenfunctions of ω. In [32] it is proved that when $\varphi = \chi_\omega$ and $C \to \infty$ then $\lambda_k(C,\varphi)$ converges to $\lambda_k(\omega)$ as $C \to \infty$. A quantitative convergence result is presented in [A19]

$$\frac{|\lambda_k(\Omega) - \lambda_k(\mu_C)|}{\lambda_k(\Omega)} \leq KC^{-1/(N+4)},$$

where $\mu_C = C(1-\chi_\omega)$.

Consider D a rectangular box in $\mathbb{R}^d$ endowed with a finite differences uniform grid. We consider an ordering for the points of this grid, allowing us to represent the discretization of a function u on this grid by a single vector $\bar{u}$. Let L be the matrix associated to the Laplace operator on this grid, i.e. $L\bar{u}$ computes the discrete Laplacian using $2d+1$ point stencils on the finite difference grid. We consider the discrete version of (4.20) given by

$$(L + C\text{diag}(1-\varphi))\bar{u} = \lambda_1(C,\varphi)\bar{u} \tag{4.21}$$

In this way we may give an approximation of the eigenvalues and eigenfunctions of a set using a finite difference grid on a larger set and an approximation of its characteristic function. This immediately shows why formulation (4.21) is so well adapted to study partitioning problems: we can perform computations on a fixed grid in order to find quantities related to some of its subsets.

Together with this advantage comes a drawback: we have a **fixed** computation grid regardless of the **size** of the cell ω, for which we wish to compute the eigenvalue. There is no advantage in using points far away from the current cell in order to impose Dirichlet boundary conditions. We propose that prior to the eigenvalue computation to look if the cell is localized to just one part of the grid and then restrict the computational domain to a suitably sized neighbourhood around the cell. In the sequel we call *computational neighbourhood* of a cell, the region to which we restrict the computations regarding a particular cell.

Given a density φ we identify its corresponding computational neighborhood as follows:

- First we find all the grid points $(P_i)_{i\in I}$ where the current density φ is greater than some threshold, equal to 0.01 in the computations.
- Next, we identify neighbors of points $(P_i)_{i\in I}$, i.e. grid points that are adjacent to one of these points. This process is made efficient using an adjacency matrix computed only once at the beginning of the simulation. To account for a non-trivial phase transition from 0 to 1, we repeat the process 5 times, successively finding the neighbors of points in the current sub-grid. More details are given in [A16, Section 2].
- Denote by R_φ the set of points in the computational neighborhood found above. Figure 4.13 illustrates a few examples in dimensions two, three and on surfaces. The blue (dark) points are grid nodes in the set $\{\varphi \geq 0.01\}$. The cyan (light) points are grid nodes which are neighbors of the set $\{\varphi \geq 0.01\}$. The union of these two sets of points is R_φ.

We compute the eigenvalue of the current cell using only the grid points inside the associated neighborhood R_φ found using the procedure described above. More precisely, we select from the matrix L, associated to the finite-differences Laplace operator, only the lines and columns corresponding to indices of points which are contained in the computational neighbourhood R_φ. In the initial phase of the computation the densities are random and the associated sub-grids may coincide with the whole grid. However, when the cells become localized the gain in speed is significant. A similar discrete framework is available when using finite element methods and the corresponding, described in [A16, Section 2]. The algorithm can be implemented on a periodic grid by modifying the adjacency matrix so that neighbours along the sides of the computational domain are included.

In each of the situations presented above, partitions of the domain D will be represented by n-tuples of functions $(\varphi_1, ..., \varphi_n)$ defined on D which verify the partition condition

$$\varphi_1 + ... + \varphi_n = 1$$

point-wise at each grid point. The initial condition will always be generated randomly and then projected on the constraint. In [32] the authors proposed the following projection:

$$\varphi_i \mapsto \frac{|\varphi_i|}{\sum_{i=1}^n |\varphi_i|}. \tag{4.22}$$

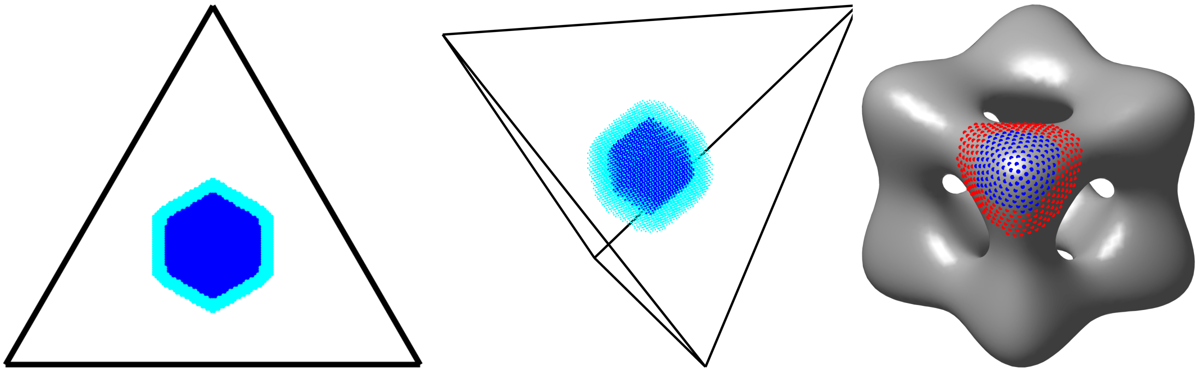

Figure 4.13: Illustration of computational neighborhoods in dimension two, three and on surfaces. Given φ a density function, dark points are points in the set $\{\varphi \geq 0.01\}$ and light points are their successive neighbors.

Apart from the fact that this projects a family of functions on constant sum equal to 1 constraint, this also makes every function φ_i have values in $[0, 1]$. This is important in light of the fact that the application $\varphi \mapsto \lambda_1(C, \varphi)$ is concave in φ [32]. Thus when minimizing $\sum_{i=1}^n \lambda_1(\varphi_i, C)$ each φ_i will become an extremal point in the family of functions with values in $[0, 1]$, and these extremal points are exactly the characteristic functions, taking values in $\{0, 1\}$.

Optimization algorithm. For simplicity, we denote by φ_i, $i = 1, ..., n$ the current density functions. At each iteration we perform the following:

- For each $i = 1, ..., n$, find the computational neighbourhood R_{φ_i} of φ_i.
- Compute the associated eigenvalue $\lambda_1(C, \varphi_i)$ and eigenfunction $\mathbf{u}_i = (u_j)_{j=1}^N$ solving (4.21) on the respective restricted grids R_{φ_i} (extended with zeros outside R_{φ_i}), where N is the size of the finite differences grid.
- Using the eigenfunction $\mathbf{u}_i = (u_j)_{j=1}^N$, compute the associated gradient of $\lambda_1(C, \varphi_i)$ with respect to each discrete variable. Denoting $\mathbf{v}_i = (u_j^2)_{j=1}^N$, according to [32] this is given by

$$\nabla \lambda_1(C, \varphi) = -C\mathbf{v}_i,$$

- **Gradient descent iteration:** update each density function φ_i using the opposite direction of the gradient

$$\varphi_i \mapsto \varphi_i + \alpha C \mathbf{v}_i,$$

- Performing the gradient descent iteration will break the partition condition. Therefore we project back on the constraint using the algorithm in [32], described in (4.22).
- Test if the new partition has a lower energy. If yes, then we continue, if not then we decrease the value of the step size α.
- Continue the optimization loop until we reach a preset maximal number of iterations, or the step α is smaller than 10^{-6}.

When dealing with many cells we wish to automatically classify the components of an optimized partition. In dimension two and on surfaces this can be achieved by simply counting neighbors. In dimension three the number of neighbors is not enough to classify the cells. We use the spectrum of the normalized Laplace-Beltrami operator of the surfaces of the cells to decide which cells are similar. The algorithm is described in [A16, Section 2, Algorithm 3].

4.4.2 Simulations and observations

The framework proposed in the previous section is efficient and allows to perform faster simulations in more complex contexts than those presented in [32]. In dimension two, various domains were considered with up to 1000 cells. The hexagonal partition emerges as the number of cells

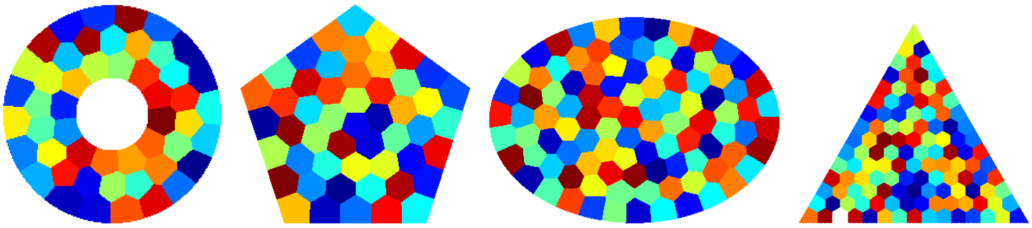

Figure 4.14: Partitions on various domains

increases, as can be observed in Figure 4.14. These simulations, in accord with previous simulations [32], [46], confirm the Caffarelli-Lin conjecture. We consider the same test as in [32]: the unit square with 512 cells on a 512 × 512 grid. We take random densities on a 32 × 32 grid and we perform an optimization on this grid in order to get an initial partition. We double the number of points in the grid along each axis direction and we interpolate the previous result on the new grid. We optimize again the result and we double the grid size until we reach the desired resolution. In Figure 4.15 we present the result obtained using the approach given above. We observe the presence of patches of regular hexagons as expected. We underline here that this test was made on a laptop with a 3.5GHz quad-core processor and 16GB of RAM in a few hours of computation time. Having more cells and better resolution is possible, as it can be seen in Figures 4.15, 4.16. Working with sparse matrices we optimize the memory cost used for storing the computational structure. For example in Figure 4.15, we present a case with 1000 cells on a grid of size 1000 × 1000 the computation takes about 12 hours and RAM consumption is less than 16GB when using sparse matrices to represent the cells. The 1000 × 1000 computation was made on a machine with an 8-core Xeon processor with 32 GB of RAM. However, the code was not parallelized, so eigenvalues were not computed in parallel. The RAM usage was of about 4GB in general, with spikes up to 12GB when performing the grid refinement step, probably due to the fact that several variables containing information having the size of the whole partition structure were present: among these one contains the current densities and one contains the gradient. Also, additional variables were created during the projection step. This example is presented to show the advantage of the grid restriction method with respect to the algorithm presented in [32], where for the same computation a supercomputer was needed[2].

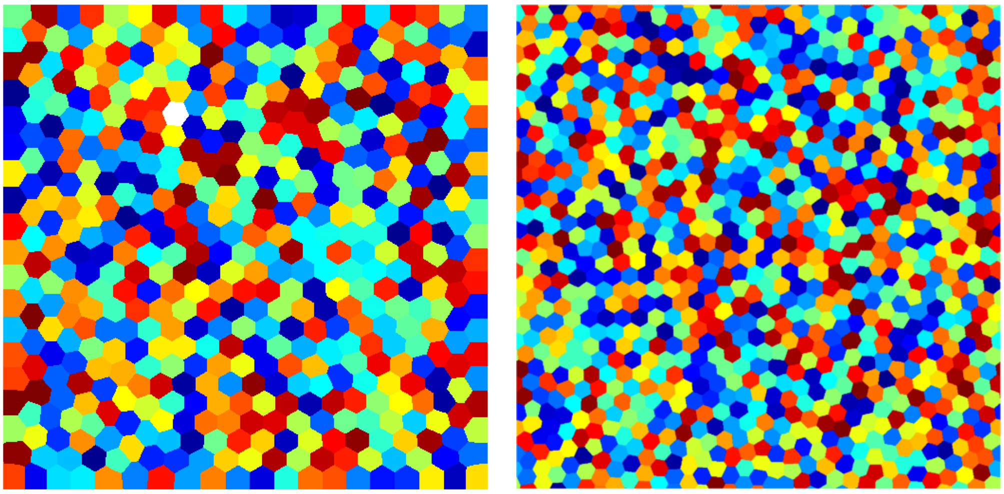

Figure 4.15: 512 cells on a grid of size 512 × 512 and 1000 cells on a grid of size 1000 × 1000.

It is possible to observe exact hexagonal patterns if we look at partitions of 2D shapes which are exact union of regular hexagons. These types of domains have also been investigated by

---

[2] The computation in [32] was made at Texas Advanced Computing Center

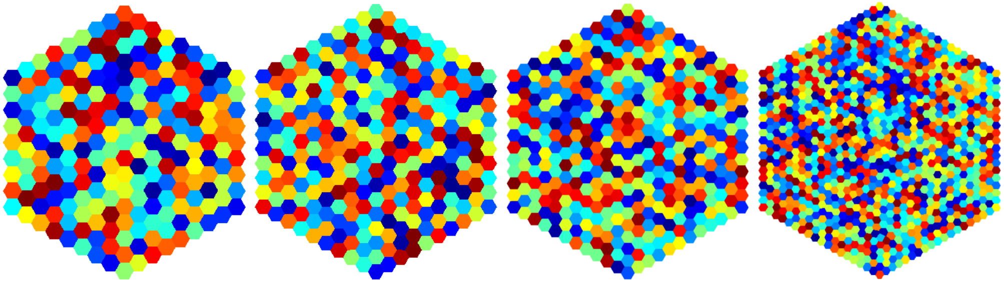

Figure 4.16: Optimal partitions on unions of hexagons for $217, 271, 397$ and 1027 cells. The partition of 397 cells is computed on a grid of size 1024×1024 and the partition into 1027 cells on a grid of size 510×510.

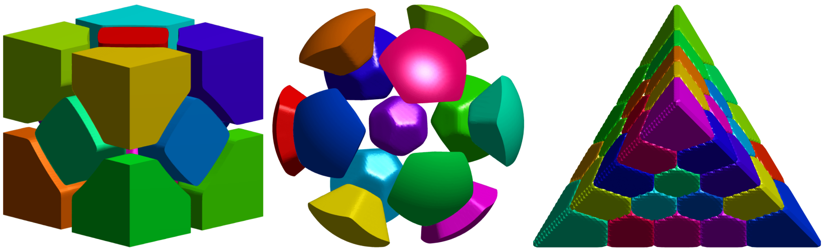

Figure 4.17: Optimal spectral partition for various 3D objects.

Bonnaillie-Noël, Helffer and Vial in [28] by adding cracks with Dirichlet conditions. In the computations presented here, we always start with an initial condition consisting of random densities and we arrive at an exact partition made of regular hexagons. This provides further evidence that the Caffarelli-Lin conjecture seems to be true. The partitions obtained are given in Figure 4.16.

The same algorithm can be used to simulate optimal multiphase configurations described in the work [39]. For particular choices of the penalization parameter this leads to another variational approach for computing circle packings. More details are given in [A16, Section 3.2]. Surface partitions can also be investigated, as shown in [A16, Section 3.3]. Hexagonal patterns emerge again in this case as the number of cells increases. This behavior is natural, since smooth surfaces behave locally like planar domains.

The efficiency of the proposed algorithm allows to investigate 3D partitions. Results in this sense are shown in Figure 4.17. The 3D analogue of the Caffarelli-Lin conjecture can be investigated by using periodic boundary conditions in a cube. Figure 4.18 shows the different configurations obtained for $n \in \{8, 16, 32\}$. Different classical configurations are obtained, including the Kelvin truncated octahedra and the Weaire-Phelan structure. A more careful investigation detailed in [A16, Section 3.4] shows that it is likely that the rhombic dodecahedron partition is the optimal one in the asymptotic case as $n \to \infty$. When partitioning a tetrahedron into a pyramidal number of cells of the form $n(n+1)(n+2)/6$ we obtain four types of cells illustrated in Figure 4.19. The classification of the cells was done in an automatic way using the Laplace-Beltrami spectrum of the surfaces of the cells. It can be noted that the cells inside the tetrahedron are rhombic dodecahedra.

4.4.3 Minimizing the maximal eigenvalue

The article [A15] deals with the minimization of p-norms of the first Dirichlet-Laplace eigenvalues of the cells. The objective is to deduce, for large enough p, approximations for the partition minimizing the maximal fundamental eigenvalue

$$\min \max_{i=1,\ldots,n} \lambda_1(\omega_i). \tag{4.23}$$

Figure 4.18: Some computations on the periodic cube: the Weaire-Phelan structure for $n = 8$, the Kelvin structure for $n = 16$ and the rhombic dodecahedron structure for $n = 32$.

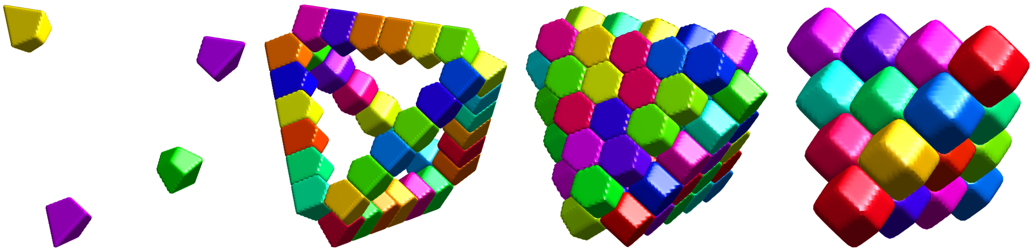

Figure 4.19: Automatic classification using the spectrum of the Laplace-Beltrami operator for the cells of the partition of the tetrahedron into 120 cells: 4 corner cells, 36 cells along the edges, 60 cells corresponding to the faces, 20 cells in the interior.

In some particular cases, solutions to the problem above are given by nodal partitions for some eigenfunction of the bounding domain D. See, for example [67] for more details.

We provide three methods for approximating solutions to problem (4.23):

- **using p-norms**: the algorithm proposed in the previous section can be easily adapted for optimizing p-norms of the first eigenvalues of each cell. The optimal partition evolves with respect to p and converges to the optimal partition for the maximum as $p \to \infty$. In Figure 4.20 an example is shown regarding the 4 partition of the equilateral triangle. This is one case where the change from $p = 1$ to p large is the most significative.
- **using penalization**: for $\varepsilon > 0$ we propose the functional

$$\sum_{i=1}^{n} \lambda_1(\omega_i) + \frac{1}{\varepsilon} \sum_{1 \leq i < j \leq n} (\lambda_1(\omega_i) - \lambda_1(\omega_j))^2, \tag{4.24}$$

  which, when minimized among partitions of D produces optimal partitions converging to solutions of (4.23) when $\varepsilon \to 0$. The optimization framework uses finite differences based on the density representation of the cells. The objective cost is therefore inexact unless the resolution is very fine. In order to have a more precise evaluation we extract the contours of the partition from the optimized densities and we use finite elements to compute the associated eigenvalues. The details of these computations are shown in [A15, Sections 4-5].
- **using Dirichlet-Neumann problems**: In some particular cases, the topology of the optimal partition found with one of the preceeding methods allows us to derive more information regarding the symmetry. In particular, some of the partitions found can be expressed as nodal domains of eigenfunctions corresponding to some well chosen Dirichlet-

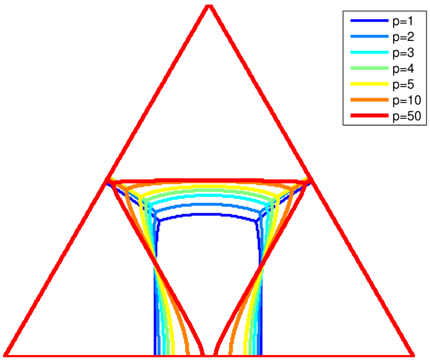

Figure 4.20: Evolution of the 4 partition of an equilateral triangle with respect to p.

Neumann problem on a particular polygon P:

$$\begin{cases} -\Delta u &= \Lambda_k(P)u \quad \text{in } P \\ u &= 0 \quad \text{on } S_j, 1 \leq j \leq q_D \\ \partial_n u &= 0 \quad \text{on } T_j, 1 \leq j \leq q_N, \end{cases} \tag{4.25}$$

where S_j, $1 \leq j \leq q_D$ and T_j, $1 \leq j \leq q_N$ are segments on the boundary or in the interior of P where Dirichlet and, respectively, Neumann boundary conditions are imposed. The nodal partition associated to $\Lambda_k(P)$ varies with the choice of the segments described above. A parametric search, described in detail in [A15], is performed to identify the configuration yielding a compatible nodal partition.

An example is shown in Figure 4.21 for the 8-partition of an equilateral triangle. Red segments indicate Dirichlet boundary conditions while blue ones indicate Neumann boundary conditions. Further aspects regarding this method are discussed in [A18] and the main ideas are summarized below:

- For the equilateral triangle, when $k = 8$, initial simulations using density based methods show that the optimal partition is symmetric. See Figure 4.21 a).
- Working on half of the equilateral triangle, consider the segment $[\mathsf{X}_s\mathsf{X}_t]$ where Dirichlet conditions are imposed. Consider also the vertical crack $[\mathsf{Y}_q\mathsf{Y}_r]$ where an additional Dirichlet condition is imposed. See Figure 4.21 b).
- The fifth eigenfunction for this configuration of boundary conditions has the desired nodal structure. The position of the points $\mathsf{X}_s, \mathsf{X}_t, \mathsf{Y}_q, \mathsf{Y}_r$ is modified until the nodal partition touches the endpoints of the segments $[\mathsf{X}_s\mathsf{X}_t]$, $[\mathsf{Y}_q\mathsf{Y}_r]$. See Figure 4.21 c).
- The nodal partition is symmetrized, giving a partition on the whole equilateral triangle. See Figure 4.21 d).

Whenever all three strategies above can be applied, the Dirichlet-Neumann method gives best results, followed by the penalization method.

4.5 Perspectives

Maximization of the minimal perimeter partitions [A3].

- Existence results should be extended to more general settings (star-shaped domains, simply connected domains in dimension two). Counterexamples should be found to guarantee that the existence results are optimal.
- The computation of the shape derivatives in (4.12), (4.13) are formal, assuming the optimal isoperimetric set or partition is unique. A computation of the directional derivatives in full generality should be made, following, for example, the ideas in [52, Chapter 9].
- Qualitative results regarding optimal sets and partitions should be investigated in more detail. Variational ideas could bring new insights and generate different proof methods

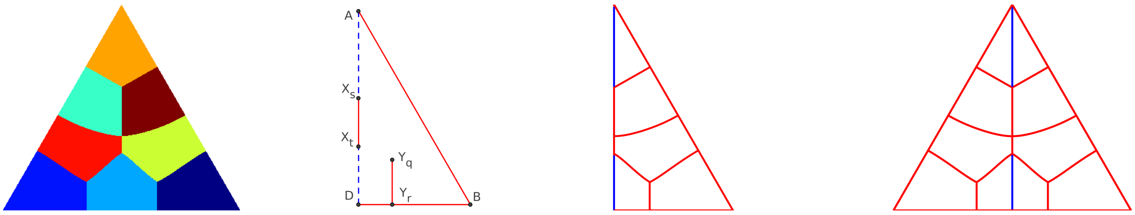

a) Optimal 8-partition b) Mixed problem c) Nodal partition d) Symmetrized partition

Figure 4.21: The 8-partition of the equilateral triangle. The leftmost picture shows the partition found using the penalization method. The next pictures show the Dirichlet-Neumann approach computing the 8-partition of the equilateral triangle. Red segments indicate Dirichlet boundary conditions and blue segments indicate Neumann boundary conditions.

than those in [55] or the other references working on this problem.

Spectral partitions [A15], [A16].

- To investigate optimal partitions in more detail, especially from the point of view of the precision of the objective cost, alternative numerical representations of the partition could be used. Starting from the approximate density representation of the partition, the Voronoi interface method [111], or a finite number of level sets could parametrize the resulting partition. FreeFEM together with MMG [48] could be used to mesh exactly all cells, providing a framework where the cost function is evaluated precisely. Notably, results in [A15] where the Dirichlet-Neumann method cannot be used could all be further improved.
- Alternative formulations could be used for the study of the min-max problem. For example

$$\min\{r : \lambda_1(\omega_i) \leq r, (\omega_i) \text{ is a partition of } D\}$$

  leads to a constrained problem where all constraints are differentiable. `fmincon` or `IPOPT` could be used to study the min-max problem in the discrete setting with potentially better results than the penalization method proposed in (4.24).
- Elucidate cases where no better candidate is known than a partition which cannot be optimal [67]. For example the 9-partition of the square or the 8 partition of the cube. Having more precise simulation methods could bring more clarity in these cases.

Chapter 5

The Polygonal Faber-Krahn inequality

5.1 Introduction

For every bounded, open set $\Omega \subset \mathbb{R}^2$ we consider the eigenvalue problem for the Laplace operator with Dirichlet boundary conditions

$$\begin{cases} -\Delta u &= \lambda u \quad \text{in } \Omega, \\ u &= 0 \quad \text{on } \partial\Omega. \end{cases} \tag{5.1}$$

The spectrum consists only on eigenvalues, which can be ordered (counting the multiplicity),

$$0 < \lambda_1(\Omega) \le \lambda_2(\Omega) \le \cdots \le \lambda_k(\Omega) \cdots \to +\infty.$$

Lord Rayleigh conjectured in 1877 that the first eigenvalue is minimal on the disc, among all other planar domains of the same area. The proof was given in by Faber and Krahn in the 1920s. A survey of the topic can be found in [69, 68].

In their book of 1951, Pólya and Szegö have conjectured a polygonal version of this inequality (see [106, page 158]). Denote by $\mathcal{P}_n$ the family of simple polygons with n sides in $\mathbb{R}^2$ and for every $n \ge 3$ consider the problem

$$\min_{P \in \mathcal{P}_n, |P| = \pi} \lambda_1(P). \tag{5.2}$$

They propose the following:

Pólya-Szegö Conjecture (1951). *The unique solution to problem (5.2) is the regular polygon with n sides and area π.*

This question, easy to state, has puzzeld many mathematicians in the last seventy years, but no significant progress has been made. The conjecture holds true for $n = 3$ and $n = 4$. A proof can be found, for instance, in [68] as a straightforward application of the Steiner symmetrization principle (the original proof can be found in [106]). However, Steiner symmetrization techniques do not allow the treatment of the case $n \ge 5$ since, performing this procedure, the number of vertices could possibly increase. We are not aware of further results regarding this conjecture. Neverteless, we mention a new approach, which applies only to triangles, proposed by Fragalà and Velichkov in [61], establishing that equilateral triangles are the only critical points for the first eigenvalue.

It is quite straightforward to prove the existence of an optimal n-gon in the closure of the set of simple n-gons with respect to the Hausdorff distance of the complements, as shown in [68, Chapter 3]. It has precisely n edges, but it is possibly degenerate in the sense that a vertex could belong to another edge. However, it is not even known that this polygon has to be convex! Meanwhile, many numerical experiments have been performed for small values of n (see for instance [8], [24, Chapter 1], [54]) which all suggest the validity of the conjecture.

In the paper [A7] in collaboration with D. Bucur, we present results which justify that a hybrid proof of the Polyà-Szegö conjecture can be given, based on theoretical results and certified numerical computations. The proof strategy is described below and more details are be given in subsequent sections.

Local minimality of the regular n-gon. A polygon with n vertices can be completely characterized using $2n$ real variables. Thus problem (5.2) is reduced to a finite dimensional optimization problem. A simple eigenvalue is differentiable with respect to domain perturbations [71, Chapter 5], therefore computation of first and second partial derivatives can provide the relevant information related to local minimality. While classical shape derivative formulas for λ_1 written as linear forms of the normal displacement of the boundary remain valid on polygons, this is not the case for the second shape derivatives [71, Chapter 5]. Based on the recent paper of A. Laurain [88] we compute second shape derivatives for λ_1 using volume integrals to avoid the need of additional regularity hypotheses. This allows us to compute the Hessian matrix for λ_1 when the coordinates of the vertices are taken as variables.

A particular change of basis makes the Hessian matrix of the scale invariant functional $P_n \mapsto \lambda_1(P_n)|P_n|$ block circulant, allowing us to completely characterize its spectrum. The spectrum consists of the eigenvalue 0 with multiplicity 4 (corresponding to translations, rotations and homotheties) and another $2n-4$ eigenvalues. We show that if the remaining $2n-4$ eigenvalues are strictly positive then the regular polygon is indeed a local minimum. The complexity of the formulas for the non-zero eigenvalues does not allow us to solve theoretically the question of local minimality. This motivates us to use a numerical method instead.

Validated numerical computations. When using finite element methods to approximate solutions of a PDE multiple sources of error exist: discretization errors, meshing errors, machine precision errors. All these sources of errors need to be taken into account to validate a numerical computation. Given a mesh size h, the difference between the analytical solution and the one obtained with finite elements can be estimated using a term of the form $O(h^k)$ where the power k depends on the type of finite elements and the norm used. While general classical references ignore the constants involved and focus on the order k, in our case, precise information regarding the corresponding constants are necessary. Based on the work [90] we find explicit estimates for all PDEs involved in the computations of the eigenvalues of the Hessian matrix. The quantification of the errors made by working with floating point arithmetics is a more delicate issue. Generally, one needs to perform all computations using an interval arithmetics software like Intlab [109]. Operations on floating point numbers are transformed into operations on intervals. The resulting interval is guaranteed to contain the exact result. Using these techniques we manage to show that for $n \in \{5,6,7,8\}$ the regular n-gon is a local minimizer, up to floating point errors involved in solving the large FEM problems. Ideally one should perform the FEM computations using interval arithmetics, but this is the subject of future works since different difficulties need to be overcome: validation of large linear systems and matrix eigenvalue problems, improvement of the constants and convergence order in the *a priori* estimates for the FEM problems.

Reducing the proof to a finite number of numerical computations. The final point of our strategy is to limit the space of n-gons that are relevant competitors with the regular one to a region which can be exhausted through numerical computations. To do this we have the following steps:

(i) The local minimality region. Based on the H^{2+s} regularity of the first eigenfunction on a regular polygon we show that the eigenvalues of the Hessian matrix vary continuously in a quantified way for n-gons close to the regular one. Therefore, the computation of the eigenvalues of the Hessian for the regular n-gon will give a quantified neighborhood of local minimality. Fixing 2 vertices (amounting for the flexibility given by the four zero eigenvalues), the strict positivity of $2n-4$ remaining eigenvalues of the Hessian will be preserved in a neighborhood of the regular n-gon.

(ii) Geometric inequalities. We provide analytic upper bound for the diameter and lower bounds for the inradius and minimal edge length of an optimal n-gon. This allows to reduce the space of admissible n-gons to a compact region of $\mathbb{R}^{2n-4}$. Moreover, explicit estimates show that performing one validated numerical computation can provide a quantified neighborhood of the current n-gon where no minimizer exists.

(iii) Finite number of numerical computations. Following the previously presented facts, outside the local minmality neighborhood, the compact region of $\mathbb{R}^{2n-4}$ corresponding to the geometric constraints described above, can be covered using a finite number of balls of a given, sufficiently small radius. Performing a validated computation for an n-gon with coordinates in every such ball is enough to validate the conjecture. If the validation procedure fails, a counterexample will be found (highly unlikely, in view of the numerical evidence for the conjecture). For now, this proof strategy is only formal, since we do not have an estimation regarding the number of computations necessary to complete the proof. Further qualitative results (like the convexity of optimizers) would reduce the search space and improve the feasibility of this hybrid proof strategy.

In the following sections I present the main ideas in connection with the strategy described above. Section 5.2 deals with the computation of the second shape derivative of a simple eigenvalue among Lipschitz domains. Section 5.3 contains details regarding the computation of the eigenvalues of the Hessian of λ_1 on the regular n-gon and the explicit estimates related to their numerical approximations using $\mathbf{P_1}$ finite elements. In Section 5.4 geometric estimates for optimal n-gons are given and the exhaustion of the admissible space through a finite number of numerical computations is discussed. The chapter concludes in Section 5.5 with a series of perspectives regarding theoretical qualitative properties and numerical aspects related to the proposed proof strategy.

5.2 Second shape derivatives and Hessian matrix

It is well established that simple Dirichlet-Laplace eigenvalues are differentiable with respect to the shape of the domain without any regularity assumptions [71, Section 5.7]. The case of multiple eigenvalues is more involved, but it can be shown that directional derivatives exist [68, Section 2.5.3], [77, Chapter VII]. The classical formula for the shape derivative of a simple eigenvalue λ of (5.1) is

$$\lambda'(\Omega)(\theta) = -\int_{\partial\Omega} (\nabla u \cdot \mathbf{n})^2 \theta \cdot \mathbf{n}, \tag{5.3}$$

where u is the $L^2(\Omega)$ normalized eigenfunction associated to λ and $\mathbf{n}$ is the outer normal vector to $\partial\Omega$. Formula (5.3) contains an integral of the square of the normal derivative of the eigenfunction u on the boundary and is valid under certain regularity assumptions. For example if $u \in H^2(\Omega)$ the trace of its gradient is well defined and belongs to $L^2(\partial\Omega)$. When Ω is convex the results of [64, Chapter 2] show that u belongs to $H^2(\Omega)$ so the boundary formula for the shape derivative is valid. It can be observed that formula (5.3) gives the shape derivative as a linear form depending on the normal component of the perturbation field $\theta \cdot \mathbf{n}$. In [100] it is shown that this structure holds for very general functionals under regularity assumptions. Moreover, in regular contexts the second derivative also has a particular structure. The second derivative of a simple eigenvalue is described, for example, in [71, Section 5.9] for shapes that are C^3 regular. The formula and methods used to obtain it cannot be used in the case of polygons. It is likely that the search for an answer to this question using the structure theorem in [100] prevented earlier attempts to compute the second shape derivative in contexts where less regularity is present.

The idea that started our work on the Polyà-Szegö conjecture comes from a paper of A. Laurain [88], formalizing ideas present in other previous works like [89]. The use of distributed shape derivative formulas, i.e. volume integrals instead of boundary ones, requires less regularity for the domain and perturbation fields. Distributed shape derivative formulas, for a generic shape differentiable functional $\Omega \mapsto J(\Omega)$, have the structure

$$J'(\Omega)(\theta) = \int_\Omega \mathbf{S}_1 : D\theta + \mathbf{S}_0 \cdot \theta \tag{5.4}$$

where $\mathbf{S}_0 \in L^1(\Omega, \mathbb{R}^2)$ is a first order tensor and $\mathbf{S}_1 \in L^1(\Omega, \mathbb{R}^{2\times 2})$ is a second order tensor. When $\mathbf{S}_1$ is regular enough we have $\operatorname{div} \mathbf{S}_1 = \mathbf{S}_0$ (see [89]). This implies that when Ω is regular enough, the use of the divergence theorem allows us to transform formula (5.4) into the standard form (5.3).

In [A7] we compute the distributed shape derivative for a simple eigenvalue $\lambda(\Omega)$ and we arrive at the formula

$$\lambda'(\Omega)(\theta) = \int_\Omega \mathbf{S}_1^\lambda : D\theta, \text{ where } \mathbf{S}_1^\lambda = (|\nabla u|^2 - \lambda(\Omega)u^2)\,\mathbf{Id} - 2\nabla u \otimes \nabla u. \tag{5.5}$$

As usual $\mathbf{Id}$ denotes the identity 2×2 matrix and $\otimes$ denotes the tensor product: if $a, b \in \mathbb{R}^d$ then $a \otimes b = (a_i b_j)_{1\le i\le j\le d} \in \mathbb{R}^{d\times d}$. Formula (5.5) holds when Ω is Lipschitz and $\theta \in W^{1,\infty}(\mathbb{R}^2;\mathbb{R}^2)$. The advantage of formula (5.5) is that it can be further differentiated without imposing additional regularity assumptions, using the same method described in [A7, Section 2]. We arrive, thus at the formula for the second order distributed Fréchet derivative, given for $\theta, \xi \in W^{1,\infty}(\mathbb{R}^2;\mathbb{R}^2)$ by

$$\lambda''(\Omega)(\theta,\xi) = \int_\Omega \mathcal{K}^\lambda(\theta,\xi)$$

with

$$\begin{aligned}\mathcal{K}^\lambda(\theta,\xi) = {} & -2\nabla\dot u(\theta)\cdot\nabla\dot u(\xi) + 2\lambda(\Omega)\dot u(\theta)\dot u(\xi) + \mathbf{S}_1^\lambda : (D\theta \operatorname{div}\xi + D\xi \operatorname{div}\theta) \\ & + \left(-|\nabla u|^2 + \lambda u^2\right)(\operatorname{div}\xi \operatorname{div}\theta + D\theta^T : D\xi) \\ & + 2(D\theta D\xi + D\xi D\theta + D\xi D\theta^T)\nabla u\cdot\nabla u \\ & - \left[\lambda'(\Omega)(\theta)\operatorname{div}\xi + \lambda'(\Omega)(\xi)\operatorname{div}\theta\right]u^2, \end{aligned} \tag{5.6}$$

where $\dot u(\theta), \dot u(\xi) \in H_0^1(\Omega)$ are the material derivatives of the eigenfunction u in directions θ, ξ, respectively, defined by the variational formulation

$$\begin{aligned}&\int_\Omega (\nabla\dot u(\theta)\cdot\nabla v - \lambda(\Omega)\dot u(\theta)v)\,dx \\ &\qquad = \int_\Omega \left(-(\operatorname{div}\theta\,\mathbf{Id} - D\theta - D\theta^T)\nabla u\cdot\nabla v + \lambda'(\Omega)(\theta)uv + \lambda(\Omega)uv\operatorname{div}\theta\right)dx,\end{aligned} \tag{5.7}$$

holding for every $v \in H_0^1(\Omega)$. Notice that $\dot u(\theta)$ is defined up to a multiple of u, moreover, the second shape derivative does not change if $\dot u(\theta), \dot u(\xi)$ are changed with a multiple of u. Therefore an additional condition is considered to have uniqueness of solutions in (5.7), for example $\int_\Omega u\dot u(\theta) = 0$. The expression (5.6) is new, up to our knowledge and is valid when the shape Ω, and the perturbation fields θ, ξ are Lipschitz, including the case of polygons.

In the following we restrict our analysis to polygonal domains Ω. We consider a particular class of perturbation vector fields $\theta \in W^{1,\infty}(\mathbb{R}^2;\mathbb{R}^2)$ preserving the polygonal character of the n-gon Ω. For simplicity, we only define the perturbation fields inside Ω, their extension outside Ω, being arbitrary. Denote the vertices of the polygon by $\mathbf{a}_i \in \mathbb{R}^2$ and consider associated vectors $\theta_i \in \mathbb{R}^2$ for $i = 0, ..., n-1$. Consider a triangulation $\mathcal{T}$ of Ω such that the edges of Ω are edges of some triangles in $\mathcal{T}$. Two examples are shown in Figure 5.1, the symmetric one having particular interest for the sequel. On this triangulation consider $\mathbf{P_1}$ (piece-wise affine) functions φ_i such that $\varphi_i(\mathbf{a}_j) = \delta_{ij}$. The functions φ_i are equal to zero at any existing internal nodes of the triangulation $\mathcal{T}$. This allows to define the global perturbation $\theta = \sum_{i=0}^{n-1} \theta_i\varphi_i \in W^{1,\infty}(\Omega;\mathbb{R}^2)$.

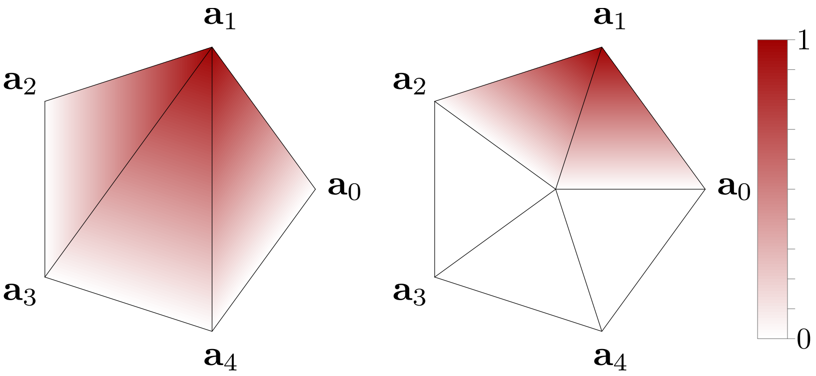

Figure 5.1: Examples of admissible triangulations used for defining perturbations on a polygon and graphical view of the function φ_1.

Taking the coordinates of the polygon as variables $\mathbf{x} = (\mathbf{a}_0, ..., \mathbf{a}_{n-1})$ and using perturbation fields of the form described above, the associated gradient vector and Hessian matrix can be computed using the previously found shape derivative formulas. In particular, we have

$$\nabla\lambda(\mathbf{x}) = \Big(\int_\Omega \mathbf{S}_1^\lambda \nabla\varphi_i\Big)_{i=0,...,n-1} \tag{5.8}$$

Following the notation of [88], we introduce the functions $\mathbf{U}_i \in H_0^1(\Omega;\mathbb{R}^2),\ i = 0, ..., n-1$ such that $\dot{u}(\theta) = \sum_{i=0}^{n-1} \theta_i \cdot \mathbf{U}_i$. Using (5.7) we get the set of two PDEs: $\mathbf{U}_i \in H_0^1(\Omega;\mathbb{R}^2)$,

$$\begin{aligned}\int_\Omega (D\mathbf{U}_i\nabla v - \lambda(\Omega)\mathbf{U}_i v)\,dx &= \int_\Omega [-(\nabla\varphi_i \otimes \nabla u)\nabla v + 2(\nabla u \odot \nabla v)\nabla\varphi_i]\,dx \\ &+ \int_\Omega \mathbf{S}_1^\lambda\nabla\varphi_i \int_\Omega uv\,dx + \lambda(\Omega)\int_\Omega uv\nabla\varphi_i\,dx,\end{aligned} \tag{5.9}$$

for every $v \in H_0^1(\Omega)$ with the normalization condition

$$\int_\Omega u\mathbf{U}_i\,dx = 0, \tag{5.10}$$

so that the system of equations (5.9) - (5.10) has a unique solution $\mathbf{U}_i$.

Theorem 5.2.1. *The Hessian matrix $\mathbf{N}^\lambda \in \mathbb{R}^{2n\times 2n}$ of a simple Dirichlet-Laplace eigenvalue (5.1) with respect to the coordinates of the n-gon is given by the following $n \times n$ block matrix*

$$\mathbf{N}^\lambda = (\mathbf{N}_{ij}^\lambda)_{0\le i,j\le n-1}$$

where the 2×2 blocks are given by

$$\begin{aligned}\mathbf{N}_{ij}^\lambda = &\int_\Omega (-2D\mathbf{U}_iD\mathbf{U}_j^T + 2\lambda(\Omega)\mathbf{U}_i\mathbf{U}_j^T + \nabla\varphi_i\otimes\mathbf{S}_1^\lambda\nabla\varphi_j + \mathbf{S}_1^\lambda\nabla\varphi_i\otimes\nabla\varphi_j)\,dx \\ &+ \int_\Omega \left(-|\nabla u|^2 + \lambda(\Omega)u^2\right)(2\nabla\varphi_i\odot\nabla\varphi_j)\,dx \\ &+ 2\int_\Omega [(\nabla\varphi_i\cdot\nabla u)(\nabla\varphi_j\otimes\nabla u) + (\nabla\varphi_j\cdot\nabla u)(\nabla u\otimes\nabla\varphi_i) + (\nabla\varphi_i\cdot\nabla\varphi_j)(\nabla u\otimes\nabla u)]\,dx \\ &- \int_\Omega u^2\left[\nabla\varphi_i\otimes\left(\int_\Omega \mathbf{S}_1^\lambda\nabla\varphi_j\,dx\right) + \left(\int_\Omega \mathbf{S}_1^\lambda\nabla\varphi_i\,dx\right)\otimes\nabla\varphi_j\right]\,dx\end{aligned} \tag{5.11}$$

where $\mathbf{U}_i \in H^1(\Omega,\mathbb{R}^2),\ i = 0, ..., n-1$ are solutions of (5.9)-(5.10).

It should be noted that in formula (5.11) all the terms that do not contain the material derivatives $\mathbf{U}_i$ (5.9) are explicit in terms of the eigenfunction u and the functions φ_i (related to the geometry of the n-gon).

The results in [A7, Section 3] show that the coefficients of the Hessian matrix (5.11) vary continuously, in a quantifiable way, with respect to the coordinates of the vertices of the n-gon. Such stability results for the eigenvalue and the corresponding eigenfunction are rather classical. For instance, Savaré and Schimperna [110] give estimates for solutions of the Laplace equation in the class of sets satisfying a uniform cone condition while Burenkov and Lamberti [14], Feleqi [56] discuss the eigenfunctions. The quantitative stability of the eigenvalues for domain perturbations is discussed in [105]. On the other hand, the stability of the terms involving the material derivatives (5.9) is more delicate and exploits the $H^{2+s}(\Omega)$ regularity of the eigenfunctions of a regular n-gon. This is the subject of [A7, Section 3].

The regular n-gon. We are interested in proving the local minimality of the regular n-gon, therefore in the following we restrict ourselves to this case and we consider the first eigenvalue $\lambda_1(\Omega)$. In particular, the first eigenfunction has the same symetries as the regular n-gon. We also assume that the functions φ_i are defined using a symmetric triangulation, shown in Figure 5.1. In [A7, Section 2] we show that these symmetry considerations allow us to obtain a simpler formula for the Hessian Matrix for the regular n-gon.

Furthermore, the scaling properties of the Dirichlet-Laplace eigenvalue imply that the quantity $\lambda_1(\Omega)|\Omega|$ is **scale invariant**. Therefore, we focus on this quantity which allows a more straightforward characterization of the minimality of solutions of (5.2) since it gives rise to an unconstrained problem. The associated Hessian matrix is given below.

Proposition 5.2.2. *In the case where Ω is a regular n-gon and the triangulation $\mathcal{T}$ defining φ_i is symmetric the Hessian matrix of $\lambda_1(\Omega)|\Omega| = \mathcal{A}(\mathbf{x})\lambda_1(\mathbf{x})$ in terms of the coordinates of the polygon has the 2×2 blocks $\mathbf{M}^\lambda_{ij}$, $0 \le i,j \le n-1$ given by*

$$\begin{aligned}\mathbf{M}^\lambda_{ij} = &-2|\Omega|\int_\Omega (D\mathbf{U}_i D\mathbf{U}_j^T - \lambda_1(\Omega)\mathbf{U}_i\mathbf{U}_j^T)\\ &-\lambda_1(\Omega)\int_\Omega [\nabla\varphi_i\otimes\nabla\varphi_j - \nabla\varphi_j\otimes\nabla\varphi_i]\\ &+2|\Omega|\int_\Omega (\nabla\varphi_i\cdot\nabla\varphi_j)(\nabla u_1\otimes\nabla u_1).\end{aligned}\tag{5.12}$$

The simplified formula (5.12) for the Hessian of the product of the area and the first eigenvalue has three terms:

- The first one is related to the decomposition $\mathbf{U}_i$ of the material derivatives given in (5.9). Furthermore, these terms are computed using the bilinear form from the variational formulations of $\mathbf{U}_i$, which will be essential in improving the estimates in the numerical simulations. This part of the Hessian is negative definite.
- The second term is proportional to the Hessian of the area given in [A7, Section 2]. The associated blocks are non-zero only when $|i-j| = 1$ (modulo n). This part has both positive and negative eigenvalues.
- The third term involves only the first eigenfunction u_1 and the functions φ_i described in the symmetric configuration shown in Figure 5.1. The associated blocks are non-zero only when $|i-j| \le 1$. This part of the Hessian is positive definite.

Although the expression of the Hessian given in (5.12) is explicit, its positive definiteness is not obvious. The analysis of the eigenvalues of this matrix is continued in Section 5.3.

5.3 Eigenvalues of the Hessian matrix and their numerical approximations

In this section, the spectrum of $\mathbf{M}^\lambda$, the Hessian matrix of $\mathbf{x} \mapsto \lambda(\mathbf{x})\mathcal{A}(\mathbf{x})$ described in (5.12) is investigated. For simplicity we use the notation $\theta = 2\pi/n$ and $\mathbb{P}_n$ denotes the regular n-gon with unit circumradius, centered at the origin and having the first vertex $\mathbf{a}_0 = (1,0)$. The main ideas elaborated in detail in [A7, Section 4] are resumed below:

- Translations, rotations and homotheties do not change the scale invariant quantity $\lambda(\mathbf{x})\mathcal{A}(\mathbf{x})$. Using direct observations related to the matrices involved, or more explicitly, considering perturbations of the regular n-gon preserving its regularity, we show that $\mathbf{M}^\lambda$ has four zero eigenvalues associated to the eigenvectors

$$\mathbf{t}_x = \begin{pmatrix} 1 \\ 0 \\ 1 \\ 0 \\ \dots \\ 0 \end{pmatrix}, \mathbf{t}_y = \begin{pmatrix} 0 \\ 1 \\ 0 \\ 1 \\ \dots \\ 1 \end{pmatrix}, \mathbf{s} = \begin{pmatrix} 1 \\ 0 \\ \cos\frac{2\pi}{n} \\ \sin\frac{2\pi}{n} \\ \dots \\ \sin\frac{2(n-1)\pi}{n} \end{pmatrix}, \mathbf{r} = \begin{pmatrix} 0 \\ -1 \\ \sin\frac{2\pi}{n} \\ -\cos\frac{2\pi}{n} \\ \dots \\ -\cos\frac{2(n-1)\pi}{n} \end{pmatrix}. \tag{5.13}$$

- Having four extra degrees of freedom, we may fix two vertices $\mathbf{a}_0, \mathbf{a}_1$ and consider the minimization of $\mathbf{x} \mapsto \lambda_1(\mathbf{x})\mathcal{A}(\mathbf{x})$ using the remaining $2n-4$ variables $\mathbf{a}_2, ..., \mathbf{a}_{n-1}$. The associated Hessian matrix is a $(2n-4)\times(2n-4)$ principal submatrix of $\mathbf{M}^\lambda$. This submatrix is positive definite, provided the remaining $2n-4$ eigenvalues of $\mathbf{M}^\lambda$ are strictly positive. (see [72, Theorem 4.3.28]) Moreover, continuity arguments in [A7, Section 3] ensure that the positive definiteness of this $(2n-4)\times(2n-4)$ matrix is preserved in a neighborhood of the regular n-gon, proving local minimality.
  Therefore, the proof of local minimality of the regular n-gon is reduced to showing that the remaining $2n-4$ non-zero eigenvalues of $\mathbf{M}^\lambda$ are strictly positive.
- The matrix $\mathbf{M}^\lambda$ computed in (5.12) uses the usual Euclidean basis. Making a change of basis considering radial and tangential coordinates for each vertex shows that circular permutations of the vertices do not change the associated Hessian matrix. Therefore, the Hessian matrix becomes block circulant and using results in [115] we can characterize its spectrum using a set of 2×2 matrices

$$\mathbf{B}_{\rho_k} = \mathbf{M}_0 + \mathbf{M}_1(\rho_k \mathbf{R}_\theta) + ... + \mathbf{M}_{n-1}(\rho_k\mathbf{R}_\theta)^{n-1},$$

  constructed using the blocks on the first line of $\mathbf{M}^\lambda$, roots of unity $\rho_k = \exp(ik\theta)$ and usual rotation matrices $\mathbf{R}_\tau$.

Tedious, but explicit computations show that the eigenvalues of $\mathbf{B}_{\rho_k}$, and as a consequence those of $\mathbf{M}^\lambda$, can be expressed in terms of u_1, U_0^1, U_0^2.

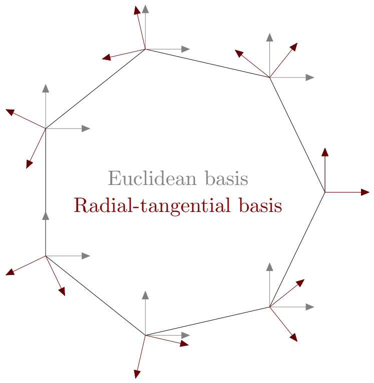

Figure 5.2: Changing the basis from the Euclidean one to use radial and tangential coordinates. The Hessian matrix becomes block circular in this setting.

Theorem 5.3.1. *For* $0 \leq k \leq n-1$ *we have* $\mathbf{B}_{\rho_k} = \begin{pmatrix} \alpha_k & i\gamma_k \\ -i\gamma_k & \beta_k \end{pmatrix}$ *with*

$$\alpha_k = \frac{2n(1-\cos(k\theta))}{\sin\theta}\int_{T_0}(\partial_x u_1)^2 - 2|\mathbb{P}_n|a(U_0^1, \sum_{j=0}^{n-1}\cos(jk\theta)(\cos(j\theta)U_j^1 + \sin(j\theta)U_j^2))$$

$$\beta_k = \frac{2n(1-\cos(k\theta))}{\sin\theta}\int_{T_0}(\partial_y u_1)^2 - 2|\mathbb{P}_n|a(U_0^2, \sum_{j=0}^{n-1}\cos(jk\theta)(-\sin(j\theta)U_j^1 + \cos(j\theta)U_j^2))$$

$$\begin{aligned}\gamma_k &= -2|\mathbb{P}_n|a(U_0^1, \sum_{j=0}^{n-1}\sin(jk\theta)(-\sin(j\theta)U_j^1 + \cos(j\theta)U_j^2)) \\ &= 2|\mathbb{P}_n|a(U_0^2, \sum_{j=0}^{n-1}\sin(jk\theta)(\cos(j\theta)U_j^1 + \sin(j\theta)U_j^2))\end{aligned}$$

Moreover, the eigenvalues of $\mathbf{B}_{\rho_k}$ *are given by*

$$\mu_{2k} = 0.5(\alpha_k + \beta_k - \sqrt{(\alpha_k-\beta_k)^2 + 4\gamma_k^2}),\ \mu_{2k+1} = 0.5(\alpha_k + \beta_k + \sqrt{(\alpha_k-\beta_k)^2 + 4\gamma_k^2}).$$

As a consequence, the eigenvalues of the Hessian matrix $\mathbf{M}_\lambda$ *given in* (5.12) *are exactly* μ_j, $j = 0, ..., 2n-1$.

Despite the explicit character of the formulas found in Theorem 5.3.1, the positivity of the $2n-4$ non-zero eigenvalues is not obvious and we do not have a theoretical argument for now. Nevertheless, these eigenvalues can be approximated numerically using finite elements, motivating us to find explicit error bounds justifying their positivity. The choice of finite elements compared to other methods like fundamental or particular solutions [15] is motivated by the complexity of the equations of the material derivatives (5.9). Solutions to these equations are not even in $H^2(\Omega)$, since discontinuities in the derivatives occur along segments of the triangulation $\mathcal{T}$ defining φ_i, depicted in Figure 5.1.

The steps needed to obtain certified error estimates for coefficients of $\mathbf{M}^\lambda$ using $\mathbf{P_1}$ finite elements are summarized as follows:

- Certified approximations for λ_1 and u_1 are well known and described in [91]. We describe in detail in [A7, Section 5] the constants appearing in the estimates

  $$|\lambda_1 - \lambda_{1,h}| = O(h^2), \|\nabla u_1 - \nabla u_{1,h}\|_{L^2(\Omega)} = O(h), \|u_1 - u_{1,h}\|_{L^2(\Omega)} = O(h^2),$$

  where h is the mesh size. The constants take into account the geometry of all triangles present in the mesh $\mathcal{T}_h$ discretizing the n-gon Ω.

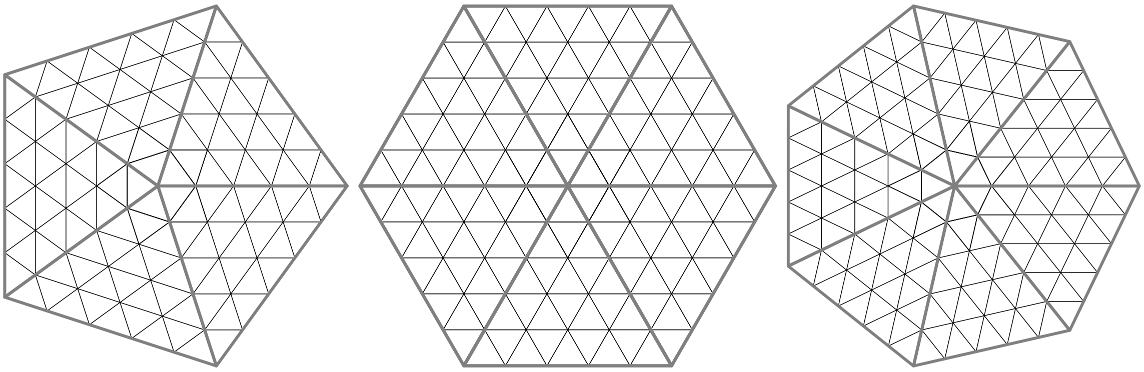

Figure 5.3: Examples of symmetric meshes for regular polygons used in the computations.

- The estimate for the approximation of $\mathbf{U}_i$, solution of (5.9) is more involved. The difficulties come from the lack of global $H^2(\mathbb{P}_n)$ regularity. We use again the $H^{2+s}(\mathbb{P}_n)$ regularity of the eigenfunction to conclude that the singular term in the right hand side of (5.9) belongs to $H^{-\frac{1}{2}-\gamma}(\mathbb{P}_n)$ for $\gamma \in (0,1/2)$. The main results allowing us to obtain a quantified estimate for $\mathbf{U}_i$ is [A7, Theorem 5.2] where we show that if U is a generic scalar component of $\mathbf{U}_i$ then
$$\|\nabla U - \nabla U_h\|_{L^2(\mathbb{P}_n)} = O(h^{0.5-\gamma}),$$
for every $\gamma \in (0,1/2)$ with explicit constants depending on γ. Moreover, the constants go to $+\infty$ as $\gamma \to 0$.
- A detailed analysis of the equation (5.9) is given in [A7, Section 5] and all required *a priori* estimates for the constants involved are given. In particular, we even suppose that the mesh of $\mathbb{P}_n$ is symmetric and is made of congruent triangles, as shown in Figure 5.3.
- The terms involving $\mathbf{U}_i$ in formulas given in Theorem 5.3.1 have a particular structure, involving the bilinear form $a(u,v) = \int_\Omega \nabla u \cdot \nabla v - \lambda_1(\Omega)uv$, also appearing in the variational formulation of the material derivatives (5.9). In [63, Section 5] it is shown that defining some auxiliary problems can double the convergence speed in the estimates for some particular quantities of interest. We perform the same analysis in [A7, Section 5.3] and we arrive at a quantified error terms for eigenvalues of $\mathbf{M}^\lambda$ which are enough to guarantee the positivity of the remaining $2n-4$ non-zero eigenvalues for $n \in \{5,6,7,8\}$.

The next result summarizes the results described above:

Theorem 5.3.2. *The terms $\alpha_k, \beta_k, \gamma_k$ in Theorem 5.3.1 admit an error estimate of order $O(h^{1-2\gamma})$ for every $\gamma \in (0,1/2)$ when the first eigenfunction u_1 and the function $\mathbf{U}_0 = (U_0^1, U_0^2)$ are approximated using $\mathbf{P_1}$ finite elements.*

Having explicit *a priori* error estimates, we are ready to perform the numerical computations. The software FreeFEM [66] is used in its parallel version. The simulations are run on the Cholesky cluster at the Institut Polytechnique de Paris on up to 400 cores. The computation process is described below:

- Given $n \geq 5$ we construct a symmetric mesh as shown in Figure 5.3 with mesh size h equal to the length of the equal sides in the small isosceles triangles composing it. The size h is chosen such that estimates in Theorem 5.3.2 are enough to guarantee positivity of the non-zero eigenvalues of $\mathbf{M}^\lambda$ defined in (5.12), following Theorem 5.3.1.
- Piecewise affine $\mathbf{P_1}$ elements are used to approximate λ_1, u_1 and solutions $\mathbf{U}_i, i = 0, ..., n-1$ of (5.9). The numerical quantities obtained are used to compute $\alpha_k, \beta_k, \gamma_k$ shown in Theorem 5.3.1 as well as the constants in estimates from Theorem 5.3.2.
- For each one of the $\alpha_k, \beta_k, \gamma_k$, the explicit error estimate gives intervals $I_{\alpha_k}, I_{\beta_k}, I_{\gamma_k}$ guaranteed to contained the exact result. These intervals are used in Intlab [109] to find intervals

	h	d.o.f.
Pentagon	10^{-4}	250 025 001
Hexagon	10^{-4}	300 030 001
Heptagon	10^{-4}	350 035 001
Octagon	10^{-4}	400 040 001

Table 5.1: Size of the computational problems for the finite element computations.

Pentagon			
Eig.	l.b.	u.b.	mult.
2.568803	2.359297	2.784816	2
8.015038	7.558395	8.460722	2
13.458443	13.012758	13.915086	2

Hexagon			
Eig.	l.b.	u.b.	mult.
1.323826	1.040291	1.629895	2
3.916803	3.112218	4.719205	2
12.990672	12.188270	13.795257	2
7.566593	6.326083	8.803012	1
11.540733	10.304314	12.781243	1

Heptagon			
Eig.	l.b.	u.b.	mult.
0.747352	0.446026	1.096876	2
2.056766	0.963449	3.148214	2
4.655979	3.078862	6.228621	2
12.292485	10.719843	13.869602	2
12.582047	11.490599	13.675364	2

Octagon			
Eig.	l.b.	u.b.	mult.
0.452095	0.182855	0.774247	2
1.171933	0.309482	2.034382	2
2.772135	1.273803	4.268064	2
12.049631	11.187182	12.912082	2
13.037208	11.541279	14.535540	2
3.999568	1.460555	6.536411	1
11.740713	9.203870	14.279726	1

Table 5.2: Numerical approximations of the $2n-4$ non-zero eigenvalues of the Hessian matrix for $n \in \{5,6,7,8\}$ together with intervals given by the error estimate in Theorem 5.3.2

containing the eigenvalues of $\mathbf{M}^\lambda$. If among these intervals we find $2n-4$ which do not contain 0, then we have found $2n-4$ strictly positive eigenvalues.

The strategy described above allows us to conclude that the regular n-gon is a local minimizer for $n \in \{5,6,7,8\}$. The bounds for the corresponding non-zero eigenvalues are shown in Table 5.2. The missing ingredient to have a complete proof is the control of errors made in the FEM computations: resolution of discrete linear systems and machine errors. Basic estimations based on estimates of the condition number of the rigidity and mass matrices for $\mathbf{P_1}$ finite elements (see [76] for example) show that errors related to the linear systems have the form $O(\varepsilon h^{-2})$, where ε is the given machine precision. Evaluating machine precision errors is more involved, as shown in [13], for example. Ideally the whole FEM computation should be made in Intlab, but for now this is costly in view of the need to validate large linear systems and large eigenvalue problems. In the perspective section we enumerate some ideas that might lead to a complete proof in this sense.

The sizes of the numerical computations associated to the FEM problems are enumerated in Table 5.1. The *a priori* estimates have the particularity that the precision of the computation can be evaluated before execution. Evaluating the optimal problem size which still allows us to conclude the local minimality leads to estimations shown in Table 5.3. In particular, any further improvements in the error estimates shown in Theorem 5.3.2 concerning the constants or the order of convergence would lead to a further decrease in size which could allow to perform the whole computation using interval arithmetics and complete the proof of the local minimality of the regular n-gon for problem (5.2).

	Mesh size	deg. freedom
Pentagon	9.8e-4	$\approx$ 2.6 million
Hexagon	4.2e-4	$\approx$ 17 million
Heptagon	1.9e-4	$\approx$ 97 million
Octagon	1.35e-4	$\approx$ 220 million

Table 5.3: Approximately optimal mesh sizes and number of degrees of freedom for which currently known *a priori* estimates allow to certify the local minimality.

5.4 Reducing the proof to a finite number of numerical simulations

For a given $n \geq 5$ suppose that the regular n-gon is a local minimizer for (5.2). Suppose also that, fixing two vertices, we have a quantified neighborhood $V_n \subset \mathbb{R}^{2n-4}$ for the remaining $n-2$ vertices where local minimality occurs, based on [A7, Section 3]. This could be achieved by either theoretical or numerical methods, like the ones shown in the previous section.

To achieve the objective stated in the introduction, namely to use numerical tools in order to complete the proof of the Polyà-Szegö conjecture, first we establish some theoretical results regarding geometric aspects of an optimal n-gon, denoted by Q_n in the following. Denote by $l_n^* = \lambda_1(Q_n)|Q_n|$, the minimal value for scale invariant objective functional $P \mapsto \lambda_1(P)|P|$ among n-gons. Recall that the existence of such an optimal n-gon is guaranteed by the results in [68, Chapter 3]. The main results are enumerated below:

- Fixing the volume of Q_n there exists an explicit upper bound for the diameter of the optimal n-gon. In the scale invariant setting this translates into a restriction regarding the possible *flatness* of the optimal n-gon. Fixing two vertices of the polygon, corresponding to the longest side, in the scale invariant setting leads to a lower bound on the area of the optimal n-gon. The result is described in detail in [A7, Theorem 7.1] and the proof uses techniques introduced in [38].
- A lower bound on the smallest edge length of Q_n, when the volume is fixed, is provided in [A7, Theorem 7.3]. This lower bound for the shortest side length also holds in the scale invariant setting, since we have a lower bound on the area.
- A quantitative stability result in [A7, Lemma 7.4] shows that for two polygons with the same area and an upper bound on the diameter, closedness of the vertices implies closedness of the first eigenvalues. Makai's inequality [94] gives a lower bound on the first eigenvalue in terms of the inradius ρ_P: $\lambda_1(P) \geq \frac{1}{4\rho_P^2}$. Using this inequality and the lower bound on the area we obtain an explicit lower bound for the inradius of an optimal n-gon Q_n. Among polygons with prescribed lower bound on the inradius we obtain an explicit result of the following form.

  If $P = [\mathbf{a}_0 ... \mathbf{a}_{n-1}], Q = [\mathbf{b}_0 ... \mathbf{b}_{n-1}]$ are two n-gons having areas in $[m, M]$, $0 < m < M$, with inradii verifying $\rho_P, \rho_Q \geq \rho_{\min} > 0$ such that $|\mathbf{a}_i \mathbf{b}_i| \leq \delta$ then

  $$|\lambda_1(P) - \lambda_1(Q)| \leq C_n \delta^{1/2},$$

  where the constant C_n depends only on n.

Based on these theoretical results we prove in [A7, Theorem 7.5] that the proof of the Polyà-Szegö conjecture can be achieved using a finite number of numerical computations. The argument presented is formal and uses a ball covering of a compact set of $\mathbb{R}^{2n-4}$ containing coordinates of admissible polygons verifying the geometric constraints described above. In the following, I present an alternative argument, also abstract, allowing to reach the same conclusions. More concrete variants that are more appropriate from a computational point of view are discussed in the Perspectives section.

Consider $n \geq 5$ and, up to a change of variables, fix two vertices $\mathbf{a}_0 = (0,0), \mathbf{a}_1 = (1,0)$. We work with the scale invariant functional $P \mapsto \lambda_1(P)|P|$, therefore without loss of generality we assume that $[\mathbf{a}_0\mathbf{a}_1]$ is the longest edge of the polygon $P = [\mathbf{a}_0 ... \mathbf{a}_{n-1}]$. The remaining $n-2$ vertices lie in a bounded region of the plane and their coordinates belong to a compact region $R_n \subset \mathbb{R}^{2n-4}$. Following the arguments described above, there exists an explicit constant K_n such that if the vertices of admissible n-gons P, Q are at distance at most equal to δ then

$$|\lambda_1(P)|P| - \lambda_1(Q)|Q|| \leq K_n \delta^{1/2}. \tag{5.14}$$

Choose an estimate ε_1 of the minimal value of $|P|\lambda_1(P)$ outside the local minimality neighborhood V_n described above. For example, start with $\varepsilon_1 = 1$ and perform the steps described below. Assuming that l_n^* is given by the regular n-gon, in the following l_n^* represents an approximation of $\lambda_1(\mathbb{P}_n)|\mathbb{P}_n|$.

- Suppose that outside the local minimality neighborhood V_n we have $\lambda_1(P)|P| \geq l_n^* + \varepsilon_1$.
- Consider a uniform grid of squares (S_n) **in the plane** having diagonals δ_0 , covering the region where vertices of polygons with vertices in $R_n \subset \mathbb{R}^{2n-4}$ belong. See Figure 5.4 for an illustration. It follows that the set R_n can be covered by products of the form $S_{i_2} \times ... \times S_{i_{n-1}}$. The length δ_0 is chosen such that:
  (a) δ_0 is smaller than half the size of the minimal edge of the optimal polygon, determined analytically previously. Therefore any admissible polygon P having coordinates in R_n will have vertices in different squares (S_n).
  (b) Using the constant K_n from (5.14) we have $K_n\delta_0^{1/2} < \varepsilon_1/4$. This implies that if an admissible polygon P with vertices $\mathbf{a}_j \in S_{i_j}$, $j = 2, ..., n-1$ verifies $\lambda_1(P)|P| \geq l_n^* + \varepsilon_1/4$ then no other polygon having vertices in the same squares is better than the regular n-gon.
- There is a finite number of cartesian products $S = S_{i_2} \times ... \times S_{i_{n-1}}$. Loop through all of them and perform the following:
  (a) Find an admissible polygon in the current region S. If no such polygon exists, there is nothing to be done.
  (b) If the current region is included in the local minimality neighborhood V_n, there is nothing to be done.
  (c) If an admissible polygon P exists, compute $\lambda_1(P)|P|$ using a certified finite element computation obtaining an interval with length smaller than $\varepsilon_1/4$. If this certified computation gives $\lambda_1(P)|P| \geq l_n^* + \varepsilon_1/2$ then no other polygon better than the regular n-gon exists in the current region.
  (d) If the previous inequality is not verified, divide ε_1 by two and repeat the above procedure.

Suppose the procedure described above fails for every choice of ε_1 of the form $1/2^m$, $m \geq 1$. Then a sequence of polygons converging to a counter example lying outside the local minimality neighborhood will be found, contradicting the conjecture. Assuming the conjecture is true, the strategy described above will finish after a finite number of numerical computations.

Alternative approach. Considering again a square grid, like in Figure 5.4, and $n-2$ small squares $S_{i_2}, ..., S_{i_{n-1}}$, consider polygons Q_1, Q_2 such that:

- $Q_1 = [\mathbf{a}_0\mathbf{a}_1\mathbf{b}_2 ... \mathbf{b}_{n-1}]$ with $\mathbf{b}_j \in S_{i_j}, 2 \leq j \leq n-1$ has minimal area. See Figure 5.5 (left).
- Q_2 is a maximal polygon with respect to inclusion, containing all polygons of the form $[\mathbf{a}_0\mathbf{a}_1\mathbf{b}_2 ... \mathbf{b}_{n-1}]$ with $\mathbf{b}_j \in S_{i_j}, 2 \leq j \leq n-1$. Note that Q_2 may have more than n sides. In view of the monotnicity of the eigenvalues with respect to inclusion, Q_2 is used to obtain a lower bound for eigenvalues of polygons $P = [\mathbf{a}_0\mathbf{a}_1\mathbf{a}_2 ... \mathbf{a}_{n-1}]$ with $\mathbf{a}_j \in S_{i_j}$. See Figure 5.5 (center).

Then $\lambda_1(Q_2)|Q_1|$ is a lower bound for $P \mapsto \lambda_1(P)|P|$ for P having vertices $\mathbf{a}_0, \mathbf{a}_1, \mathbf{a}_j \in S_{i_j}, 2 \leq j \leq n-1$. If this lower bound is higher than l_n^* then the region $S = S_{i_2} \times ... \times S_{i_{n-1}}$ does not contain a better competitor than the regular n-gon. If the inequality does not hold, divide each

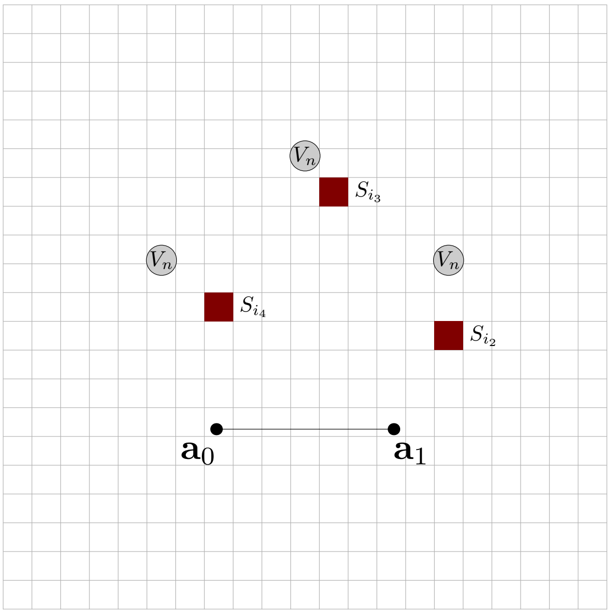

Figure 5.4: Graphical illustration of the computational strategy for $n = 5$: the fixed points $\mathbf{a}_0$, $\mathbf{a}_1$, the local minimality neighborhood V_n, the square grid and squares $S_{i_2}, S_{i_3}, S_{i_4}$ are represented.

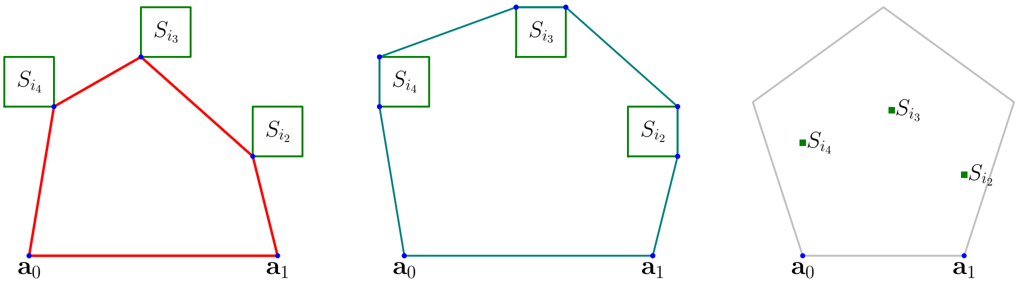

Figure 5.5: Examples of polygons giving lower bounds for the area (left) and the eigenvalue (center) for polygons with vertices $\mathbf{a}_0, \mathbf{a}_1, \mathbf{a}_j \in S_{i_j}, 2 \leq j \leq 4$. The picture on the right shows an example of three squares $S_{i_2}, S_{i_3}, S_{i_4}$ with sides 0.04 which do not contain any competitors better than the regular pentagon. The numerical validation of this fact used 262144 numerical computations.

square in smaller ones and repeat the procedure recursively.

It is not clear if this method is efficient in practice, since the squares need to be small for the inequality described above to hold. Nevertheless, in Figure 5.5 an example is shown for $n = 5$, where the validation of polygons having vertices in the squares $S_{i_j}, 2 \leq j \leq 4$ is performed. The numerical validation used 262144 numerical computations, showing that these regions do not contain a better polygon than the regular n-gon.

5.5 Perspectives

The results described in this chapter have various natural perspectives described below. The goal is to apply the strategy presented here to complete the proof of the optimality for the regular n-gon for at least one value of $n \geq 5$.

- The first objective is the completion of the proof for the local minimality of the regular n-gon. Ideally, a theoretical proof of the positivity for the eigenvalues described in Theorem 5.3.1 should be given. Alternatively, the estimates in Theorem 5.3.2 should be improved.

Initial results, investigating deeper regularity results in [64] concerning problems (5.9) show that even though the solutions $\mathbf{U}_i$ are not globally in $H^2(\mathbb{P}_n)$, they are, in fact piecewise H^2 for every triangle in the triangulation shown in Figure 5.1.

- After improving the convergence results in Theorem 5.3.2, the whole finite element computation should be performed in Intlab [109]. Studying the code used for validating matrix eigenvalue problems shows that natural improvements are readily available.
- The theoretical arguments in [A7, Section 3] should be revisited and all constants involved in the estimates should be evaluated. The argument using Stein extensions could be replaced with an argument using only the extension operator for the regular polygon.
- Qualitative properties of the minimal n-gons should be further investigated. In particular, the question of convexity is still open. The new results regarding the explicit second order derivatives could help deal with this aspect. Proving that the optimal n-gon is convex would drastically reduce the computational cost of the strategy described in Section 5.4.
- Numerical experiments show that using particular changes of basis, different from the one shown in Figure 5.2, the resulting Hessian matrix becomes almost diagonal. This suggests that more details regarding the structure of the second derivatives could be found. In particular, the second shape derivative (5.6) and the Hessian matrix found in Theorem 5.2.1 should be investigated in the context of the structure theorem described in [100].
- Practical aspects regarding the strategy described in Section 5.4 should be further addressed, evaluating more precisely the computational cost and the feasibility of the approach proposed.

Bibliography

[1] G. Alberti. Variational models for phase transitions, an approach via Γ-convergence. In *Calculus of variations and partial differential equations (Pisa, 1996)*, pages 95–114. Springer, Berlin, 2000.

[2] G. Allaire. *Conception optimale de structures*, volume 58 of *Mathématiques & Applications (Berlin) [Mathematics & Applications]*. Springer-Verlag, Berlin, 2007. With the collaboration of Marc Schoenauer (INRIA) in the writing of Chapter 8.

[3] G. Allaire, C. Dapogny, R. Estevez, A. Faure, and G. Michailidis. Structural optimization under overhang constraints imposed by additive manufacturing technologies. *J. Comput. Phys.*, 351:295–328, 2017.

[4] G. Allaire and L. Jakabčin. Taking into account thermal residual stresses in topology optimization of structures built by additive manufacturing. *Math. Models Methods Appl. Sci.*, 28(12):2313–2366, 2018.

[5] G. Allaire, F. Jouve, and G. Michailidis. Molding direction constraints in structural optimization via a level-set method. In *Variational analysis and aerospace engineering*, volume 116 of *Springer Optim. Appl.*, pages 1–39. Springer, Cham, 2016.

[6] G. Allaire, F. Jouve, and G. Michailidis. Thickness control in structural optimization via a level set method. *Struct. Multidiscip. Optim.*, 53(6):1349–1382, 2016.

[7] G. Allaire, F. Jouve, and A.-M. Toader. Structural optimization using sensitivity analysis and a level-set method. *J. Comput. Phys.*, 194(1):363–393, 2004.

[8] P. Antunes and P. Freitas. New bounds for the principal Dirichlet eigenvalue of planar regions. *Experiment. Math.*, 15(3):333–342, 2006.

[9] P. R. S. Antunes. Maximal and minimal norm of Laplacian eigenfunctions in a given subdomain. *Inverse Problems*, 32(11):115003, 18, 2016.

[10] P. R. S. Antunes and P. Freitas. Numerical optimization of low eigenvalues of the Dirichlet and Neumann Laplacians. *J. Optim. Theory Appl.*, 154(1):235–257, 2012.

[11] P. R. S. Antunes and P. Freitas. Optimisation of eigenvalues of the Dirichlet Laplacian with a surface area restriction. *Appl. Math. Optim.*, 73(2):313–328, 2016.

[12] P. R. S. Antunes and A. Henrot. On the range of the first two Dirichlet and Neumann eigenvalues of the Laplacian. *Proc. R. Soc. Lond. Ser. A Math. Phys. Eng. Sci.*, 467(2130):1577–1603, 2011.

[13] I. Babuška and G. Söderlind. On roundoff error growth in elliptic problems. *ACM Trans. Math. Software*, 44(3):Art. 33, 22, 2018.

[14] G. Barbatis, V. I. Burenkov, and P. D. Lamberti. Stability estimates for resolvents, eigenvalues, and eigenfunctions of elliptic operators on variable domains. In *Around the research of Vladimir Maz'ya. II*, volume 12 of *Int. Math. Ser. (N. Y.)*, pages 23–60. Springer, New York, 2010.

[15] A. H. Barnett and T. Betcke. Stability and convergence of the method of fundamental solutions for Helmholtz problems on analytic domains. *J. Comput. Phys.*, 227(14):7003–7026, 2008.

[16] S. Bartels and G. Wachsmuth. Numerical approximation of optimal convex shapes. *SIAM J. Sci. Comput.*, 42(2):A1226–A1244, 2020.

[17] T. Bayen. Analytical parameterization of rotors and proof of a Goldberg conjecture by optimal control theory. *SIAM J. Control Optim.*, 47(6):3007–3036, 2008.

[18] T. Bayen. *Etude de quelques problèmes de contrôle optimal issus des EDP et des EDO.* Habilitation à diriger des recherches, Université Montpellier II - Sciences et Techniques du Languedoc, Dec. 2013.

[19] T. Bayen and D. Henrion. Semidefinite programming for optimizing convex bodies under width constraints. *Optim. Methods Softw.*, 27(6):1073–1099, 2012.

[20] T. Bayen, T. Lachand-Robert, and E. Oudet. Analytic parametrization of three-dimensional bodies of constant width. *Arch. Ration. Mech. Anal.*, 186(2):225–249, 2007.

[21] M. P. Bendsøe and N. Kikuchi. Generating optimal topologies in structural design using a homogenization method. *Comput. Methods Appl. Mech. Engrg.*, 71(2):197–224, 1988.

[22] J. Berry, E. Bongiovanni, W. Boyer, B. Brown, P. Gallagher, D. Hu, A. Loving, Z. Martin, M. Miller, B. Perpetua, and S. Tammen. The convex body isoperimetric conjecture in the plane. *Rose-Hulman Undergraduate Mathematics Journal*, 18(2), 2017. `https://scholar.rose-hulman.edu/rhumj/vol18/iss2/2`.

[23] M. Bihr. *Optimisation Topologique du Couple Pièce/Support pour la Fabrication Additive sur Lit de Poudre.* Thesis, Institut Polytechnique de Paris, Dec. 2021. `https://tel.archives-ouvertes.fr/tel-03631143`.

[24] B. Bogosel. *Optimisation de formes et problèmes spectraux.* Thesis, Université Grenoble Alpes, Dec. 2015. `https://tel.archives-ouvertes.fr/tel-01502792`.

[25] V. Bonnaillie-Noël and B. Helffer. Numerical analysis of nodal sets for eigenvalues of Aharonov-Bohm Hamiltonians on the square with application to minimal partitions. *Exp. Math.*, 20(3):304–322, 2011.

[26] V. Bonnaillie-Noël and B. Helffer. On spectral minimal partitions: the disk revisited. *Ann. Univ. Buchar. Math. Ser.*, 4(LXII)(1):321–342, 2013.

[27] V. Bonnaillie-Noël and B. Helffer. Nodal and spectral minimal partitions—the state of the art in 2016. In *Shape optimization and spectral theory*, pages 353–397. De Gruyter Open, Warsaw, 2017.

[28] V. Bonnaillie-Noël, B. Helffer, and G. Vial. Numerical simulations for nodal domains and spectral minimal partitions. *ESAIM Control Optim. Calc. Var.*, 16(1):221–246, 2010.

[29] V. Bonnaillie-Noël, B. Helffer, and G. Vial. Numerical simulations for nodal domains and spectral minimal partitions. *ESAIM Control Optim. Calc. Var.*, 16(1):221–246, 2010.

[30] J. F. Bonnans and A. Shapiro. *Perturbation analysis of optimization problems.* Springer Series in Operations Research. Springer-Verlag, New York, 2000.

[31] K. J. Böröczky, E. Makai, Jr., M. Meyer, and S. Reisner. On the volume product of planar polar convex bodies—lower estimates with stability. *Studia Sci. Math. Hungar.*, 50(2):159–198, 2013.

[32] B. Bourdin, D. Bucur, and É. Oudet. Optimal partitions for eigenvalues. *SIAM J. Sci. Comput.*, 31(6):4100–4114, 2009/10.

[33] A. Braides. *Approximation of Free-Discontinuity Problems.* Springer, 1998.

[34] E. Bretin, R. Denis, J.-O. Lachaud, and E. Oudet. Phase-field modelling and computing for a large number of phases. *ESAIM Math. Model. Numer. Anal.*, 53(3):805–832, 2019.

[35] D. Bucur. Minimization of the k-th eigenvalue of the Dirichlet Laplacian. *Arch. Ration. Mech. Anal.*, 206(3):1073–1083, 2012.

[36] D. Bucur and G. Buttazzo. *Variational methods in shape optimization problems.* Progress in Nonlinear Differential Equations and their Applications, 65. Birkhäuser Boston, Inc., Boston, MA, 2005.

[37] D. Bucur, I. Fragalà, B. Velichkov, and G. Verzini. On the honeycomb conjecture for a class of minimal convex partitions. *Transactions of the American Mathematical Society*, 2017.

[38] D. Bucur and D. Mazzoleni. A surgery result for the spectrum of the Dirichlet Laplacian. *SIAM J. Math. Anal.*, 47(6):4451–4466, 2015.

[39] D. Bucur and B. Velichkov. Multiphase shape optimization problems. *SIAM J. Control Optim.*, 52(6):3556–3591, 2014.

[40] C. Bui, C. Dapogny, and P. Frey. An accurate anisotropic adaptation method for solving the level set advection equation. *Internat. J. Numer. Methods Fluids*, 70(7):899–922, 2012.

[41] G. Buttazzo. Gamma-convergence and its Applications to Some Problems in the Calculus of Variations. *School on Homogenization ICTP, Trieste, September 6-17*, 1993.

[42] L. A. Caffarelli and F.-H. Lin. Singularly perturbed elliptic systems and multi-valued harmonic functions with free boundaries. *J. Amer. Math. Soc.*, 21(3):847–862, 2008.

[43] L. A. Cafferelli and F. H. Lin. An optimal partition problem for eigenvalues. *J. Sci. Comput.*, 31(1-2):5–18, 2007.

[44] M. Conti, S. Terracini, and G. Verzini. An optimal partition problem related to nonlinear eigenvalues. *J. Funct. Anal.*, 198(1):160–196, 2003.

[45] S. J. Cox and E. Flikkema. The minimal perimeter for N confined deformable bubbles of equal area. *Electron. J. Combin.*, 17(1):Research Paper 45, 23, 2010.

[46] O. Cybulski, V. Babin, and R. Hoł yst. Minimization of the Renyi entropy production in the space-partitioning process. *Phys. Rev. E (3)*, 71(4):046130, 10, 2005.

[47] O. Cybulski and R. Hołyst. Tiling a plane in a dynamical process and its applications to arrays of quantum dots, drums, and heat transfer. *Phys. Rev. Lett.*, 95:088304, Aug 2005.

[48] C. Dapogny, C. Dobrzynski, and P. Frey. Three-dimensional adaptive domain remeshing, implicit domain meshing, and applications to free and moving boundary problems. *J. Comput. Phys.*, 262:358–378, 2014.

[49] C. Dapogny, A. Faure, G. Michailidis, G. Allaire, A. Couvelas, and R. Estevez. Geometric constraints for shape and topology optimization in architectural design. *Comput. Mech.*, 59(6):933–965, 2017.

[50] C. Dapogny and P. Frey. Computation of the signed distance function to a discrete contour on adapted triangulation. *Calcolo*, 49(3):193–219, 2012.

[51] G. De Philippis and B. Velichkov. Existence and regularity of minimizers for some spectral functionals with perimeter constraint. *Appl. Math. Optim.*, 69(2):199–231, 2014.

[52] M. C. Delfour and J.-P. Zolésio. *Shapes and geometries*, volume 22 of *Advances in Design and Control.* Society for Industrial and Applied Mathematics (SIAM), Philadelphia, PA, second edition, 2011. Metrics, analysis, differential calculus, and optimization.

[53] J. Desai, G. Allaire, and F. Jouve. Topology optimization of structures undergoing brittle fracture. *J. Comput. Phys.*, 458:Paper No. 111048, 35, 2022.

[54] S. Dominguez, N. Nigam, and B. Shahriari. A combined finite element and Bayesian optimization framework for shape optimization in spectral geometry. *Comput. Math. Appl.*, 74(11):2874–2896, 2017.

[55] L. Esposito, V. Ferone, B. Kawohl, C. Nitsch, and C. Trombetti. The longest shortest fence and sharp Poincaré-Sobolev inequalities. *Arch. Ration. Mech. Anal.*, 206(3):821–851, 2012.

[56] E. Feleqi. Estimates for the deviation of solutions and eigenfunctions of second-order elliptic Dirichlet boundary value problems under domain perturbation. *J. Differential Equations*, 260(4):3448–3476, 2016.

[57] F. Feppon, G. Allaire, and C. Dapogny. A variational formulation for computing shape derivatives of geometric constraints along rays. *ESAIM Math. Model. Numer. Anal.*, 54(1):181–228, 2020.

[58] F. Feppon, G. Allaire, C. Dapogny, and P. Jolivet. Topology optimization of thermal fluid-structure systems using body-fitted meshes and parallel computing. *J. Comput. Phys.*, 417:109574, 30, 2020.

[59] A. V. Fiacco. *Introduction to sensitivity and stability analysis in nonlinear programming*, volume 165 of *Mathematics in Science and Engineering.* Academic Press, Inc., Orlando, FL, 1983.

[60] F. Fodor. The densest packing of 19 congruent circles in a circle. *Geom. Dedicata*, 74(2):139–145, 1999.

[61] I. Fragalà and B. Velichkov. Serrin-type theorems for triangles. *Proc. Amer. Math. Soc.*, 147(4):1615–1626, 2019.

[62] G. D. M. G. Buttazzo. An existence result for a class of shape optimization problems. *Arch. Rational Mech. Anal.*, 122:183–195, 1993.

[63] T. Grätsch and K.-J. Bathe. A posteriori error estimation techniques in practical finite element analysis. *Comput. & Structures*, 83(4-5):235–265, 2005.

[64] P. Grisvard. *Elliptic problems in nonsmooth domains*, volume 24 of *Monographs and Studies in Mathematics.* Pitman (Advanced Publishing Program), Boston, MA, 1985.

[65] T. C. Hales. The honeycomb conjecture. *Discrete & Computational Geometry*, 25(1):1–22, 2001.

[66] F. Hecht. New development in FreeFem++. *J. Numer. Math.*, 20(3-4):251–265, 2012.

[67] B. Helffer, T. Hoffmann-Ostenhof, and S. Terracini. Nodal domains and spectral minimal partitions. *Ann. Inst. H. Poincaré Anal. Non Linéaire*, 26(1):101–138, 2009.

[68] A. Henrot. *Extremum problems for eigenvalues of elliptic operators.* Frontiers in Mathematics. Birkhäuser Verlag, Basel, 2006.

[69] A. Henrot, editor. *Shape optimization and spectral theory.* De Gruyter Open, Warsaw, 2017.

[70] A. Henrot and E. Oudet. Minimizing the second eigenvalue of the Laplace operator with Dirichlet boundary conditions. *Arch. Ration. Mech. Anal.*, 169(1):73–87, 2003.

[71] A. Henrot and M. Pierre. *Shape variation and optimization*, volume 28 of *EMS Tracts in Mathematics*. European Mathematical Society (EMS), Zürich, 2018. A geometrical analysis, English version of the French publication [MR2512810] with additions and updates.

[72] R. A. Horn and C. R. Johnson. *Matrix analysis*. Cambridge University Press, Cambridge, second edition, 2013.

[73] H. Iriyeh and M. Shibata. Symmetric Mahler's conjecture for the volume product in the 3-dimensional case. *Duke Math. J.*, 169(6):1077–1134, 2020.

[74] I. M. Jaglom and V. G. Boltjanskiĭ. *Convex figures*. Translated by Paul J. Kelly and Lewis F. Walton. Holt, Rinehart and Winston, New York, 1960.

[75] S. G. Johnson. The nlopt nonlinear-optimization package. `http://github.com/stevengj/nlopt`.

[76] L. Kamenski, W. Huang, and H. Xu. Conditioning of finite element equations with arbitrary anisotropic meshes. *Math. Comp.*, 83(289):2187–2211, 2014.

[77] T. Kato. *Perturbation theory for linear operators*. Springer-Verlag, Berlin-New York, second edition, 1976. Grundlehren der Mathematischen Wissenschaften, Band 132.

[78] B. Kawohl and T. Lachand-Robert. Characterization of Cheeger sets for convex subsets of the plane. *Pacific J. Math.*, 225(1):103–118, 2006.

[79] B. Kawohl and C. Weber. Meissner's mysterious bodies. *Math. Intelligencer*, 33(3):94–101, 2011.

[80] B. Kloeckner. Dans quelle forme la plus petite paroi enfermant un volume donné est-elle la plus grande ? - Images des mathématiques : `http://images.math.cnrs.fr/Dans-quelle-forme-la-plus-petite-paroi-enfermant-un-volume-donne-est-elle-la.html`, 12 2019.

[81] A. Koldobsky, C. Saroglou, and A. Zvavitch. Estimating volume and surface area of a convex body via its projections or sections. *Studia Math.*, 244(3):245–264, 2019.

[82] S. Kravitz. Packing Cylinders into Cylindrical Containers. *Math. Mag.*, 40(2):65–71, 1967.

[83] T. Lachand-Robert and E. Oudet. Minimizing within convex bodies using a convex hull method. *SIAM J. Optim.*, 16(2):368–379, 2005.

[84] T. Lachand-Robert and É. Oudet. Bodies of constant width in arbitrary dimension. *Math. Nachr.*, 280(7):740–750, 2007.

[85] J. Lamboley and A. Novruzi. Polygons as optimal shapes with convexity constraint. *SIAM J. Control Optim.*, 48(5):3003–3025, 2009/10.

[86] J. Lamboley, A. Novruzi, and M. Pierre. Regularity and singularities of optimal convex shapes in the plane. *Arch. Ration. Mech. Anal.*, 205(1):311–343, 2012.

[87] J. Lamboley, A. Novruzi, and M. Pierre. Polygons as maximizers of dirichlet energy or first eigenvalue of dirichlet-laplacian among convex planar domains, 2021.

[88] A. Laurain. Distributed and boundary expressions of first and second order shape derivatives in nonsmooth domains. *J. Math. Pures Appl. (9)*, 134:328–368, 2020.

[89] A. Laurain and K. Sturm. Distributed shape derivative *via* averaged adjoint method and applications. *ESAIM Math. Model. Numer. Anal.*, 50(4):1241–1267, 2016.

[90] X. Liu and S. Oishi. Verified eigenvalue evaluation for the Laplacian over polygonal domains of arbitrary shape. *SIAM J. Numer. Anal.*, 51(3):1634–1654, 2013.

[91] X. Liu and S. Oishi. Verified eigenvalue evaluation for the Laplacian over polygonal domains of arbitrary shape. *SIAM J. Numer. Anal.*, 51(3):1634–1654, 2013.

[92] S. Luckhaus and L. Modica. The Gibbs-Thompson relation within the gradient theory of phase transitions. *Arch. Rational Mech. Anal.*, 107(1):71–83, 1989.

[93] F. Maggi. *Sets of finite perimeter and geometric variational problems*, volume 135 of *Cambridge Studies in Advanced Mathematics*. Cambridge University Press, Cambridge, 2012. An introduction to geometric measure theory.

[94] E. Makai. A lower estimation of the principal frequencies of simply connected membranes. *Acta Math. Acad. Sci. Hungar.*, 16:319–323, 1965.

[95] E. Meissner. Über die anwendung von fourier-reihen auf einige aufgaben der geometrie und kinematik. *Vierteljahrschrift der Naturforschenden Gesellschaft*, 54:309–329, 1909.

[96] Q. Mérigot and E. Oudet. Handling convexity-like constraints in variational problems. *SIAM J. Numer. Anal.*, 52(5):2466–2487, 2014.

[97] L. Modica and S. Mortola. Un esempio di γ^--convergenza. *Boll. Un. Mat. Ital. B (5)*, 14(1):285–299, 1977.

[98] F. Morgan. Soap bubbles in $\mathbf{R}^2$ and in surfaces. *Pacific J. Math.*, 165(2):347–361, 1994.

[99] F. Morgan. Convex body isoperimetric conjecture. `https://sites.williams.edu/Morgan/2010/07/03/convex-body-isoperimetric-conjecture/`, 2010.

[100] A. Novruzi and M. Pierre. Structure of shape derivatives. *J. Evol. Equ.*, 2(3):365–382, 2002.

[101] S. Osher and J. A. Sethian. Fronts propagating with curvature-dependent speed: algorithms based on Hamilton-Jacobi formulations. *J. Comput. Phys.*, 79(1):12–49, 1988.

[102] É. Oudet. Numerical minimization of eigenmodes of a membrane with respect to the domain. *ESAIM Control Optim. Calc. Var.*, 10(3):315–330 (electronic), 2004.

[103] É. Oudet. Approximation of partitions of least perimeter by Γ-convergence: around Kelvin's conjecture. *Exp. Math.*, 20(3):260–270, 2011.

[104] E. Oudet. Shape optimization under width constraint. *Discrete Comput. Geom.*, 49(2):411–428, 2013.

[105] M. M. H. Pang. Approximation of ground state eigenvalues and eigenfunctions of Dirichlet Laplacians. *Bull. London Math. Soc.*, 29(6):720–730, 1997.

[106] G. Pólya and G. Szegö. *Isoperimetric Inequalities in Mathematical Physics*. Annals of Mathematics Studies, no. 27. Princeton University Press, Princeton, N. J., 1951.

[107] P. Ramachandran and G. Varoquaux. Mayavi: 3d visualization of scientific data. *Computing in Science Engineering*, 13(2):40–51, 2011.

[108] M. Ritoré and E. Vernadakis. Isoperimetric inequalities in Euclidean convex bodies. *Trans. Amer. Math. Soc.*, 367(7):4983–5014, 2015.

[109] S. M. Rump. Verification methods: rigorous results using floating-point arithmetic. *Acta Numer.*, 19:287–449, 2010.

[110] G. Savaré and G. Schimperna. Domain perturbations and estimates for the solutions of second order elliptic equations. *J. Math. Pures Appl. (9)*, 81(11):1071–1112, 2002.

[111] R. I. Saye and J. A. Sethian. The Voronoi implicit interface method for computing multiphase physics. *Proc. Natl. Acad. Sci. USA*, 108(49):19498–19503, 2011.

[112] R. Schneider. *Convex bodies: the Brunn-Minkowski theory*, volume 151 of *Encyclopedia of Mathematics and its Applications*. Cambridge University Press, Cambridge, expanded edition, 2014.

[113] J. A. Sethian. *Level set methods and fast marching methods*, volume 3 of *Cambridge Monographs on Applied and Computational Mathematics*. Cambridge University Press, Cambridge, second edition, 1999. Evolving interfaces in computational geometry, fluid mechanics, computer vision, and materials science.

[114] L. Stewart. Matlab lbfgs wrapper. `http://www.cs.toronto.edu/~liam/software.shtml`.

[115] G. J. Tee. Eigenvectors of block circulant and alternating circulant matrices. *New Zealand J. Math.*, 36:195–211, 2007.

[116] A. Wächter and L. T. Biegler. On the implementation of an interior-point filter line-search algorithm for large-scale nonlinear programming. *Math. Program.*, 106(1, Ser. A):25–57, 2006.

[117] B.-H. Wang and Y.-K. Wang. A note on the convex body isoperimetric conjecture in the plane, 2021.

[118] M. Y. Wang, X. Wang, and D. Guo. A level set method for structural topology optimization. *Comput. Methods Appl. Mech. Engrg.*, 192(1-2):227–246, 2003.

[119] Y. Wang, J. Gao, and Z. Kang. Level set-based topology optimization with overhang constraint: towards support-free additive manufacturing. *Comput. Methods Appl. Mech. Engrg.*, 339:591–614, 2018.

[120] D. Weaire and R. Phelan. A counter-example to Kelvin's conjecture on minimal surfaces. *Forma*, 11(3):209–213, 1996. Reprint of Philos. Mag. Lett. 69 (1994), no. 2, 107–110.

[121] W. Wichiramala. Efficient cut for a subset of prescribed area. *Thai J. Math.*, 5(3, Special issue):95–100, 2007.

[122] Y. Zhang, G. Guillemot, M. Bernacki, and M. Bellet. Macroscopic thermal finite element modeling of additive metal manufacturing by selective laser melting process. *Comput. Methods Appl. Mech. Engrg.*, 331:514–535, 2018.

Institut Polytechnique de Paris
91120 Palaiseau, France